
Robust Laser-Based Optical Measurement in Industrial Harsh Environments.

by

Marcos Alonso Nieto

Advisors

Manuel M Graña Romay

7th July 2022

Acknowledgements

I would like to thank my esteemed supervisor Prof. Manuel Graña for the opportunity to undertake my studies at the Department of Computer Science and Artificial Intelligence, for his invaluable supervision, support and tutelage during the course of my PhD degree. My gratitude extends to Prof. Alberto Izaguirre for his invaluable advice, continuous support, and patience during my PhD study. Their immense knowledge and plentiful experience have encouraged me in all the time of my academic research. I would also like to thank Dr. Imanol Andonegui and Dr. Daniel Maestro-Watson for their technical support on my study, their treasured support was really influential in shaping my experiment methods and critiquing my results, and for a cherished time spent together in the lab.

I would especially like to thank Dr. Elena Silvestre and Dr. Lander Galdos for their contributions to data collection and for being there to support me and help me with all the industrial validation experiments. Further, I would like to thank Dr. Jairo R. Sánchez and Dr. Hugo Álvarez for their support, constructive thoughts and ideas during my research. Their assistance and commitment during the testing and assessment phases in industrial environments has been of tremendous help. I am also indebted to all of the Robotics and Automation Group members at Faculty of Engineering of Mondragon University, for providing me with all the necessary facilities for the research, for their continuous encouragement, and for sharing their expertise during this time.

Finally, I would like to express my gratitude to my family, thank you all for supporting me. A especial thank to my beloved wife, I can't thank you enough for encouraging me throughout this experience. Without your tremendous understanding and encouragement it would have been impossible for me to complete my research. Thank you for "being there" when I needed you.

Declaration

Hereby I declare that except where specific reference is made to the work of others, this document is my original authorial work, which I have worked out on my own. The contents of this dissertation are original and have not been submitted in whole or in part for consideration for any other degree or qualification in this, or any other University. All sources, references, and literature used or excerpted during the elaboration of this work are properly cited and listed in complete reference to the due source.

Marcos Alonso Nieto
7th July 2022

Abstract

In the metal parts manufacturing industry, maximising the throughput, manufacturing on time and on budget, and ensuring zero-defect products are among the most significant aspects of the production chain. The purpose of Quality Control is to prevent defects, i.e, ensure that the parts are made to comply with design specifications and will function properly as part of larger assemblies, such as a car transmission, engine, car body, just to cite some. Quality Control also contributes to product safety and prevents reliability issues, which can often increase costs, lead to product recalls, or trigger issues that endanger final consumers.

This thesis reports on the design and experimental assessment of reliable dimensional control using laser based optical devices. Modeling and calibration of such systems, as well as the filtering of the delivered data, has been one of the primary motivations. In particular, modern AI-based algorithms such as Deep Learning and Machine Learning have made these processes faster and easier. Two scenarios were chosen to validate experimentally this work. The former consists of an in-line inspection where complex warm forged revolution parts for automotive propulsion systems are measured. The latter computes the flatness and the surface quality of metal sheets produced by a cut to length production line, where the entire process of unwinding, fattening, cutting and stacking metal sheets takes place.

Keywords:

Optical Laser Sensor, Calibration, 3D Reconstruction, Depth Data Denoising, Convolutional Neural Networks, Deep Learning, In-line Dimensional Inspection, Warm Forming, Roll Levelling, Flatness Inspection.

Contents

Contents	vii
List of Figures	ix
List of Tables	xi
1 Introduction	1
2 Foundation and Context	3
2.1 Camera Model	3
2.1.1 Intrinsic Parameters	4
2.1.2 Extrinsic Parameters	5
2.1.3 Projective Transformation	5
2.2 Laser triangulation	6
2.2.1 Basic Principle	6
2.2.2 Sensor Calibration	8
2.2.3 Scheimpflug Condition	10
2.3 3D Surface Data Denoising	11
2.3.1 Piecewise Cubic Hermite Interpolation Denoising Filter	12
2.3.2 Deep Learning Approaches	12
3 Hypotheses and Objectives	19
3.1 Hypotheses	19
3.2 Objectives	20
3.3 Brief description of the publications and contributions	20
3.3.1 Article 1: A Multi Camera and Multi Laser Calibration Method for 3D Reconstruction of Revolution Parts.	21
3.3.2 Article 2: Optical Dual Laser Based Sensor Denoising for Online Metal Sheet Flatness Measurement Using Hermite Interpolation.	21
3.3.3 Article 3: Depth Data Denoising in Optical Laser Based Sensors for Metal Sheet Flatness Measurement: A Deep Learning Approach.	21
4 Results	23
4.1 Multi camera and multi laser sensing setup and calibration method for 3D reconstruction of forged revolution parts	23
4.1.1 Scheimpflug Distortion	24
4.1.2 Calibration Repeatability and Accuracy	25
4.1.3 Real Case	26

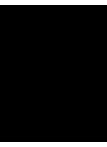
4.2	Optical Laser based Sensor and Algorithms for Real Time Surface Reconstruction and Flatness Measurement in Metal Sheet Industries	26
4.2.1	Dual Laser Line Sensor and Hermite Interpolations Results	27
4.2.2	Single Laser Line Sensor and Deep Learning Approach Results	28
5	Conclusions and Future Work	33
5.1	Conclusions	33
5.2	Contributions to knowledge	35
5.3	Future Work	36
	Bibliography	39
6	Appendix	47
6.1	Publication 1: A Multi Camera and Multi Laser Calibration Method for 3D Reconstruction of Revolution Parts	49
6.2	Publication 2: Optical Dual Laser Based Sensor Denoising for Online Metal Sheet Flatness Measurement Using Hermite Interpolation	71
6.3	Publication 3: Depth Data Denoising in Optical Laser Based Sensors for Metal Sheet Flatness Measurement: A Deep Learning Approach	93

List of Figures

2.1	Schematic diagram of image sensor's imaging model	4
2.2	General configuration of a laser triangulation system.	7
2.3	Schematic of an imaging system with the Scheimpflug principle in a 2D view.	10
2.4	Neuron model in Artificial Neural Network.	13
2.5	Multi-layer ANN architecture.	14
2.6	Schematic of an autoencoder model architecture.	15
2.7	Schematic of an autoencoder model architecture.	16
2.8	Schematic of the U-Net model architecture.	16
4.1	The proposed and deployed optical system for 3D Reconstruction of Warm-Die Forged Revolution Parts	24
4.2	Calibration pattern and Measured planes and Cylinders during the repeatability tests	24
4.3	(a) Sensor raw data for a S235JR steel coil with observed high frequency transient noisy waves and background noise. (b) Denoised sensor data using the proposed Hermite interpolation filtering method.	28
4.4	(a) Sensor raw data for a S500MC high yield steel coil with with observed periodic transient impulses and background noise. (b) Denoising results of the sensor raw data using the proposed Hermite interpolation filtering method.	29
4.5	An instance of a longitudinal section of the surface reconstruction, the blue line represents the raw 1D data, the red line shows the Hermite interpolation result, the yellow line shows Symlet results, and finally the green line depicts the CBRDNet denoised result. The inset provides a better detail of the results achieved by both Hermite and CBRDNet in the highlighted area.	31

List of Tables

4.1	Mean and standard deviation error (in mm) of some primitives (cylinders and planes) of the calibration pattern respect to nominal values using different calibrations.	25
4.2	Comparative results of our approach with other conventional denoising approaches. MAE = mean absolute error; MaxAE = maximum absolute error; STD = standard deviation of the absolute error; RMSE = root mean squared error.	28
4.3	Comparative results of our approach with traditional 1D denoising approaches. MAE = mean absolute error; MaxAE = maximum absolute error; STD = standard deviation of the absolute error; RMSE = root mean squared error. Best results presented in bold font.	30
4.4	Comparative results of our approach with traditional 2D denoising approaches. MAE = mean absolute error; MaxAE = maximum absolute error; STD = standard deviation of the absolute error; RMSE = root mean squared error. Best results presented in bold font.	30
4.5	Comparative results of our approach with traditional 2D denoising approaches. MAE = mean absolute error; MaxAE = maximum absolute error; STD = standard deviation of the absolute error; RMSE = root mean squared error. Best results presented in bold font.	31



Introduction

Quality control can be traced back to medieval Europe, when craftsmen formed guilds in the late 13th century. They were in charge of establishing stringent criteria for quality of products and services. Inspection committees enforced the standards by affixing a distinctive mark or symbol to faultless items. Initially, this identifier was used to track the source of defective products. However, the symbol evolved to indicate the craftsman's high quality across time. Customers throughout medieval Europe relied on inspection seals and master craftsmen markings as guarantee of quality.

Until the Industrial Revolution in the early nineteenth century, this method to manufacturing quality was prevalent. The emphasis on product inspection, began in the mid-1750s in Great Britain and during the Industrial Revolution in the early 1800s. Quality procedures emerged throughout the 1800s as a result of changes in manufacturing techniques. The skill of the labourers, complemented by audits and inspections, ensured quality in the production system. Defective products were either reworked or discarded. Late in the nineteenth century, the main goal was to boost productivity without having a large number of qualified workers. This increased focus on mass production had a detrimental impact on quality. To address this deterioration, managers organised quality inspection departments to avoid faulty items from reaching customers.

The introduction of "processes" in quality practices began around the turn of the twentieth century. A "process" is defined as the set of actions that beginning with an input, adds value to it, and ends with an output. In the mid-1920s, manufacturers began to focus on process control, making quality crucial not just for the completed product but also for the processes that produced it. Quality control departments realised that all industrial processes produce data, and this data could be analysed statistically to determine if a process is stable and under control, or whether it was altered by specific factors that must be addressed. As a result, quality was assessed using statistical sample techniques, and the production processes were monitored using quality control charts, setting the groundwork for modern-day quality control [1, 2, 3].

In today's intelligent manufacturing era, new technologies have completely overthrown conventional manufacturing processes. With the arrival of Industry 4.0, a significant part of industrial processes are now carried out by smart machines, production systems are

interconnected, and so all manufacturing operations, including quality control. This fact implies that every single process has to be designed as intelligent as possible in order to operate with minimum human interaction. Therefore, intelligent technologies and digitisation approaches have resulted in significant improvements in quality control.

Machine vision and artificial intelligence, for instance, are widely used for quality control in a wide range of applications [4, 5, 6, 7, 8]. It is well known that automated machine vision systems are able to analyse geometrical and aesthetic aspects to assess product quality. These systems minimise human intervention, which leads to subjectivity and fatigue resulting from performing repetitive tasks that may result in human errors, ensure a higher grade of accuracy, repeatability, optimise operational efficiency, and reduce quality control downtime increasing enterprise profits. However, in some scenarios such as industrial harsh environments, there exists undesirable conditions (high temperatures, dust, mechanical vibrations, high-speed manufacturing lines, etc.) making image-base quality control challenging.

In this thesis, we deal with two particular scenarios of mass production. The former, is a high-speed forging press producing warm metal parts (600-800 °C) for the automotive industry, that must be inline inspected with respect to several dimensional parameters and the absence of surface defects have to be verified. The latter, is about a Cut To Length Line (CTL) for the uncoiling, levelling, measuring, cross-cutting to length and stacking work of metal sheets. Both are examples where quality control processes strive against the aforesaid demanded conditions.

Imaging-based sensing tries to overcome the aforementioned challenges. Among the existing technologies, laser-based optical sensors are one of the most commonly used for dimensional measuring. They offer a useful balance between resolution and precision, can be used in high-speed applications, and they are robust and reliable under varying conditions. These sensors are based in the laser triangulation principle, i.e., they use a laser light source and a camera to obtain 3-dimensional measurements. The laser beam and the camera are both focused at the inspection object, thus, depth variations are measured using trigonometry, given a known angular distance between the laser plane and the camera sensor plane. These sensors, combined with machine vision algorithms [9, 10, 11, 12, 13], have received considerable attention. Recently, advances in this field have benefit from improvements in artificial intelligence. Particularly, Convolutional Neural Networks (CNNs) have been widely used for image processing, pattern recognition, and classification, achieving outstanding results [14, 15, 16, 17]. Nevertheless, innovative technologies and improvements in laser-based sensors for quality control processes in harsh industrial environments are required.

Therefore, this thesis tackles the challenge of optical laser-based sensors in quality control processes and intends to enhance this field, managing complex and mass production aspects, in particular in industrial harsh scenarios. This works reports on the design and experimental assessment of reliable dimensional quality control methods, the devising of laser-based optical sensors for industrial harsh environments, and the modelling, calibration and filtering of data provided by such devices.

Foundation and Context

This chapter explains the theoretical concepts, which have been the guiding light throughout the work of this thesis. Therefore, the following subsections are concerned with the most commonly used camera calibration model, namely the pin-hole camera, laser triangulation principle and the Scheimplug condition, and finally we close by presenting some data filtering techniques used in this thesis.

2.1 Camera Model

In this section, we will go through the geometry and image acquisition of a single camera. More precisely, we begin with a description of the projective transformation. Next, the so-called pin-hole camera model is introduced. Finally, we address the computation of the extrinsic and intrinsic parameters, and also the most common type of camera lens distortions coefficients, i.e., radial and tangential.

Any image acquisition system, whether human or computer-based, performs a transformation of real 3D space into 2D space. Identifying the parameters of this transformation is essential to characterise the system. The most basic design of real camera consists of a pin-hole and an imaging sensor (image plane). This camera, also named "camera obscura" or pin-hole camera, was first used by the arabic scientist Alhazen around 1000 AD as a roughly approximation to the human eye [18]. Light rays enter a pin-hole camera through a narrow aperture and generate an image on the camera sensor also known as the image plane. The image is generated upside down, much the same as the human eye. The image plane in the pin-hole model used for calculations is rotated 180 degrees around the vertical axis and the optical axis, leaving the image plane in front of the pin-hole aperture and with an image perceived the same manner as the original. Because this configuration is physically impossible, it is referred to as the virtual image plane. However, this formulation in the pin-hole camera model simplifies the concept of projection calculations.

This results to the pin-hole camera model's basic formulation, as seen in Equation 2.2, where x and y are the image coordinates on the image plane, X , Y and Z are the world coordinates of the observed object, and f is the focal length which corresponds to image plane distance. A mathematical model of the simple pin-hole camera is illustrated

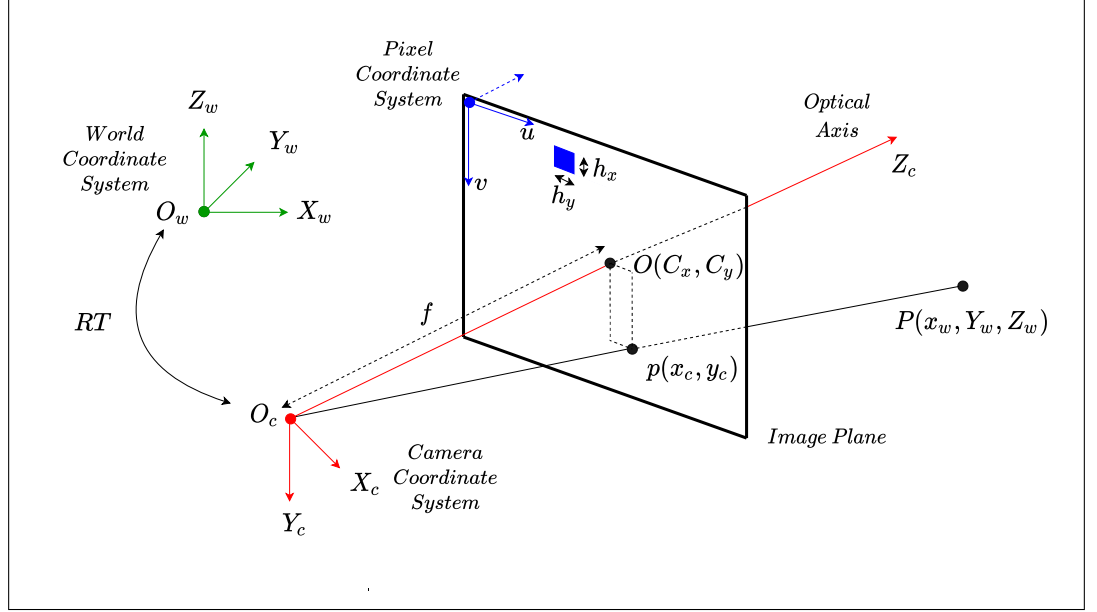


Figure 2.1: Schematic diagram of image sensor's imaging model

in Figure. 2.1. Two coordinate systems are of special relevance for understanding how points in the real world are mathematically related to points on the image plane. First, the world coordinate system, here with a subscript W . Second, the camera coordinate system here with a subscript C . These two coordinate systems are related by a translation and a 3D orthonormal rotation, represented by T and R . Point O_c , also called principal point or a focal point, where the axes X_c , Y_c and Z_c define the camera coordinate system. The point O_c projected on the image plane in the direction of Z_c determines the principal point coordinates $O = (C_x, C_y)$ in pixels.

Coordinates of the points P and p in camera coordinate systems are as follows:

$$P_c = [X_c, Y_c, Z_c]^T \quad p_c = [x_c, y_c, f]^T \quad (2.1)$$

Because of the optical axis being perpendicular to the image plane, and by similarity of triangles, we obtain the formulation of the pin-hole camera model as follows:

$$x_c = f \frac{X_c}{Z_c}, \quad y_c = f \frac{Y_c}{Z_c}, \quad (2.2)$$

2.1.1 Intrinsic Parameters

The intrinsic parameters of a camera can be summarised as the parameters of the projective transformation, i.e, the focal length f , the mapping relation between camera and image coordinate systems, and the geometric distortions.

The mapping relation between image and camera coordinate systems, i.e, between u, v and x_c, y_c is described by:

$$u = \frac{x_c}{h_x} + C_x, \quad v = \frac{y_c}{h_y} + C_y \quad (2.3)$$

where x_c and y_c are related to the camera coordinate system, and u, v to the system of the local image plane in pixels. Pixels dimensions, h_x and h_y , are usually expressed in μm in both sensor plane directions.

The geometric distortions produced by the optical elements of the camera are due to the non-linearity nature of these elements. In most practical scenarios, we can characterise these distortions as radial and tangential distortions, the magnitude of which increases as points move away from the image centre. These distortions can be modelled by a nonlinear correction adding a polynomial model firstly introduced by by Brown [19, 20], based on earlier work by Conrady [21]. The undistorted point is computed by:

$$\begin{pmatrix} x_u \\ y_u \end{pmatrix} = \begin{pmatrix} x_d (1 + K_1 r^2 + K_2 r^4 + \dots) + P_1 (r^2 + 2x_d^2) + 2P_2 x_d y_d (1 + P_3 r^2 + \dots) \\ y_d (1 + K_1 r^2 + K_2 r^4 + \dots) + 2P_1 x_d y_d + P_2 (r^2 + 2y_d^2)(1 + P_3 r^2 + \dots) \end{pmatrix}, \quad (2.4)$$

where x_d and y_d are the distorted coordinates of the projected point in the camera, x_u and y_u are the undistorted coordinates as projected by an ideal pin-hole camera, K_n is the n^{th} radial distortion coefficients, P_n is the n^{th} tangential distortion coefficients, being $r = \sqrt{x_d^2 + y_d^2}$. These parameters model the non-linear influence on the optical system.

2.1.2 Extrinsic Parameters

The extrinsic parameters are all the geometric parameters required to transform a point from the camera coordinate system to the world coordinate system and backwards. As a result, the extrinsic parameters of a camera are easily introduced as an orthonormal 3D rotation matrix \mathbf{R} and a translation matrix \mathbf{T} between \mathbf{O}_c and \mathbf{O}_w coordinate systems

For a given point \mathbf{P} , its coordinates in the camera and world coordinate systems are related by the following equation:

$$\mathbf{P}_c = \mathbf{R}\mathbf{P}_w + \mathbf{T}, \quad (2.5)$$

where \mathbf{P}_c stands for a point \mathbf{P}_c in the camera coordinate system, \mathbf{P}_w is its the same point expressed in world coordinate system. These matrices can be expanded as follows:

$$\mathbf{R} = \begin{bmatrix} r_{11} & r_{12} & r_{13} \\ r_{21} & r_{22} & r_{23} \\ r_{31} & r_{32} & r_{33} \end{bmatrix}, \quad \mathbf{T} = \mathbf{O}_w - \mathbf{O}_c = [t_x \quad t_y \quad t_z]^T \quad (2.6)$$

2.1.3 Projective Transformation

By substituting Equations 2.5 and 2.3 into 2.2, and not taking into account the distortions 2.4, we get the linear equation corresponding to the pin-hole camera model.

$$\tilde{\mathbf{m}} = \mathbf{H}\tilde{\mathbf{P}}_w, \quad (2.7)$$

where $\tilde{\mathbf{m}}$ are the homogeneous coordinates of the projected imaged point expressed in pixels. $\tilde{\mathbf{P}}_w$ are the homogeneous coordinates of the point \mathbf{P} in world coordinate system.

Finally, \mathbf{H} is the pin-hole camera transformation, also called projection matrix which can be expressed as the product of the following two matrices:

$$\mathbf{H} = \mathbf{K} [\mathbf{R}|\mathbf{T}] \quad (2.8)$$

Matrices \mathbf{R} and \mathbf{T} are given in Equation 2.6. \mathbf{K} defines the intrinsic parameters, and corresponds to Equations 2.2 and 2.3 expressed in homogeneous transformations form. Thus, Equation 2.7 above can be written as follows:

$$\tilde{\mathbf{m}} = s \begin{bmatrix} u \\ v \\ 1 \end{bmatrix} = \begin{bmatrix} \frac{f}{h_x} & 0 & C_x \\ 0 & \frac{f}{h_y} & C_y \\ 0 & 0 & 1 \end{bmatrix} \begin{bmatrix} r_{11} & r_{12} & r_{13} & t_x \\ r_{11} & r_{12} & r_{13} & t_y \\ r_{11} & r_{12} & r_{13} & t_z \end{bmatrix} \begin{bmatrix} X \\ Y \\ Z \\ 1 \end{bmatrix} \quad (2.9)$$

where s is a nonzero scalar implying that matrix \mathbf{H} is defined only up to a known scale parameter.

2.2 Laser triangulation

In this section, we address some fundamental aspects of the sheet-of-light triangulation principle, optical design considerations, the use of peak image intensity detector techniques, and the calibration of the camera and laser line sensor.

2.2.1 Basic Principle

The sheet-of-light technique is based on the principle of triangulation [22], performing a three-dimensional reconstruction of the surface of an opaque and diffuse reflecting solid by using area scan cameras and laser light projectors. Although sheet-of-light techniques are the most commonly used for surface reconstruction, other laser projected patterns like multiple laser stripes, patterns like circles [23, 24, 25], concentric multiple circles, and grids may be used.

In a typical laser triangulation sensor, the camera and the laser line projector must be mounted so that their main axes form an angle for triangulation. The value of this triangulation angle is typically between 30° and 60° . The projected light line defines a plane in 3D space. This plane intersects the surface of the solid under measurement, creating a profile of the surface that is visible to the camera. By moving the solid surface in front of the laser line projector, it is possible to record the whole surface of the solid. In order to increase the measurement range, a Scheimpflug configuration is used, where the detector plane has a tilted angle with respect to the imaging plane[26].

The measurement principle of the sheet-of-light technique is illustrated for a single laser line triangulation setup in Figure 2.2, where $\mathbf{P}_w = [X_w, Y_w, Z_w]^T$ is a point in the world coordinate system and $\mathbf{P}'_w = [x_w, y_w, z_w]^T$ is its projection in the image plane expressed in the world coordinate system. Equations 2.10 and 2.11 show how the 3D point \mathbf{P}_w can be computed knowing its projection on the camera image plane. Equation 2.10 corresponds to the projected line of the observation of point \mathbf{P}_w by the camera, and Equation 2.11

corresponds to the laser plane. Their intersection provides the desired world coordinates \mathbf{P}_w .

$$\mathbf{P}_w = \lambda \mathbf{v} + \mathbf{P}_{0w} \quad (2.10)$$

$$\mathbf{n}^T (\mathbf{P}_w - \mathbf{P}'_{0w}) = [a \ b \ c] \begin{bmatrix} P_x \\ P_y \\ P_z \end{bmatrix} + d = 0 \quad (2.11)$$

where \mathbf{P}_{0w} is the camera optical centre in world coordinate system, \mathbf{v} is the unitary vector between \mathbf{P}'_w and \mathbf{P}_{0w} , $\mathbf{n} = [a, b, c]^T$ is the plane's definition vector, and \mathbf{P}'_{0w} is any point lying on the laser plane [27].

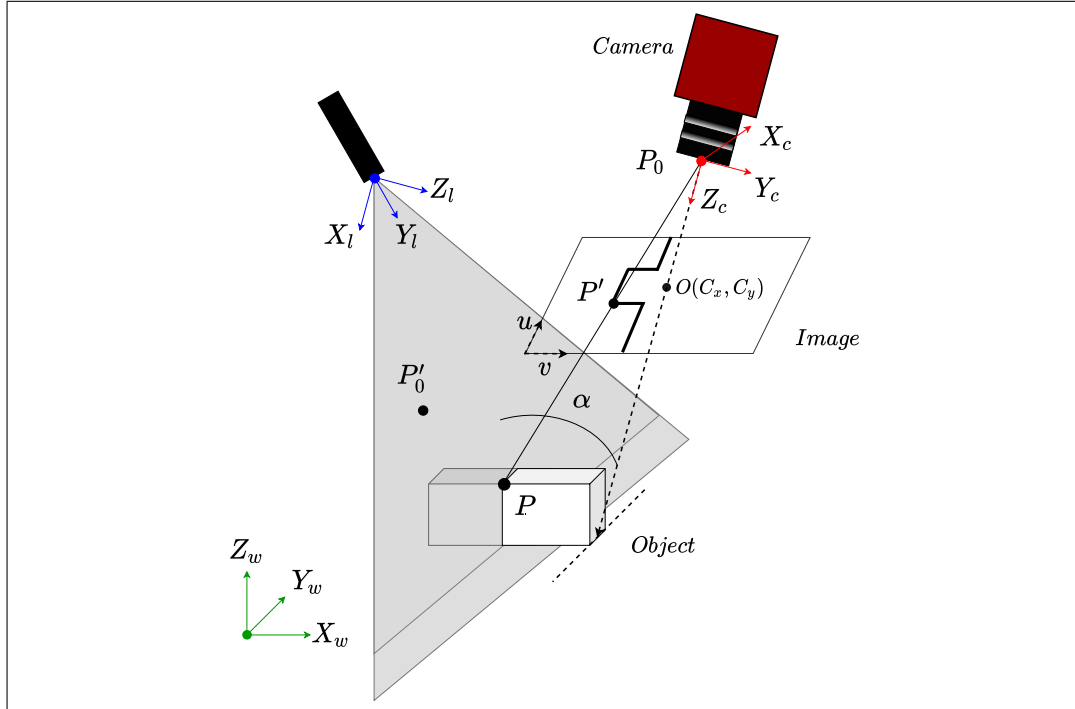


Figure 2.2: General configuration of a laser triangulation system.

The accuracy of a 3D reconstruction using laser linear illumination is significantly determined by the accuracy of the line identification in the image. Since the pattern of image intensity in the normal direction to the line has a Gaussian profile. Finding the centre of the line in the image corresponds to detecting the point of maximum intensity in the normal direction, also known as the laser peak, which can be detected by different algorithms using the intensity distribution along a column of the sensor image, e.g., finding the position of maximum intensity, finding thresholding points, or finding the centre of gravity with subpixel accuracy [28, 29, 30]. Among the different algorithms, Savitzky–Golay [31, 32] finite impulse response (FIR) differential filter is one of the most applied to the image intensity profile of the laser line for computing the zero-crossings with sub-pixel accuracy [33, 34, 35].

2.2.2 Sensor Calibration

The purpose of sensor calibration is to identify the camera intrinsic parameters and the mapping between the laser plane and the camera. Since the sensor consists of a laser projector and a camera, camera modelling and calibration become an integral part of the sensor calibration procedure. The conventional approach consists of using first a standard camera calibration technique [36, 37] to estimate the camera parameters, then the laser plane parameters are estimated by capturing the correspondences of 3D known points and applying the least squares method [38, 39, 40]. The calibration methods are dependent on the form of calibration target, the method for extracting control points for camera calibration and laser plane calibration, and the calibration algorithms used. For instance, the 2D plane with controlled movement [41], and the 3D target with the invariance of the cross ratio [42, 43] could be used. An alternative sensor calibration approach consists of finding the mapping function between the image plane and laser plane, treating the sensor as a black box carrying out a plane mapping function. This approach requires the estimation of at least eight parameters [44] by the plane constraint methods [45] or a least squares polynomial fitting method [46].

2.2.2.1 Calibration Method

In the pinhole camera model, from equation 2.7 and 2.8, the mapping between a 3D point in the world coordinate frame to the image coordinate frame is:

$$\tilde{\mathbf{m}} = \mathbf{K} [\mathbf{R}|\mathbf{T}] \tilde{\mathbf{P}}_{\mathbf{w}} . \quad (2.12)$$

This equation can be rewritten as it follows:

$$s \begin{bmatrix} u \\ v \\ 1 \end{bmatrix} = \mathbf{K} \begin{bmatrix} \mathbf{R}_1, \mathbf{R}_2, \mathbf{R}_3, \mathbf{T} \end{bmatrix} \begin{bmatrix} X_w \\ Y_w \\ Z_w \\ 1 \end{bmatrix} , \quad (2.13)$$

where \mathbf{R}_1 , \mathbf{R}_2 , and \mathbf{R}_3 are the columns of rotation matrix \mathbf{R} . Assuming that all the calibration points are placed on a plane with $Y_w = 0$ then,

$$s \begin{bmatrix} u \\ v \\ 1 \end{bmatrix} = \mathbf{K} \begin{bmatrix} \mathbf{R}_1, \mathbf{R}_3, \mathbf{T} \end{bmatrix} \begin{bmatrix} X_w \\ Z_w \\ 1 \end{bmatrix} . \quad (2.14)$$

Defining $\mathbf{H}_1 = \mathbf{K} \begin{bmatrix} \mathbf{R}_1, \mathbf{R}_3, \mathbf{T} \end{bmatrix}$, $\tilde{\mathbf{m}} = \begin{bmatrix} u, v, 1 \end{bmatrix}^T$, and $\tilde{\mathbf{P}}_1 = \begin{bmatrix} X_w, Z_w, 1 \end{bmatrix}^T$; we obtain the following expression for the mapping between the 2D image points and the 3D calibration planar points:

$$\tilde{\mathbf{m}} = \mathbf{H}_1 \tilde{\mathbf{P}}_1 \quad (2.15)$$

Given a set of calibration points and their corresponding image coordinates, the transformation matrix \mathbf{H}_1 , also known as **Homography** between the laser and image planes, can be estimated by solving the previous linear equation. Let us assume that the laser plane

XZ is our reference coordinate system. Let $\mathbf{P}_{li} = [X_{li}, Z_{li}]$ be a point in the laser plane and $\mathbf{P}_{ci} = [X_{ci}, Y_{ci}]$ the corresponding image plane point. The mapping between these two planes is given by:

$$s \begin{bmatrix} X_{ci} \\ Y_{ci} \\ 1 \end{bmatrix} = \begin{bmatrix} h_{11} & h_{12} & h_{13} \\ h_{21} & h_{22} & h_{23} \\ h_{31} & h_{32} & h_{33} \end{bmatrix} \begin{bmatrix} X_w \\ Z_w \\ 1 \end{bmatrix} \quad (2.16)$$

Carrying out the correction of the lens radial distortion, the mapping from the image plane to the laser plane becomes a linear function. The mapping transformation \mathbf{H}_1 can be estimated by minimal linear least squares:

$$\begin{aligned} sX_{ci} &= h_{l11}X_{li} + h_{l12}Z_{li} + h_{l13} \\ sY_{ci} &= h_{l21}X_{li} + h_{l22}Z_{li} + h_{l23} \\ s &= h_{l31}X_{li} + h_{l32}Z_{li} + h_{l33} \end{aligned} \quad (2.17)$$

For a set of corresponding points $\{\mathbf{P}_{li} = [X_{li}, Z_{li}]\}_i$ and $\{\mathbf{P}_{ci} = [X_{ci}, Y_{ci}]\}_i$, rearranging Equation 2.17, we get a linear system $\mathbf{A} \cdot \mathbf{H}_1 = \mathbf{0}$, where \mathbf{A} and \mathbf{H}_1 are given by Equation 2.18 and 2.19. The solution to this system is the least eigenvector of $\mathbf{A}^T \mathbf{A}$ or the eigenvector corresponding to the smallest singular value of the Singular Value Decomposition (SVD) of \mathbf{A} [47].

$$\mathbf{A} = \begin{bmatrix} -X_{li} & -Z_{li} & -1 & 0 & 0 & 0 & X_{ci}X_{li} & X_{ci}Z_{li} & X_{ci} \\ 0 & 0 & 0 & -X_{li} & -Z_{li} & -1 & Y_{ci}X_{li} & Y_{ci}Z_{li} & Y_{ci} \\ \vdots & \vdots & \vdots & \vdots & \vdots & \vdots & \vdots & \vdots & \vdots \\ -X_{ln} & -Z_{ln} & -1 & 0 & 0 & 0 & X_{cn}X_{ln} & X_{cn}Z_{ln} & X_{cn} \\ 0 & 0 & 0 & -X_{ln} & -Z_{ln} & -1 & Y_{ci}X_{li} & Y_{ci}Z_{li} & Y_{ci} \end{bmatrix}_{2n \times 9} \quad (2.18)$$

$$\mathbf{H}_1 = \begin{bmatrix} h_{l11} \\ h_{l12} \\ \vdots \\ h_{l32} \\ h_{l33} \end{bmatrix}_{1 \times 2n} \quad (2.19)$$

In most cases, for the identification of \mathbf{H}_1 parameters, planar patterns with easily identifiable imaged points are used [48, 49]. In some cases planar targets are not a feasible solution (for example, in an arrangement where the planar pattern cannot be seen by all cameras simultaneously), so a 3D calibration target is used instead. These 3D calibration objects are specific to each application and can be of different shapes and sizes, such as a stepped [50] or creased [51] gauge, a 3D cube with a white mark in the middle [50], a 3D sphere [52], or a 3D cone [53], among others.

2.2.3 Scheimpflug Condition

It is widely known that by tilting the lens with regard to the image plane, an arbitrary plane in the world coordinate system space can be imaged sharply in the sensor plane [54]. This technique is typically attributed to Theodor Scheimpflug, who submitted a series of patents during 1902 and 1904 [55, 56, 57, 58]. The principle, however, was originally established by Jules Carpentier [59].

The Scheimpflug condition enables us to handle the focusing challenges that arise in systems such as stereo vision setups, where the camera image planes must be tilted, fringe projection systems, and sheet-of-light devices such as the one depicted in Figure 2.2. In the latter devices, the Scheimpflug condition has to be necessarily fulfilled to obtain a sharp image of the laser line over the whole measurement range.

Lens's plane, image plane, and the plane of focus of a camera are generally parallel. As a result, if a planar object is parallel to the image plane, this will coincide with the plane of focus and the entire object will be focused. However, if the object plane is not parallel to the image plane, this will be in focus only across a line intersecting the plane of focus. However, when a lens is tilted, an oblique tangent extends from the image plane and another extends from the lens plane intersecting at a line through which the plane of focus also passes, as shown in Figure [2.3].

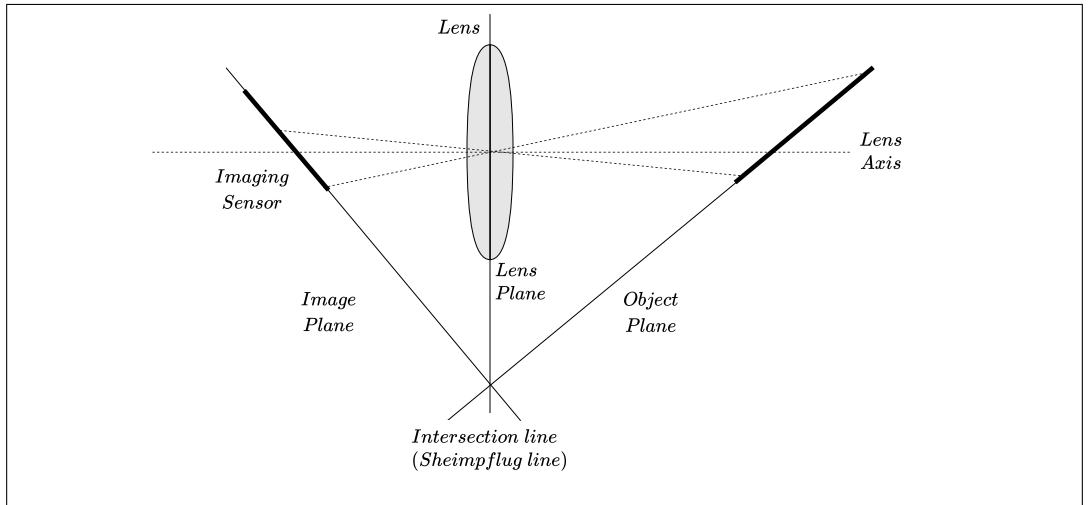


Figure 2.3: Schematic of an imaging system with the Scheimpflug principle in a 2D view.

Scheimpflug principle states that the object plane, the lens's plane, and the image plane must all meet in a single line [59]. This intersection line is also called the Scheimpflug line [60, 61]. With minor changes, this principle could be applied to both thin and thick prisms models.

The rotation that maps the ideal untilted image plane to the tilted one can be expressed as successive rotations around X_c and Y_c axes as follows [62]:

$$\mathbf{R}_S = \begin{bmatrix} \cos\beta & 0 & \sin\beta \\ 0 & 1 & 0 \\ -\sin\beta & 0 & \cos\beta \end{bmatrix} \begin{bmatrix} 1 & 0 & 0 \\ 0 & \cos\alpha & -\sin\alpha \\ 0 & \sin\alpha & \cos\alpha \end{bmatrix}. \quad (2.20)$$

Thus, the pixel coordinates in the tilted image $\mathbf{p}_t = (u_t, v_t)$ are computed using Equation 2.8 from $\mathbf{P} = (X, Y, Z)$ in the world coordinate system. Assuming the pin-hole model, disregarding the distortions, and taking into account the tilt effect of the Scheimpflug condition, the projection \mathbf{p}_t can be modeled as:

$$s \begin{bmatrix} u_t \\ v_t \\ 1 \end{bmatrix} = \mathbf{K} \cdot \mathbf{\Lambda} \cdot \mathbf{R}_S^T \cdot [\mathbf{R} | \mathbf{T}] \begin{bmatrix} X \\ Y \\ Z \\ 1 \end{bmatrix}, \quad (2.21)$$

where $\mathbf{\Lambda}$ is the so-called Scheimpflug array:

$$\mathbf{\Lambda} = \begin{bmatrix} \cos\alpha \cdot \cos\beta & 0 & \sin\beta \\ 0 & \cos\alpha \cdot \cos\beta & -\cos\alpha \cdot \sin\beta \\ 0 & 0 & 1 \end{bmatrix} \quad (2.22)$$

In cases where the tilted angle is small (Scheimpflug angles smaller than 6 degrees) the tangential distortion parameters compensate the Scheimpflug angle effects [63]. Thus, a pin-hole standard calibration with radial and tangential parameters can be used in order to calculate the Scheimpflug distortion map. However, many lenses with large focal lengths present almost no image distortion. In such cases, a direct laser-camera homography estimation without the calculation of the Scheimpflug parameters can be used [64].

2.3 3D Surface Data Denoising

Geometric measurement based on 3D surface reconstruction via optical sensors is a key feature for various disciplines such as computer-aided design, manufacturing, and industrial metrology for monitoring quality in production processes, just to cite some [65, 66, 67, 68, 69]. In particular, industrial metrology systems are capable of analysing the surface, shape and dimensions of workpieces during the production process, during the final inspection or in the measuring room. In order to acquire a 3D model, techniques such as laser scanning and structured light approaches, have been predominantly used, providing high accuracy even though they require specialised and expensive equipment.

However, these optical sensors are particularly prone to different noise sources that can significantly alter data. Some common sources include vibrations caused by mechanical processes, transporting systems, varying light conditions, optic defects, atmospheric turbulence, among others [70, 71, 72]. Formulating some of these noises is particularly challenging and, in consequence, removing their influence is not an easy task. Thus, high-quality optical measurement systems strongly depend on the quality of data denoising methods applied in order to extract the most accurate surface information.

In digital data processing, there are numerous noise reduction algorithms [73]. Therefore, when selecting a noise reduction algorithm, several factors must be taken into account. Some of these considerations are, a) the available computational power and cycle-time, b) whether losing some real data is acceptable when enables the system to remove additional noise, c) TUNING, and d) the noise characteristics and the amount of data detail that should be preserved.

The following subsections will present different data denoising techniques for optical 3D laser based sensors that have been used in this thesis.

2.3.1 Piecewise Cubic Hermite Interpolation Denoising Filter

The approximation of surface profiles by splines allows the detection of surface defects as regions of the surface that show a high distance relative to the approximating spline functions [74]. Specifically, the transform based on Hermite splines has a very convenient property, namely that the coefficients of a function corrupted with Gaussian noise follow a Gaussian distribution [75]. This property allows us to efficiently denoise the surface profile by simple thresholding of the coefficients. A cubic Hermite interpolator is a third order parametric polynomial curve specified in Hermite form, that is, by its values and first derivatives at the end points of the corresponding domain interval 2.23 that can operate efficiently in the form of filter implementation.

$$\begin{aligned}
Z(t) &= \mathbf{T} \cdot \mathbf{M}_H \cdot \mathbf{G}_H, \quad \text{being} \quad \mathbf{T} = [t^3 \quad t^2 \quad t \quad 1] \\
\mathbf{M}_H &= \begin{bmatrix} 2 & 1 & -2 & 1 \\ -3 & -2 & 3 & -1 \\ 0 & 1 & 0 & 0 \\ 1 & 0 & 0 & 0 \end{bmatrix} \\
\mathbf{G}_H &= [\rho(0) \quad \rho'(0) \quad \rho(1) \quad \rho'(1)]^T
\end{aligned} \tag{2.23}$$

where $t \in [0, 1]$, \mathbf{T} is a row vector containing the coefficients of the third order polynomial function, \mathbf{M}_H is the square matrix form composed of the four Hermite basis functions, and \mathbf{G}_H is the column vector form composed of the interval endpoints values and their derivatives, where $\rho(0)$ and $\rho(1)$ are the values at the boundaries of each interpolated curve, which may correspond to a surface laser profile, and $\rho'(0)$ and $\rho'(1)$ are their corresponding first derivatives with respect to t . A series of curve sampling intervals $\{\rho_k, \rho'_k\}_{k=1}^n$ can be interpolated by imposing boundary conditions such that the derivatives are continuous at the endpoints of neighboring intervals. These boundary conditions yield an interpolated curve consisting on cubic Hermite splines that is globally continuous and differentiable in $(t(1), t(k))$, i.e., it belongs to C^0 and C^1 [76].

However, in order to use the piece-wise cubic Hermite interpolation method, several considerations must be taken into account. On the one hand, the surface profile recovered from the sensor must have a signal-to-noise ratio (SNR) high enough to allow data interpolation. On the other hand, according to the Nyquist–Shannon sampling theorem [77], the gradient data sampling frequency must be at least twice that of the highest frequency of the original signal.

2.3.2 Deep Learning Approaches

Artificial neural networks (ANNs) are computational networks inspired by the human brain. ANN models, in particular, replicate the neuronal activity of the brain and central nervous system. The first doors to the development of neural networks were open in the late 1940s [78, 79]. Since then, these network structures have been evolved and have been

able to solve complex real-world problems in a variety of scientific fields, ranging from pharmaceutical research to finance.

ANNs are composed of artificial neurons (also known as perceptrons) that are interconnected with each other. These artificial neurons are typically structured in layers, and multiple layers piled together are called a multi-layer neural network. In an ANN, a neuron may be linked to all or a set of neurons in the following layer, with these links mimicking brain synaptic interconnections. Weighted signals arriving a neuron replicate the electrical activation of a neuron and, as a matter of fact, data transfer within the artificial brain. Each neuron in the ANN has weighted inputs, transfer function, and one output. An artificial neuron model is shown in Figure 2.4. The input data to a neuron, i_n is multiplied by a connection weight, $w_{n,m}$, which imitates the reinforcement of neurological brain pathways. Learning is reproduced in ANNs through the adaptation of these synaptic weighted connections.

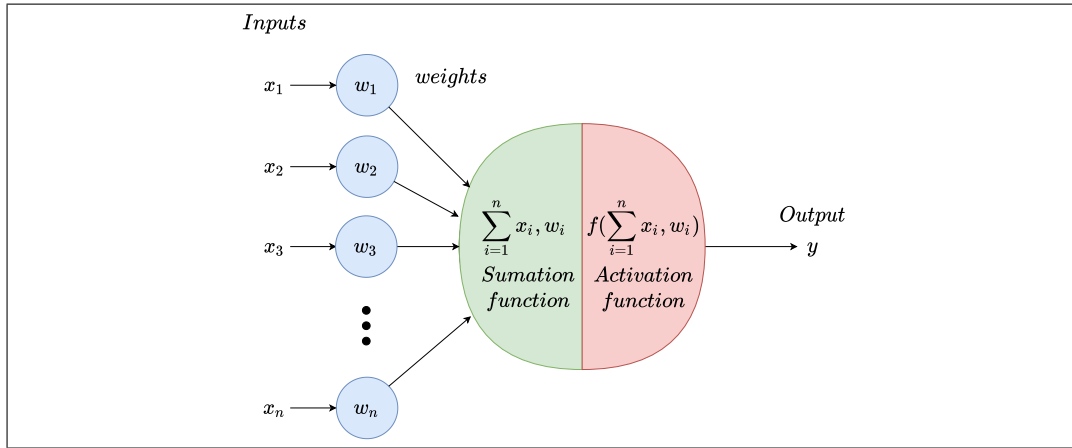


Figure 2.4: Neuron model in Artificial Neural Network.

The aforementioned neuron interconnections arrangement and geometry are very essential in ANNs. These arrangements always include two layers that are shared by all network architectures: the Input layer and the Output layer, the input layer feeds the input signal into the network, while the output layer produces the network's output. In multi-layer architectures, one or more additional layers known as Hidden layers are implemented. These layers, in which neurons are not kept in either the input or output layers, are hidden from the processes that interact with the network and behave as a black box to them. The system's computational and processing capacity can be increased by adding additional hidden layers, but the system's training phenomena become more complex at the same time. Thus, the problem to be solved and the available data plays a significant role in the ANN structure design. An example of a multi-layer ANN architecture with a single hidden layer is depicted in Figure 2.5.

2.3.2.1 Convolutional Neural Network (CNN)

Convolutional neural networks (CNN) are a specific form of ANN in which convolutional layers are used in the architecture design. A convolution layer is a fundamental component of the CNN architecture. It performs feature extraction, which typically consists of a combination of linear and nonlinear operations, i.e., convolution operation and activation

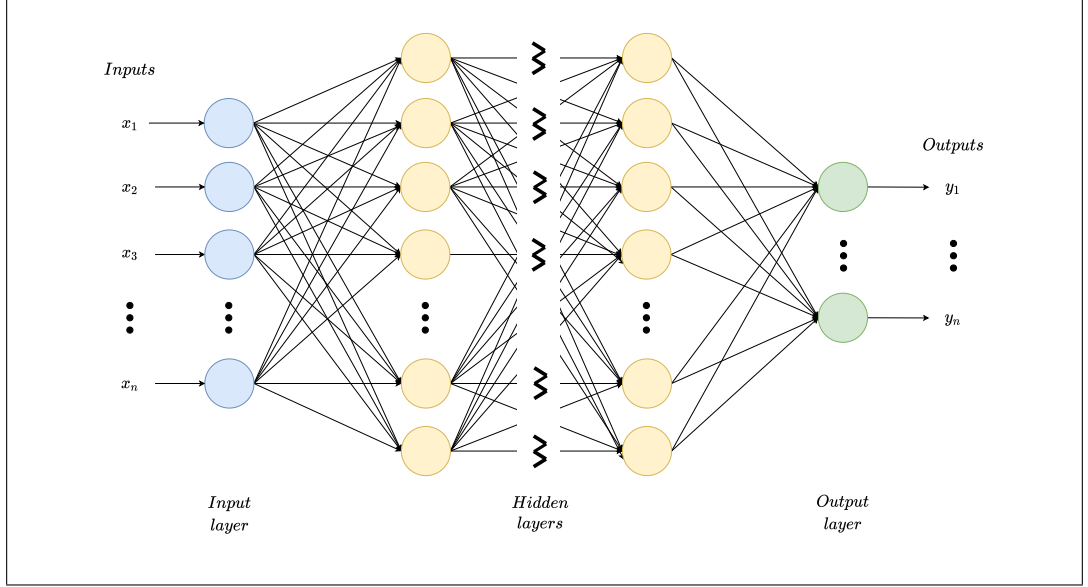


Figure 2.5: Multi-layer ANN architecture.

function. CNNs are designed and constructed to learn feature spatial hierarchies automatically and adaptively using multiple elements such as pooling layers, convolution layers, and fully connected layers. Thus, due to its hierarchical feature extraction ability CNNs have grown in popularity in a wide range of computer vision applications, being one of the most popular deep learning architecture.

CNNs were first used in LeNet [80] and demonstrated excellent performance in handwritten digit recognition and were ultimately used in image processing applications in the following years. A decade after the publication of LeNet, Krizhevsky et al. [81] proposed a novel CNN that can obtain a nearly 10% lower error rate in the ImageNet [82] benchmark in comparison to state-of-the-art methods of that time. Since then, CNNs became a boon in almost all image processing applications.

2.3.2.2 Autoencoder

An autoencoder is an unsupervised neural network architecture that is trained to reproduce the input as its output. It has a typical structure as a pair of funnels attached by the short end. The first funnel compresses the input data into a lower-dimension encoding, while the second funnel decompresses the encoding trying to recover the original input data. The encoder seeks to obtain a robust latent representation of the original data, which is often used for other purposes, such as features for another classification module. Figure 2.6 shows the autoencoder model architecture where $\tilde{\mathbf{x}}$ is one data sample of the dataset, \mathbf{x} is the output reconstructed version of $\tilde{\mathbf{x}}$, z is the latent space, f_θ is the encoding function parameterised by θ , and $g_{\theta'}$ the decoding function parameterised by θ' . The parameters θ and θ' are learned together to output a reconstructed data sample as similar as possible to the original input, i.e., $\tilde{\mathbf{x}} \approx f_\theta(g_{\theta'}(\mathbf{x}))$, or in other words, to learn an identity function. Various metrics can be used to quantify the difference between the reconstruction error. For image samples, generally, the MSE loss function is used.

Autoencoders have been a popular field of study in neural networks in recent decades.

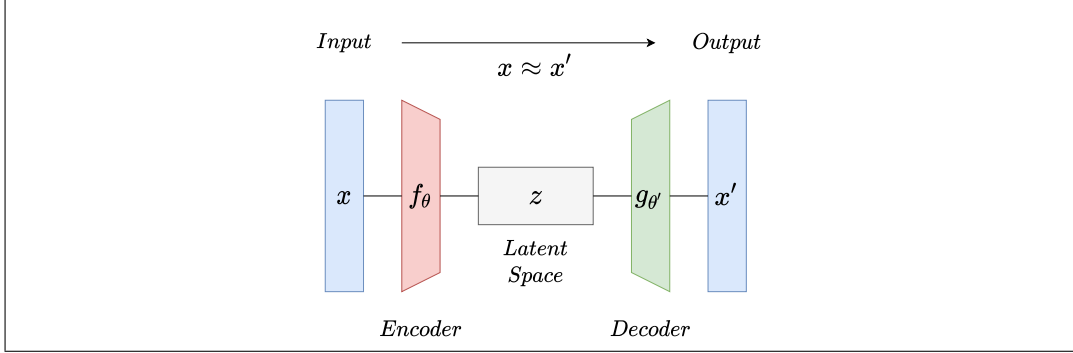


Figure 2.6: Schematic of an autoencoder model architecture.

The first applications of this type of neural networks date back to the 1980s [83, 84, 85, 86]. Autoencoders have been used for classification, clustering, anomaly detection, dimensionality reduction, and signal denoising [87]. Convolutional Autoencoders (CAEs) are a special form of Autoencoders implemented using convolutional encoding and decoding layers.

2.3.2.3 Denoising Autoencoder

Proposed by Vincent et al. [88], the Denoising Autoencoders (DAEs) are an extension of classic autoencoders where the model is taught to predict original uncorrupted data from corrupted input data, i.e., the decoder attempts to reconstruct a clean version of the corrupted input from the autoencoder latent representation.

The encoder function f takes a corrupted input $\tilde{\mathbf{x}}$ and maps it to a hidden representation \mathbf{y} computed as:

$$\mathbf{y} = f_\theta(\tilde{\mathbf{x}}) = h(\mathbf{W}\tilde{\mathbf{x}} + \mathbf{b}) \quad (2.24)$$

where h is a typically nonlinear transfer function, \mathbf{W} and \mathbf{b} are the encoder network parameters, and $\theta = (\mathbf{W}, \mathbf{b})$.

The output \mathbf{x}' , having a similar form to $\tilde{\mathbf{x}}$, is reconstructed from \mathbf{y} by the decoder g

$$\mathbf{x}' = g_{\theta'}(\mathbf{y}) = h'(\mathbf{W}'\mathbf{y} + \mathbf{b}') \quad (2.25)$$

where h' is similar to h , \mathbf{W}' and \mathbf{b}' are the decoder network parameters, and $\theta' = (\mathbf{W}', \mathbf{b}')$.

The DAE training procedure consists on learning the parameters \mathbf{W} , \mathbf{W}' , \mathbf{b} , and \mathbf{b}' that minimise the autoencoder reconstruction error between the groundtruth \mathbf{x} and the reconstruction $\mathbf{x}' = g_{\theta'}(f_\theta(\tilde{\mathbf{x}}))$, using a suitable cost function. Typically, the function is minimised using Stochastic Gradient Descent (SGD) [89] for small batches of corrupted and clean sample pairs. Figure 2.7 shows the denoising autoencoder model architecture.

Convolutional Denoising Autoencoders (CDAEs) are Denoising Autoencoders implemented using convolutional encoding and decoding layers. Because CDAEs use CNNs for extracting high-order features from images, CDAEs differ from standard DAEs in that their parameters are shared across all input image patches to maintain spatial locality. Different

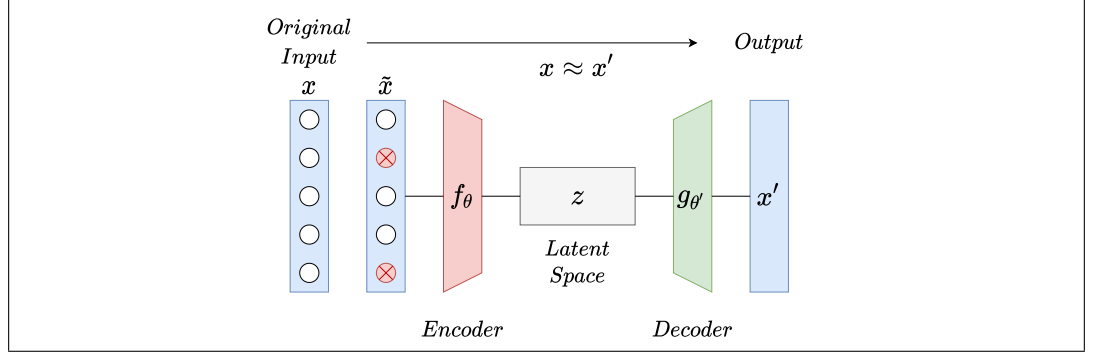


Figure 2.7: Schematic of an autoencoder model architecture.

studies show that CDAEs achieve better image processing performance when compared to standard DAEs [90, 91].

2.3.2.4 The U-Net Architecture

The U-Net is a convolutional network architecture originally design for fast and precise segmentation of images. The U-Net [92] has a encoding-decoding architecture inspired in the autoencoder with skip connections [93] that transfer the data from the encoder layers to the decoding layers. Input-output pairs are images and their desired semantic pixel labelling providing segmentation of the image in one shot.

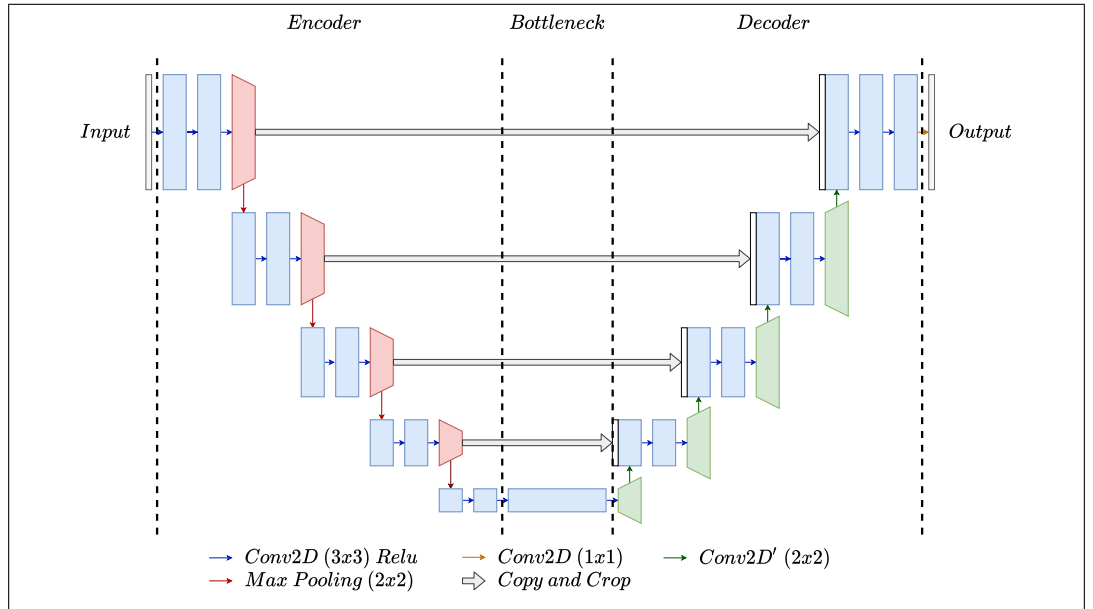


Figure 2.8: Schematic of the U-Net model architecture.

The architecture of the U-Net model is shown in Figure 2.8. Each blue box corresponds to a multi-channel feature map. White boxes represent copied feature maps. Blue and yellow arrows denote 2D convolutional operations, red boxes stands for pooling operations, green boxes denote upscaling 2D convolutional operations, and finally, gray arrows denote copy copy and crop feature map operations

This architecture has shown exceptional results for image segmentation and image restoration tasks [94, 95, 96]. Depending on the architectural modifications made to U-Net, it can be used to achieve different tasks beyond segmentation. Isola et al. [97] used U-Net as a generator to perform image-to-image translation tasks such as in the case of aerial images and their correspondence in maps or the conversion of gray-scale images to color images through adversarial learning. Jansson et al. [98] investigated the use of U-Net as a voice separator, using the magnitude of the spectrogram of the audio containing the mix of different singing voices as the input. Zhang et al. [99] modified U-Net with a residual block and proposed it as a tool for extracting roads from aerial maps.

Hypotheses and Objectives

The main goal of the thesis is to tackle the shortcomings of optical laser-based sensors in quality control processes, in particular in industrial harsh scenarios. In these industrial environments, different challenges arise as a result of the manufacturing processes. Just to cite some, fast object motion during the acquisition process may lead to blurred images and consequently an inaccurate surface reconstruction, extreme temperatures can cause additional image noise hindering real data, complex material handling and transporting produce vibrations and shocks that affect the measured surface profile, and imaging of complex geometries sometimes require of tailor made optical laser-based sensors.

This thesis reports on the design and experimental assessment of reliable dimensional quality optical laser-based sensors for two specific industrial harsh environments, a high-speed forging press where complex revolution parts are manufactured and in-line inspected between 600 and 800 °C, and a steel Cut to Length Line (CTL) where the uncoiling, levelling, measuring, cutting to length and stacking work of metal sheets take place. The modelling and calibration of the devised sensors together with the processing and filtering methods for the data provided by such devices are addressed.

3.1 Hypotheses

The following list enumerates the hypotheses of this research work:

1. **3D surface reconstruction for in-line quality control inspection of hot high-speed forged complex revolution parts.**
 - A set of three cameras, featuring a Scheimpflug configuration, and two laser planes, will provide the sufficient field of view (FOV), depth of field (DOF), and accuracy to obtain in-line 3D surface reconstructions of hot forged complex revolution parts.
 - A simplified camera-laser calibration method based on homographies under Scheimpflug conditions can be developed. If the right conditions exist, i.e., errors in the laser projections corresponding to the pixels on the border of the

image (those having largest distortions) with and without distortion are smaller than the needed precision in the reconstruction, we can discard the calculation of the accurate Scheimpflug compensation map. Thus, the calibration procedure will be simplified and will offer an industrial high degree of automation.

2. **3D surface reconstruction and denoising of metal sheets for flatness computation in a high speed CTL processing line.**

- Devising an optical sensor, composed of a CCD camera and two parallel laser lines, will enable us instantaneous, robust, and quick estimation of the surface height derivatives. Using Hermite cubic interpolation along the surface using both height information and its derivatives will provide the background to develop a real-time surface estimation and noise removal algorithm.
- The previous sensor's 3D denoised surface reconstructions can be used to train a CNN network. The trained CNN network will allow us to process surface information from an simplified sensor, composed of a CCD camera and a single laser line. It also will achieve sufficiently accurate results while simplifying the development, complexity, calibration, and price of the required sensor.

3.2 Objectives

The following list enumerates the technical objectives to be accomplished to answer to all the previously exposed hypotheses:

1. To implement a sensing setup that enables us to acquire the most accurate surface information to carry out an effective industrial quality control assessment in the two aforementioned scenarios.
2. To investigate and demonstrate the feasibility of a simple camera-laser calibration method based on homographies under Scheimpflug conditions.
3. To investigate and develop methods and algorithms that enable us to improve the quality of the surface data obtained from previous mentioned devices, filtering out, when necessary, the undesirable effects of the inherent manufacturing processes noise.
4. To design and implement the experiments that validate the feasibility of the proposed devices and methods in both theoretical and real scenarios.

3.3 Brief description of the publications and contributions

The research work is assembled in a total of four articles. Each research article focuses on accomplishing one or several technical objectives, answering the hypothesis listed above. The first two articles tackle the 3D surface reconstruction and quality control of hot high-speed forged complex revolution parts. The third and fourth articles address the 3D surface reconstruction and denoising of metal sheets in a high speed CTL processing line.

3.3.1 Article 1: A Multi Camera and Multi Laser Calibration Method for 3D Reconstruction of Revolution Parts.

(Accepted: 21 January 2021, Sensors, MDPI)

This paper describes the theoretical background for calibrating multi camera and multi laser 3D triangulation systems, particularly for those using Scheimpflug adapters, which have been implemented in the previous article. Our method uses a conical calibration object whose intersections with the laser planes generate stepped line patterns that can be used to calculate the camera-laser homographies. The calibration object has been designed to calibrate scanners for revolving surfaces, but it can be easily extended to linear setups. The experiments carried out show that the proposed system has a precision of 0.1 mm.

3.3.2 Article 2: Optical Dual Laser Based Sensor Denoising for Online Metal Sheet Flatness Measurement Using Hermite Interpolation.

(Accepted: 19 September 2020, Sensors, MDPI)

This article presents an innovative system for real-time robust surface estimation of flattened metal sheets composed of two line lasers and a conventional 2D camera. Laser plane triangulation is used for surface height retrieval along the surface. The dual laser configuration allows instantaneous robust and quick estimation of the surface height derivatives. Hermite cubic interpolation allows us to retrieve real-time surface estimation and high frequency noise removal. These noises arise from vibrations induced in the sheet by its movements during the process and some mechanical operations, such as cutting into separate pieces. The system is validated on synthetic surfaces that simulate the most critical noise sources and on real data obtained from the installation of the sensor in a production CTL line. In the comparison with conventional filtering methods, we achieve at least a 41% of improvement in the accuracy of the surface reconstruction.

3.3.3 Article 3: Depth Data Denoising in Optical Laser Based Sensors for Metal Sheet Flatness Measurement: A Deep Learning Approach.

(Accepted: 21 October 2021, Sensors, MDPI)

This paper presents a deep learning architecture for removing the specific kinds of noise from the data obtained by a laser based range sensor installed in a CTL line, in order to allow accurate flatness measurements from the clean range images. The proposed convolutional blind residual denoising network (CBRDNet) is composed of a noise estimation module and a noise removal module implemented by specific adaptation of semantic convolutional neural networks. The CBRDNet is validated on both synthetic and real noisy range image data that exhibit the most critical kinds of noise that arise throughout the metal sheet production process. Real data were obtained from a single laser line triangulation flatness sensor installed in a roll leveling and CTL line. Computational experiments over both synthetic and real datasets clearly demonstrate that CBRDNet achieves superior performance in comparison to traditional 1D and 2D filtering methods, and state-of-the-art CNN-based denoising techniques. The experimental validation results show a reduction in error than can be up to 15% relative to solutions based on traditional 1D and 2D filtering methods and between 10% and 3% relative to the other deep learning denoising architectures recently reported in the literature.

Results

This chapter presents and discusses the obtained results. First, the results concerning the sensing setup and calibration methods for the quality control of hot high-speed forged complex revolution parts are presented. A special attention is given to the proposed calibration method and accuracy results. Afterwards, the results from the 3D surface reconstruction and denoising of metal sheets in a high speed CTL processing line are summarised, drawing attention to the filtering methods, specially to the proposed CNN network that simplifies the initial hardware requirements and outperforms conventional methods and more complex and expensive sensing setups proposed by other authors.

4.1 Multi camera and multi laser sensing setup and calibration method for 3D reconstruction of forged revolution parts

In this section we report on a calibration method for a complex laser triangulation setup for industrial quality control. The following sections will provide an experimental evidence of the usefulness of the methodology on a system comprised of three cameras and two laser lines that are configured as shown in Figure 4.1 (a). This system is used to reconstruct Warm-Die forged revolution parts that are fixed in a rotating stage.

It is noteworthy that, although some authors (e.g., [100, 63]) have applied standard calibration methods based on planar objects in scenarios with Scheimpflug, it is not an easy procedure. The main difficulty is to capture images of the planar calibration pattern in which a large area of the pattern is focused, which implies that the calibration plate should be placed almost parallel to the laser plane. Furthermore, there are situations where several lasers or cameras are needed because of the geometry of the object being captured. This configuration increases the complexity of the calibration since all laser and image planes must be related to each other under the same reference system. This fact implies that the control points of the calibration pattern have to be visible at the same time by the cameras tied to the same laser. However, this may not be possible due to occlusions derived from the convergence angles of the cameras with respect to the laser plane.

4. RESULTS

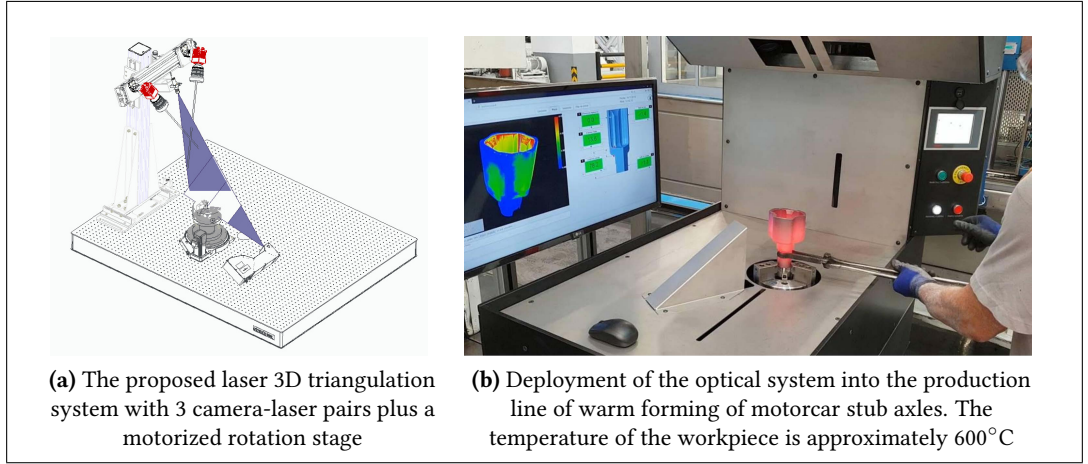


Figure 4.1: The proposed and deployed optical system for 3D Reconstruction of Warm-Die Forged Revolution Parts

We propose a calibration method that uses a 3D calibration object with a conical shape that can be used to determine the homographies [101] between laser and image planes as is shown in Figure 4.2 (a). In order to estimate these homographies, the camera distortion map under Scheimpflug conditions has to be identified, or sufficient conditions have to be met in which the distortion map calculation can be discarded.

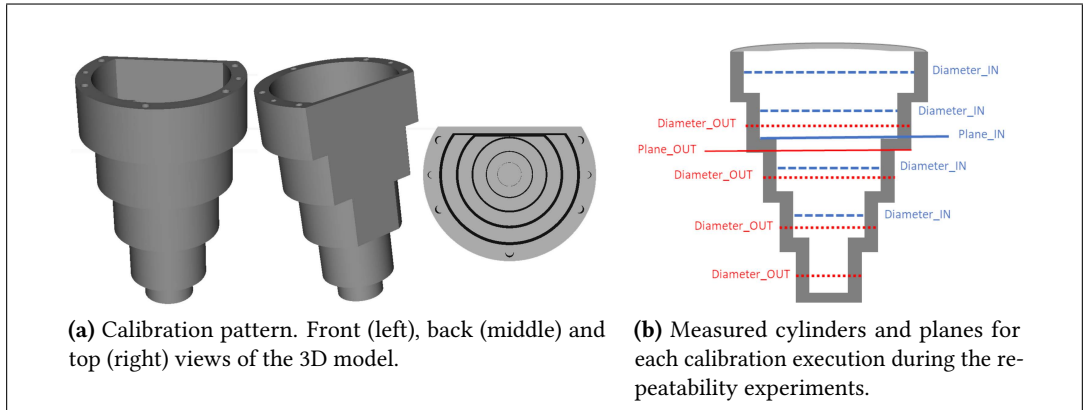


Figure 4.2: Calibration pattern and Measured planes and Cylinders during the repeatability tests

4.1.1 Scheimpflug Distortion

In our experiment an approximated Scheimpflug distortion map for the used cameras (C5-4090-GigE cameras from Automation Technology GmbH and Zeiss Planar T* 50 mm lenses from Nikon) and the estimated homography were calculated resulting in maximum errors of 2 microns. These errors comes from the fact that a similar camera but without Scheimpflug angle, i.e., perpendicular camera, has been calibrated with the same lens used in the Scheimpflug camera. A very precise dot calibration pattern with precision of about 2 microns has been used to calibrate the perpendicular camera, noticing practically no radial distortion, with a re-projection error that comes from the errors of the calibration plate. The Scheimpflug distortion map, shows distortions of a similar magnitude that the distortions of untilted camera.

4.1. Multi camera and multi laser sensing setup and calibration method for 3D reconstruction of forged revolution parts

Real calibration of the laser-camera homography was made by projecting the laser over a calibrated revolution pattern, assuming that the distortion map can be avoided. The errors obtained in the homography estimation were smaller than 7 microns. The advantage of this method resides on the fact that difficult and error-prone Scheimpflug calibration procedures can be avoided, which can at the end be more costly and less precise than this simpler method.

4.1.2 Calibration Repeatability and Accuracy

In order to demonstrate the repeatability of the proposed calibration method, we have performed the calibration 10 times. Moreover, to introduce variability in the data, the pattern has been placed in a different initial position for each calibration, providing a different set of profiles as input. At each calibration execution we have calculated the calibration data and the 3D reconstruction of two different objects: (1) the calibration pattern, and (2) an object that is similar in shape to the calibration pattern, but with a small change in the size (different height and different diameter lengths). The idea of introducing this second object is to see results without the possible effects of overfitting due to the usage of the same object for both calibration and test.

We have used these 3D reconstructions to perform some measurements and provide a comparison between them. More precisely, we have measured the diameter of several cylinders. Furthermore, the height of a plane at different locations has been estimated for the calibration pattern as well (see Figure 4.2 (b) for a graphical representation of measured cylinders and planes). In all cases we have used points of the inner and outer part of the 3D model to estimate cylinders and planes of the outer and inner parts respectively. Table 4.1 shows the error (expressed in millimetres) of these measurements respect to the nominal values, which have been obtained using a CMM (Mitutoyo Crysta-Apex S 9106, which offers a high accuracy, ~ 0.002 mm).

Measurement	Nominal	Mean	Stdev
Diameter_OUT	44.00	0.064	0.009
Diameter_OUT	71.00	0.115	0.005
Diameter_OUT	97.01	0.017	0.005
Diameter_OUT	123.00	0.059	0.016
Diameter_IN	50.94	0.031	0.008
Diameter_IN	76.95	0.067	0.041
Diameter_IN	102.95	0.084	0.087
Diameter_IN	129.00	0.180	0.047
Plane_OUT	121.96	0.194	0.014
Plane_IN	132.00	0.061	0.012

Table 4.1: Mean and standard deviation error (in mm) of some primitives (cylinders and planes) of the calibration pattern respect to nominal values using different calibrations.

As a supplementary measure of accuracy, we have calculated the distance between the 3D reconstructed model and its corresponding original 3D model for the object with similar shape. We have compared each of the previous 10 3D reconstructions of this object against its original 3D model. The mean and standard deviation of the errors of these 10

comparisons has turned out to be 0.151 mm and 0.015 mm respectively. It is noteworthy that these errors values accumulate the error of several sources (the laser, the decentering of the object on the rotation axis, the quality of the calibration and the fitting algorithm). Taking into account all the experiments presented above, we can point out that the system offers an accuracy of tenths of a millimetre with a variability of hundredths of a millimetre.

4.1.3 Real Case

As an additional evidence of the validation of the proposed system, we have made experiments with an industrial part shown in Figure 4.1 (b) that is being used in a real production environment. We have used it as a reference to validate the accuracy of the calibration. Being a result of an industrial manufacturing process, this part undergoes a series of measurements (designed and defined by expert metrologists) at some key points to ensure that the tolerances are met. These measurements are usually performed using a CMM, which offers high precision results. Thus, we have considered several of these measurements and we have calculated them using both the CMM and a metrology software which we have provided as input the scanned and reconstructed 3d model of the part using the laser 3d triangulation system described above.

Comparing the results of both alternatives, we observed that the errors are less than 0.1 mm, which indeed, is accurate enough to be used for this real application. The details of the repeatability and reproducibility (RR) experiments that led to this value can be found in [102].

4.2 Optical Laser based Sensor and Algorithms for Real Time Surface Reconstruction and Flatness Measurement in Metal Sheet Industries

In this section we present the results of an innovative system for real-time robust surface estimation of flattened metal sheets.

With the advances in computer vision technology, optical flatness sensors have become widespread [103] allowing manufacturing line human operators to measure manifest flatness, i.e., flatness not hidden by tension, at high line speeds, thus enabling real-time monitoring as well as a high degree of automation in the production phase. Most optical surface flatness inspection systems used in the metal sheet industry are based on the laser triangulation principle [104, 69].

The large real-time inspection capabilities of these optical sensors are impeded by the non-linear high-frequency fluctuations induced in the steel sheet surface by the mechanical processes that take place in the manufacturing line, the juddering of the metal strip due to forward traction, as well as the shearing processes that cut to length the sheet. Under these circumstances, achieving a highly accurate flatness measurement requires a high performance signal denoising method to be applied to the height profile captured by the 3D sensor, removing the noise corresponding to such non-linear high-frequency fluctuations. The literature [105, 106, 74, 107, 108] presents different sensors based on laser triangulation, requiring the use of two or more laser lines to filter out external noise sources and reconstruct an accurate and smooth continuous 3D map of the metal sheet surface.

4.2. Optical Laser based Sensor and Algorithms for Real Time Surface Reconstruction and Flatness Measurement in Metal Sheet Industries

In the following sections, first, we present the results coming from a noise removal method based on Hermite polynomial interpolation. This method is applied to the surface information acquired by an optical sensor featuring two parallel laser lines and a CCD camera capturing the area illuminated by the lasers. Afterwards, we present the results from our proposed CNN approach, allowing us to simplify the initially proposed sensor configuration by using only a single laser line triangulation.

4.2.1 Dual Laser Line Sensor and Hermite Interpolations Results

In this section, we assess the initially proposed dual laser line sensor and Hermite interpolation method for denoising both synthetic sheet samples and real data from the 3D flatness sensor.

4.2.1.1 Results on Synthetic Data

We created a synthetic surface showing two of the most common defects in CTL line featuring a roll leveller. A set of different computational experiments were carried out over the synthetic surface described above introducing different kinds of noise to simulate the vibrations induced in the sheet metal as a result of the mechanical elements of the CTL line. Additionally, we introduced a signal modelling the vibrations induced by a cutting station located near the scanning area, and another noise source controlled by a single parameter that simulates the triangulation error of the 3D sensor. The results obtained comparing the reconstructed surface to the theoretical noise-free surface using our filtering method, were of a maximum error of 1.15 mm and a standard deviation of 0.38 mm. These errors meet the standards to measure flatness quality in roll levelled products.

These results show that the flatness sensor and the proposed filtering method are both robust and accurate enough against different noises sources, in particular to localized high amplitude noises produced by a simulated cutting station placed after the rolling leveler and the devised 3D sensor.

For a quantitative evaluation of the improvement achieved by our proposal, we test our method against the following approaches for surface denoising, a moving-average filter featuring a sliding window of 33 samples in length, a third order low-pass Chebyshev Type II filter [109], a third order Savitzky–Golay FIR smoothing filter [31, 32] and finally, a third order Butterworth IIR digital filter [110, 111]

Table 4.2 presents the comparative results of the implemented denoising methods over the synthetic surface discussed above. Improvements in MAE achieved by our approach range from 45% relative to the Butterworth filter approach up to 50% relative to the Savitzky–Golay approach. Regarding the RMSE, our approach improves by 41% over the second best approach, and up to 49% over the Chebyshev filter.

4.2.1.2 Results on Real Industrial Data

During the experimental data acquisition, we used samples from two different kinds of steel, S235JR steel coils and S500MC high yield steel coils. The coil specimens had a length of about 800 m and width in the range [800, 2300] mm. The sensor took measurements along 3000 mm in each measurement cycle. Flatness information was highly corrupted by high frequency noisy vibrations from the cutting station and other mechanical processes

4. RESULTS

Method	MAE	MaxAE	STD	RMSE
Hermite (ours)	0.413	1.150	0.380	0.459
Butterworth	0.760	4.423	0.735	0.781
Savitzky–Golay	0.842	6.436	0.779	0.853
Moving Average	0.801	5.463	0.928	0.865
Chebyshev Type II	0.828	5.040	0.828	0.903

Table 4.2: Comparative results of our approach with other conventional denoising approaches. MAE = mean absolute error; MaxAE = maximum absolute error; STD = standard deviation of the absolute error; RMSE = root mean squared error.

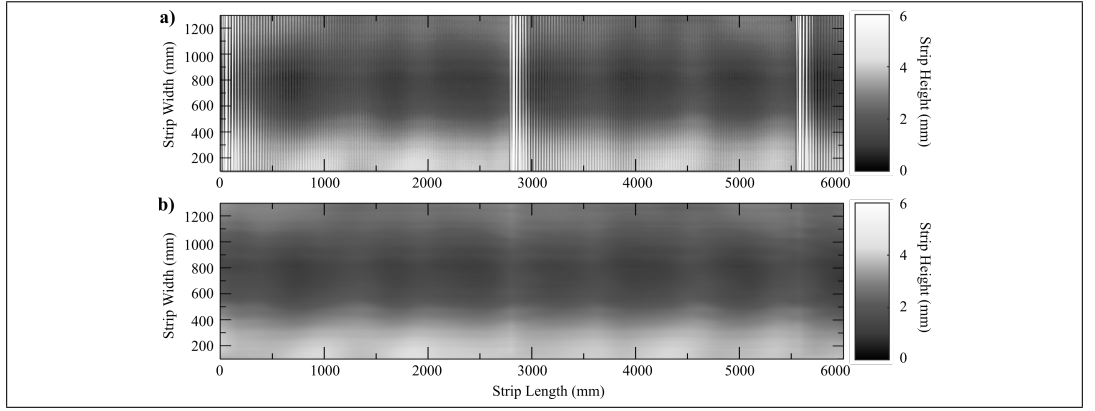


Figure 4.3: (a) Sensor raw data for a S235JR steel coil with observed high frequency transient noisy waves and background noise. (b) Denoised sensor data using the proposed Hermite interpolation filtering method.

that took place in the CTL line. Namely, the cutting station produced high amplitude/high frequency noisy waves on the metal strip a fixed time interval depending on the cutting length program, and the conveyor belt produced overall high frequency waves. The resulting interference pattern had a rather complex spatial form of noise, hindering the detection of flatness defects.

The proposed flatness measuring sensor succeeded at acquiring the surface information at the real-time production speed of 30 m/min. The Hermite polynomial filtering procedure manages to successfully retrieve the surface features of the material and the denoised flatness measures, as shown in Figures 4.3b and 4.4b, depicting the smooth reconstructed surface after the noisy waves have been removed. In Figure 4.4b, filtering unveils center buckles, i.e., another kind of common flatness defect in which sinusoidal waves restrain the central fibers of the metal sheet.

4.2.2 Single Laser Line Sensor and Deep Learning Approach Results

In this section, we assess the proposed CNN described in [112] for denoising both synthetic sheet samples and real data from the 3D flatness sensor. The proposed denoising network is employed to reconstruct both simulated and real data in order to test its ability to remove non-linear noises caused by mechanical manipulation of the metal sheet during the manufacturing process.

4.2. Optical Laser based Sensor and Algorithms for Real Time Surface Reconstruction and Flatness Measurement in Metal Sheet Industries

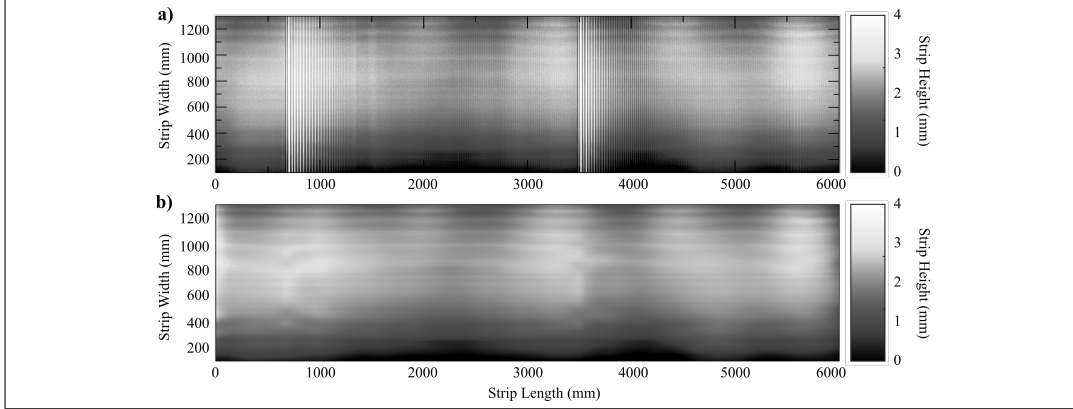


Figure 4.4: (a) Sensor raw data for a S500MC high yield steel coil with with observed periodic transient impulses and background noise. (b) Denoising results of the sensor raw data using the proposed Hermite interpolation filtering method.

The dataset used for both training and testing of the proposed architecture is composed of real production line and synthetic range image samples of steel coils from a roll levelling and shearing line. The experimental data coming from the real production line consists of 5500 samples from six different steel coils. The synthetic data are used as a kind of data augmentation aiming to improve the network denoising performance because of the difficulties faced collecting a real dataset comprising a wide range of representative samples. Additionally, in real-world measurements the metal sheet is not free from tensile stresses during the manufacturing processes causing its elongation. After cutting the metal strip in single smaller sheets, the tensile stress release results in surface deformations. Thus, measurements obtained by an offline precision measuring device like a coordinate measuring machine (CMM) cannot be used as a validation ground truth for online measurement methods, whereas synthetic samples do. We generated 5500 synthetic noisy data samples using the noise model described in Section 3 of [112]. Because we have these synthetic ground truth surfaces, we can compute the performance of our denoising method against others.

4.2.2.1 Results on Real and Synthetic Dataset Samples

To assess the performance of the proposed denoising CNN, we conducted three different comparative analyses. First, we applied some traditional 1D filtering methods such as Moving Average, Butterworth IIR [110, 111], Savitzky-Golay FIR [31, 32], Chebyshev Type II [109], and piecewise cubic Hermite interpolation [113] filters. Secondly, we applied 2D wavelet-based denoising methods. Specifically, we computed results using Daubechies, Symlets, Meyer, Coiflets, and Fejer-Korovkin wavelets [114, 115, 116]. Finally, we compared the performance of CBRDNet against some state-of-art 2D deep learning image denosing methods, specifically NERNet [117], CBDNet [118], BRDNet [119], FFDNet [120], and CDnCNN_B [121].

Table 4.3 shows the comparative results of the denoising traditional 1D filtering approaches described above when applied to the synthetic surface. MAE improvements achieved by our method range from three times better when compared to the Hermite filtering approach to 6 times better when compared to the Chebyshev filter approach. Similar improvements are achieved in term of RMSE.

4. RESULTS

Method	MAE *	MaxAE *	STD *	RMSE *
CBRDNet-ReLu (ours)	0.140	0.376	0.136	0.147
Hermite	0.413	1.150	0.380	0.459
Butterworth	0.760	4.423	0.735	0.781
Savitzky-Golay	0.842	6.436	0.779	0.853
Moving Average	0.801	5.463	0.928	0.865
Chebyshev Type II	0.828	5.040	0.828	0.903

* Measurements are expressed in millimeters (mm).

Table 4.3: Comparative results of our approach with traditional 1D denoising approaches. MAE = mean absolute error; MaxAE = maximum absolute error; STD = standard deviation of the absolute error; RMSE = root mean squared error. Best results presented in bold font.

Additionally Table 4.4 shows the comparative results of the conducted 2D wavelet-based denoising experiments. MAE improvements achieved by our method range from 2.5 times better when compared to the Fejer-Korovkin filtering approach to 1.3 times better when compared to the Symlets filter approach. Similar improvements are achieved in term of RMSE. For a graphical representation of these results refer to Section 7 in [112]

Method	MAE *	MaxAE *	STD *	RMSE *
CBRDNet-ReLu (ours)	0.140	0.376	0.136	0.147
Sym8	0.176	0.543	0.170	0.188
Coif4	0.180	0.591	0.179	0.190
Db8	0.181	0.622	0.179	0.201
Dmey	0.256	0.942	0.282	0.291
Fk8	0.390	1.998	0.588	0.390

* Measurements are expressed in millimeters (mm).

Table 4.4: Comparative results of our approach with traditional 2D denoising approaches. MAE = mean absolute error; MaxAE = maximum absolute error; STD = standard deviation of the absolute error; RMSE = root mean squared error. Best results presented in bold font.

Finally, we compared the proposed CNN architecture presented to the five earlier stated CNN-based approaches. The aforementioned architectures were trained and assessed 100 times on the same dataset to obtain the statistical results listed in Table 4.5. Furthermore, for a clearer graphical representation of denoising performance, we provide the outcomes of these methods under Section 7 in [112]. When compared to the groundtruth the CBRDNet results are very close to the real ones, MAE improvements range from 2.5 times better when compared to CDnCNN_B and 1.2 times better when compared to CBDNet. Similar improvements are measured in terms of RMSE.

4.2.2.2 Results on Real Production Environment

To evaluate the effectiveness of our CNN based denoising method in a real production environment, we carried out a set of experiments in a CTL line where the sensor and Hermite filtering method proposed by Alonso et al. [113] were deployed. Measuring results from a

4.2. Optical Laser based Sensor and Algorithms for Real Time Surface Reconstruction and Flatness Measurement in Metal Sheet Industries

Method	Blind /Non Blind	MAE *	MaxAE *	STD *	RMSE *
CBRDNet-ReLu (ours)	Blind	0.140	0.376	0.136	0.147
CBDNet	Blind	0.172	0.520	0.162	0.185
NERNet	Blind	0.184	0.499	0.175	0.195
BRDNet	Blind	0.198	0.659	0.184	0.212
FFDNet	Non Blind	0.224	0.501	0.201	0.252
CDnCNN_B	Blind	0.312	0.840	0.308	0.342

* Measurements are expressed in millimeters (mm).

Table 4.5: Comparative results of our approach with traditional 2D denoising approaches. MAE = mean absolute error; MaxAE = maximum absolute error; STD = standard deviation of the absolute error; RMSE = root mean squared error. Best results presented in bold font.

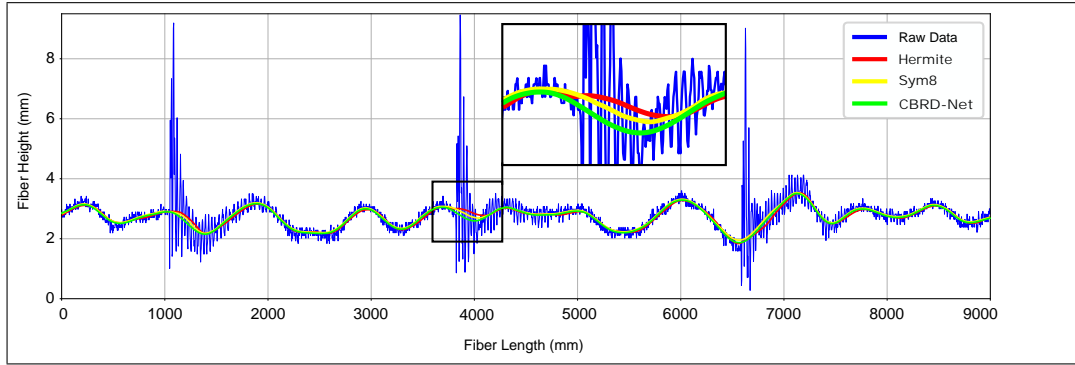


Figure 4.5: An instance of a longitudinal section of the surface reconstruction, the blue line represents the raw 1D data, the red line shows the Hermite interpolation result, the yellow line shows Symlet results, and finally the green line depicts the CBRDNet denoised result. The inset provides a better detail of the results achieved by both Hermite and CBRDNet in the highlighted area.

specimen tested out of the roll levelling system with a CMM cannot be fairly compared to those obtained by our method (Section 6 of [112]). Results obtained with the aforementioned dual laser line sensor and the Hermite filtering method have been used as groundtruth in order to evaluate the improvement of the proposed method.

Figure 4.5 depicts a longitudinal fibre, with unfiltered data collected directly from the sensor in blue, Hermite filtering in red, 2D Symlet waveletbased filtering results in yellow, and the results from the CNN proposed in this work in green. It can be seen that the method is capable of reconstructing the sheet's surface preserving the sinusoidal characteristics of the metal sheet, specially in areas where the cutting effect occurs.

These result shows graphically that the proposed method is capable of accurately reconstructing the surface of the metal sheet. When compared to state-of-the-art techniques, it achieves equivalent or better visually appealing results, as a real ground truth is always lacking in real experiments.

Conclusions and Future Work

This chapter summarises the main conclusions of this thesis, the contributions to knowledge and proposes future lines of investigation that could explore improvements over the proposed methods. Special attention will be given to the hypotheses exposed in Chapter 3 in order to confirm them.

5.1 Conclusions

This thesis, is in essence, a step forward towards a reliable and robust laser based quality control in harsh industrial environments where these optical sensors have to overcome different challenges that affect the measured surface profile. The main focus of our thesis was on the development of sensors and methods that address the difficulties of obtain an accurate smooth and noise free 3D object surface map for quality control processes. The following list enumerates the hypothesis of this research work and responds to each one of them, based on the obtained results.

1. **3D surface reconstruction for in-line quality control inspection of hot high-speed forged complex revolution parts.**

- A set of three cameras, featuring a Scheimpflug configuration, and two laser planes, will provide the sufficient field of view, depth of field, and accuracy to obtain in-line 3D surface reconstructions of hot forged complex revolution parts.

Chapter 4 section 4.1 showed that it is possible with nowadays laser based optical sensor to have enough precision to obtain a 3D surface reconstructions of hot forged complex revolution parts. Sufficient field of view, and depth of field were successfully achieved. We have reported an accuracy of few tenths of a millimetre, which could be enough for several applications.

- A simplified camera-laser calibration method based on homographies under Scheimpflug conditions can be developed. If the right conditions exist, i.e.,

errors in the laser projections corresponding to the pixels on the border of the image (those having largest distortions) with and without distortion are smaller than the needed precision in the reconstruction, we can discard the calculation of the accurate Scheimpflug compensation map. Thus, the calibration procedure will be simplified and will offer an industrial high degree of automation.

Chapter 4 section 4.1.1 and 4.1.2 showed that the proposed calibration method provides both accurateness and automatising capabilities. This method runs in less than 1 minute and provides an accuracy of few tenths of a millimetre. In order to achieve this high degree of automatism and speed in calibration, the effect of Scheimpflug distortion has not been considered. Nonetheless, as shown previously, this has little impact on accuracy when using 50 mm lenses (microns, according to our experiments). Finally, in cases where the Scheimpflug distortion cannot be avoided, simple procedures for its calculation and the conditions where it can be avoided have been also presented.

In fact, as an evidence of the potential use, this system is already being used in a real factory to control the quality of the manufacturing process of an industrial part. In this harsh industrial environment, conditions such as, the part high temperature, vibrations from the forging process, and general dirt, make the maintenance of the optical equipment a crucial factor that should be accomplished.

1. **3D surface reconstruction and denoising of metal sheets for flatness computation in a high speed CTL processing line.**

- Devising an optical sensor, composed of a CCD camera and two parallel laser lines, will enable us instantaneous, robust, and quick estimation of the surface height derivatives. Using Hermite cubic interpolation along the surface using both height information and its derivatives will provide the background to develop a real-time surface estimation and noise removal algorithm.

Chapter 4 section 4.2 showed that the devised hardware-software system is capable to carry out real time 3D surface computation of a metal strip in a CTL processing line. Online quality inspection of the strip includes the detection of flatness anomalies which are mainly low frequency variations in the height of the metal surface. The mechanical manipulation of the metal, such as the jerking due to the strip pulling and tugging, and the cutting process, induces high frequency variations that hinder the surface height information. These noises are successfully removed by our surface reconstruction system based on a Hermite interpolation approach.

Furthermore, we were able to assess the accuracy of the sensor against off-line contact sensor measurements, reporting an average error of 0.25 mm within standard industry accuracy requirements. The proposed sensor and surface reconstruction method pave the way for online closed-loop control systems, low cost real-time flatness quality inspection, and high efficiency and quality manufacture of rolled steel products.

- The previous sensor's 3D denoised surface reconstructions can be used to train a CNN network. The trained CNN network will allow us to process surface

information from an simplified sensor, composed of a CCD camera and a single laser line. It also will achieve sufficiently accurate results while simplifying the development, complexity, calibration, and price of the required sensor.

Chapter 4 section 4.2 showed that the proposed CBRDNet network is able to filter out the non-linear noise components in the range images that hinder accurate surface reconstruction and thus surface flatness measurements. Furthermore, using both real and synthetic samples of steel coils from a roll levelling cut to length line in the training process improved the network's denoising capabilities. Result showed that this network improves the 3D surface accuracy achieved with the Hermite-based method. An additional comparative analysis with wavelet-based denoising techniques. showed similar results with no clear improvement in terms of precision. However, these results must be taken with a grain of salt, because whether an optimal wavelet class and order selection might improve these results, we report results of a necessarily limited empirical exploration. To this date we do not know of such a data driven optimal wavelet design process.

5.2 Contributions to knowledge

The following list enumerates the main contributions to knowledge of the thesis:

1. **3D surface reconstruction for in-line quality control inspection of hot high-speed forged complex revolution parts.**
 - A simplified calibration method for laser camera systems configured under extreme scheimpflug conditions, allowing the scheimpflug distortion parameters to be ignored in certain scenarios.
 - A calibration procedure that relies on a conical-shaped target to simplify and automate the calibration of multiple cameras and laser planes used for 3D reconstruction of revolution parts..
2. **3D surface reconstruction and denoising of metal sheets for flatness computation in a high speed CTL processing line.**
 - An innovative surface reconstruction method based on Hermite cubic interpolation that uses range data from a dual laser based sensor as the one described in [113], This method allows us to accomplish a real-time accurate surface estimation filtering out the non-linear high-frequency fluctuations induced in the steel sheet by the mechanical processes that take place in the manufacturing CTL line.
 - A novel 3D surface reconstruction method based on a deep learning architecture. This architecture uses the range image captured by a standard single laser based sensor and the Hermite based output 3D information from the method presented in [113] as training information. This deep learning based method constitute an important step forward towards a more precise and cost-effective 3D reconstruction system. As the previous cited method, it is capable of remove the non-linear noises that occur in the metal sheet surface during its processing

in order to allow accurate flatness measurements for quality control. Furthermore, in terms of hardware complexity and costs, sensor calibration procedure, scan rate, and processing speed, this method represent and major improvement.

- When comparing our methods and results to those of older studies [107, 108, 105, 106], it must be pointed out that our methods provide better and more accurate 3D surface reconstruction. We have verified these results particularly in surface regions where high amplitude noises are induced by the mechanical processes carried out in the production line. In these regions previous proposed works struggles to obtain the "real" surface of the metal sheet.

5.3 Future Work

This section suggests possible future lines of work based on the results of the thesis, that can be summarised as it follows:

1. **3D surface reconstruction for in-line quality control inspection of hot high-speed forged complex revolution parts.**
 - The correct 3D alignment of the different laser planes required to process geometrically complex revolution parts is a challenging task, specially when high accuracy result are demanded. Moreover, precise positioning of the multiple laser planes is crucial in the 3D reconstruction process, as alignment accuracy will directly affect the accuracy of 3D reconstruction. To align a laser beam, the angular and translational displacement of the beam must be controlled. This can quickly complicate the alignment setup by requiring multiple mechanical and optical components. The above problem provide strong motivation for investigate multiple plane alignment and error compensation methods that simplify and ensure an accurate positioning of the laser planes.
2. **3D surface reconstruction and denoising of metal sheets for flatness computation in a high speed CTL processing line.**
 - One interesting continuation of the presented thesis would be to explore deep denoising architectures in the frequency domain. Although in some cases it is difficult to differentiate a signal from noise in the spatial domain, this task might be easier in the frequency domain because noisy signals can be comprised of a set of sine wave signals represented in the frequency domain with different frequencies, phases, and amplitudes. We intend to implement and compare these possible enhancements to the network outlined in this thesis in future works.
 - Some wavelet families have proven to be especially useful for noise reduction. Denoising with wavelet transforms is achieved by transforming the processed wavelet coefficients back into the spatial domain. However, most of these methods still have difficulties identifying the appropriate wavelet family and threshold parameters, which limits their capability. This opens a door for future researches, such as developing an architecture that uses the learning advantage of neural networks to select the optimal wavelet family and extract the wavelet coefficients along with the optimal denoising threshold parameters.

- Training data shortage represents a crucial issue in any deep learning project. Since data is at the core of the network training, the size of a dataset is often responsible for poor performance. To successfully train some models larger data sets are needed, but sometimes the access to real data is restricted, for example, when data becomes sensitive to its distribution, or simply, when access to real data is challenging. Under this data scarcity scenario, the development of tools capable of generating realistic synthetic data (data which contains the same schema and statistical properties as its real counterpart) would provide a solution to this data shortage. In this respect, to further our research, we plan to explore the potential of using generative models that enable us to create more realistic synthetic data samples that may be used as surrogates for real data.

Bibliography

- [1] Douglas C. Montgomery. *Introduction to statistical quality control*. Wiley, New York, NY [u.a.], 3. ed edition, 1997. See page [1](#).
- [2] Zhang W. and M. Shamsuzzaman. Design and application of integrated control charts for monitoring process mean and variance. *Journal of Manufacturing Systems*, 24(4):302–314, 2005. See page [1](#).
- [3] Karin K. Guidelines for applying statistical quality control method to monitor autocorrelated processes. *Procedia Engineering*, 69:1449–1458, 2014. 24th DAAAM International Symposium on Intelligent Manufacturing and Automation, 2013. See page [1](#).
- [4] A. Tellaeché. Three-dimensional machine vision and machine-learning algorithms applied to quality control of percussion caps. *IET Computer Vision*, 5:117–124(7), March 2011. See page [2](#).
- [5] G. Pajares. Design of a computer vision system for a differential spraying operation in precision agriculture using hebbian learning. *IET Computer Vision*, 1:93–99(6), December 2007. See page [2](#).
- [6] Hongbin J., Y.L. Murphey, Jinajun S., and Tzyy-Shuh C. An intelligent real-time vision system for surface defect detection. In *Proceedings of the 17th International Conference on Pattern Recognition, 2004. ICPR 2004*, volume 3, pages 239–242 Vol.3, 2004. See page [2](#).
- [7] L. Huanjun and W. Yaonan. Development of glass bottle inspector based on machine vision. In *2008 10th International Conference on Control, Automation, Robotics and Vision*, pages 785–790, 2008. See page [2](#).
- [8] D. Maestro-Watson, J. Balzategui, L. Eciolaza, and N. Arana-Arexolaleiba. Deflectometric data segmentation for surface inspection: a fully convolutional neural network approach. *Journal of Electronic Imaging*, 29(4):1 – 16, 2020. See page [2](#).
- [9] P. Schalk, R. Ofner, and P. O’Leary. Pipe eccentricity measurement using laser triangulation. *Image and Vision Computing*, 25(7):1194–1203, 2007. Computer Vision Applications. See page [2](#).
- [10] R. L. Silva, M. Rudek, A. L. Szejka, and O. C. Junior. Machine vision systems for industrial quality control inspections. In Paolo Chiabert, Abdelaziz Bouras, Frédéric Noël, and José Ríos, editors, *Product Lifecycle Management to Support Industry 4.0*, pages 631–641, Cham, 2018. Springer International Publishing. See page [2](#).
- [11] Wei H. and Radovan K. Development of a real-time laser-based machine vision system to monitor and control welding processes. *The International Journal of Advanced Manufacturing Technology*, 63:235–248, 2012. See page [2](#).
- [12] L. Jarzebowicz and S. Judek. 3d machine vision system for inspection of contact strips in railway vehicle current collectors. In *2014 International Conference on Applied Electronics*, pages 139–144, 2014. See page [2](#).
- [13] F. Aggogeri, N. Pellegrini, and F. L. Tagliani. Recent advances on machine learning applications in machining processes. *Applied Sciences*, 11(18), 2021. See page [2](#).

BIBLIOGRAPHY

- [14] J. Park, B. Kwon, and D. Kang. Machine learning-based imaging system for surface defect inspection. *International Journal of Precision Engineering and Manufacturing-Green Technology*, 3(3):303–310, Jul 2016. See page 2.
- [15] T. Wang, Y. Chen, M. Qiao, and H. Snoussi. A fast and robust convolutional neural network-based defect detection model in product quality control. *The International Journal of Advanced Manufacturing Technology*, 94(9):3465–3471, Feb 2018. See page 2.
- [16] L. Yi, G. Li, and M. Jiang. An end-to-end steel strip surface defects recognition system based on convolutional neural networks. *Steel Research International*, 88, 04 2016. See page 2.
- [17] Y. . Zhao, Y. H. Yan, and K. C. Song. Vision-based automatic detection of steel surface defects in the cold rolling process: considering the influence of industrial liquids and surface textures. *The International Journal of Advanced Manufacturing Technology*, 90(5):1665–1678, May 2017. See page 2.
- [18] *Brief History of Research on Vision*, chapter 2, pages 9–14. John Wiley Sons, Ltd, 2009. See page 3.
- [19] D. C. Brown. Decentering distortion of lenses. volume 32, pages 4445–462. See page 5.
- [20] D. C. Brown. Close-range camera calibration. *Photogrammetric Engineering*, 37(8):855–866, 1971. See page 5.
- [21] A. E. Conrady. Decentred Lens-Systems. *Monthly Notices of the Royal Astronomical Society*, 79(5):384–390, 03 1919. See page 5.
- [22] M. C. Amann, T. Bosch, M. Lescure, R. Myllylä, and M. Rioux. Laser ranging, a critical review of usual techniques for distance measurement. *Opt. Eng.*, 2001:10–19, 2001. See page 6.
- [23] G. Zhang, J. He, and X. Li. 3d vision inspection for internal surface based on circle structured light. *Sensors Actuators Phys.*, 2005:68–75, 2005. See page 6.
- [24] R. A. A Jarvis. Perspective on range finding techniques for computer vision. *IEEE Trans. Pattern Anal. Mach. Intell.*, 1983:122–139. See page 6.
- [25] J. L. Mundy and G. B. A Porter. Three-dimensional sensor based on structured light. In *Three-Dimensional Machine Vision*, pages 3–61. Boston, MA, USA., Springer US, 1987. See page 6.
- [26] A. Miks, J. Novak, and P. Novak. Analysis of imaging for laser triangulation sensors under scheimpflug rule. *Opt. Express*, 2013:18225–18235. See page 6.
- [27] J. F. Collado. *New Methods for Triangulation-Based Shape Acquisition using Laser Scanners*. Girona, Spain, Universitat de Girona, 2004. See page 7.
- [28] R. B. Fisher and D. K. A Naidu. Comparison of algorithms for subpixel peak detection. In *Image Technology: Advances in Image Processing, Multimedia and Machine Vision*, pages 385–404. Berlin/Heidelberg, Germany., Springer, 1996. See page 7.
- [29] K. Haug and G Pritschow. Robust laser-stripe sensor for automated weld-seam-tracking in the shipbuilding industry. In *IECON 'Proceedings of the 24th Annual Conference of the IEEE Industrial Electronics Society (Cat. No.98CH36200)*, Los Alamitos, CA, USA, 31 –4 September 1998, 98:1236–1241, August 1998. See page 7.
- [30] J. Forest, J. Salvi, E. Cabruja, and C. Pous. Laser stripe peak detector for 3d scanners. a fir filter approach. In *Proceedings of the 17th International Conference on Pattern Recognition*, Cambridge, UK, 26–26 August 2004; volume 3. *p*, pages 646–649. See page 7.
- [31] Abraham. Savitzky and M. J. E. Golay. Smoothing and differentiation of data by simplified least squares procedures. *Analytical Chemistry*, 36(8):1627–1639, 1964. See pages 7, 27, and 29.
- [32] Ronald W. Schafer. What is a savitzky-golay filter? [lecture notes]. *IEEE Signal Processing Magazine*, 28(4):111–117, 2011. See pages 7, 27, and 29.

-
- [33] A. G. Flesia, Ames, g.; Bergues, g.; Canali, l.; Schurrer, c. *Sub-pixel straight lines detection for measuring through machine vision*, 2014:402–406, May 2014. See page 7.
 - [34] N. Aggarwal and W. C. Karl. Line detection in images through regularized hough transform. *IEEE Trans. Image Process*, 2000:582–591. See page 7.
 - [35] M. Hagara and P. Kulla. Edge detection with sub-pixel accuracy based on approximation of edge with erf function. *Radioengineering*, 2011:516–524. See page 7.
 - [36] R. A. Tsai. Versatile camera calibration technique for high-accuracy 3d machine vision metrology using off-the-shelf tv cameras and lenses. *IEEE J. Robot. Autom*, 1987:323–344. See page 8.
 - [37] J. Salvi, X. Armangué, and J. A. Batlle. comparative review of camera calibrating methods with accuracy evaluation. *Pattern Recognit*, 2002:1617–1635. See page 8.
 - [38] R. C. Bolles, Kremers, j. H.; Cain, R.A. *A Simple Sensor to Gather Three-Dimensional Data*; Technical Report; AI Center, SRI International: Menlo Park, CA, USA, 1981. See page 8.
 - [39] C. H. Chen and A. C. Modelling and Kak. and calibration of a structured light scanner for 3d robot vision. In *Proceedings of the IEEE Conference on Robotics and Automation*, Raleigh, NC, USA, 31 March–3 April 1987; . p, pages 807–815. See page 8.
 - [40] M. Chiarella and K. A. Pietrzak. *An accurate calibration technique for 3-D laser stripe sensors*. Bellingham, WA, USA, In *Optics, Illumination, and Image Sensing for Machine Vision IV*; International Society for Optics and Photonics, 1990. See page 8.
 - [41] Duffy. In *IEE Proc. Vision Image Signal Process*, pages 244–248, G.; Lokier, J. Laser-video scanner calibration without the use of a frame store. 1998, 145, author = Tiddeman, B. N.; Rabey. See page 8.
 - [42] D. Q. Huynh, R. A. Owens, and P. E. Hartmann. Calibrating a structured light stripe system: A novel approach. *Int. J. Comput. Vis*, 1999:73–86. See page 8.
 - [43] F. Zhou and G. Zhang. Complete calibration of a structured light stripe vision sensor through planar target of unknown orientations. *Image Vis. Comput*, 2005:59–67. See page 8.
 - [44] I. D. Reid. Projective calibration of a laser-stripe range finder. *Image Vis. Comput*, 1996:659–666. See page 8.
 - [45] F. W. DePiero and M. M. Trivedi. *3-D Computer Vision Using Structured Light: Design, Calibration, and Implementation Issues*, volume 43. Amsterdam, The Netherlands, pp. 243–278, Elsevier, 1996. See page 8.
 - [46] E. Trucco, R. B. Fisher, A. W. Fitzgibbon, and D. Calibration Naidu. data consistency and model acquisition with laser stripers. *Int. J. Comput. Integr. Manuf*, 1998:293–310. See page 8.
 - [47] R.I. Hartley. In defense of the eight-point algorithm. *IEEE Transactions on Pattern Analysis and Machine Intelligence*, 19(6):580–593, 1997. See page 9.
 - [48] Z. Zhang. A flexible new technique for camera calibration. *IEEE Transactions on Pattern Analysis and Machine Intelligence*, 22(11):1330–1334, 2000. See page 9.
 - [49] J. Heikkila. Geometric camera calibration using circular control points. *IEEE Transactions on Pattern Analysis and Machine Intelligence*, 22(10):1066–1077, 2000. See page 9.
 - [50] Shuming Yang, Xinyu Shi, Guofeng Zhang, and Changshuo Lv. A dual-platform laser scanner for 3d reconstruction of dental pieces. *Engineering*, 4(6):796–805, 2018. See page 9.
 - [51] J Santolaria, D Guillomía, C. Cajal, J. A. Albajez, and J J. Aguilar. Modelling and calibration technique of laser triangulation sensors for integration in robot arms and articulated arm coordinate measuring machines. *Sensors*, 9(9):7374–7396, 2009. See page 9.
 - [52] L. Song, S. Sun, Y. Yang, X. Zhu, Q. Guo, and H. Yang. A multi-view stereo measurement system based on a laser scanner for fine workpieces. *Sensors*, 19(2), 2019. See page 9.

BIBLIOGRAPHY

- [53] A. Picon, A. Bereciartua, J. A. Gutierrez, and J. Perez. 3d high precision tube bevel measurement using laser based rotating scanner. In *2006 IEEE Conference on Emerging Technologies and Factory Automation*, pages 1190–1197, 2006. See page 9.
- [54] H Gross. *Handbook of Optical Systems: Optical System*, chapter 10, pages 425–483. John Wiley Sons, Ltd. See page 10.
- [55] T. Scheimpflug. Process and apparatus for the methodical distortion of flat images by photographic means with any type of lens., Austria. Patent No. AT20299B, Mar. 12, 1902. See page 10.
- [56] T. Scheimpflug. Device for methodical distortion of flat images by optical means with any lens system., Austria. Patent No. AT20299B, Nov. 11, 1902. See page 10.
- [57] T. Scheimpflug. Method of distorting plane images by means of lenses or mirrors, U.S. Patent No. 751,347, Feb. 2, 1904. See page 10.
- [58] T. Scheimpflug. Improved method and apparatus for the systematic alteration or distortion of plane pictures and images by means of lenses and mirrors for photography and for other purposes, GB Patent No. 1196. May 12, 1904. See page 10.
- [59] J. Carpentier. Improvements in enlarging or like cameras, GB Patent No. 1139. Feb. 11, 1901. See page 10.
- [60] L. Evens. View camera geometry, 2008. See page 10.
- [61] H.M. Merklinger. *Focusing the View Camera: A Scientific Way to Focus the View Camera and Estimate Depth of Field*. H.M. Merklinger, 1993. See page 10.
- [62] P. Cornic, C. Illoul, A. Cheminet, G. Le Besnerais, F. Champagnat, Y. Le Sant, and B. Leclaire. Another look at volume self-calibration: calibration and self-calibration within a pinhole model of scheimpflug cameras. *Measurement Science and Technology*, 27(9):094004, 2016. See page 10.
- [63] A. Legarda, A. Izaguirre, N. Arana-Arexolaleiba, and A. Iturrospe. Comparison and error analysis of the standard pin-hole and scheimpflug camera calibration models. pages 1–6, 06 2013. See pages 11, 23.
- [64] H. Álvarez, M. Alonso, J. R. Sánchez, and A. Izaguirre. A multi camera and multi laser calibration method for 3d reconstruction of revolution parts. *Sensors*, 21(3), 2021. See page 11.
- [65] F. Bernardini, C. L. Bajaj, J. Chen, and D. R. Schikore. Automatic reconstruction of 3d cad models from digital scans. *International Journal of Computational Geometry & Applications*, 09(04n05):327–369, 1999. See page 11.
- [66] Tamás V., Ralph R. M., and Jordan C. Reverse engineering of geometric models—an introduction. *Computer-Aided Design*, 29(4):255–268, 1997. Reverse Engineering of Geometric Models. See page 11.
- [67] L. Humbert, J. A De Guise, B. Aubert, B. Godbout, and W. Skalli. 3d reconstruction of the spine from biplanar x-rays using parametric models based on transversal and longitudinal inferences. *Medical engineering & physics*, 31(6):681–687, 2009. See page 11.
- [68] Zhiliang M. and Shilong L. A review of 3d reconstruction techniques in civil engineering and their applications. *Advanced Engineering Informatics*, 37:163–174, 2018. See page 11.
- [69] P. Siekański, K. Magda, K. Malowany, J. Rutkiewicz, A. Styk, J. Krześlowski, T. Kowaluk, and A. Zagórski. On-line laser triangulation scanner for wood logs surface geometry measurement. *Sensors*, 19(5), 2019. See pages 11, 26.
- [70] J. Goodman. Statistical properties of laser speckle patterns. *Laser Speckle and Related Phenomena*, 9:57, 12 1963. See page 11.

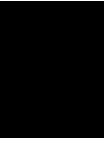
-
- [71] G. Häusler and S. Ettl. Limitations of optical 3d sensors. In *Optical measurement of surface topography*, pages 23–48. Springer, 2011. See page [11](#).
 - [72] J. Molleda, R. Usamentiaga, and D. F. García. On-line flatness measurement in the steelmaking industry. *Sensors (Basel, Switzerland)*, 13:10245 – 10272, 2013. See page [11](#).
 - [73] M. Mafi, H. Martin, M. Cabrerizo, J. Andrian, A. Barreto, and M. Adjouadi. A comprehensive survey on impulse and gaussian denoising filters for digital images. *Signal Processing*, 157:236–260, 2019. See page [11](#).
 - [74] Franz P. 3d surface acquisition and reconstruction for inspection of raw steel products. *Computers in Industry*, 56(8):876–885, 2005. Machine Vision Special Issue. See pages [12](#), [26](#).
 - [75] M. Brajović and I. Stanković, S. and Orović. Analysis of noisy coefficients in the discrete hermite transform domain with application in signal denoising and sparse signal reconstruction. *Signal Processing*, 150:145–156, 2018. See page [12](#).
 - [76] J. F. Hughes, A. van Dam, M. McGuire, D. F. Sklar, J. D. Foley, S. Feiner, and K. Akeley. *Computer Graphics: Principles and Practice*. Addison-Wesley, Upper Saddle River, NJ, 3 edition, 2013. See page [12](#).
 - [77] A.J. Jerri. The shannon sampling theorem—its various extensions and applications: A tutorial review. *Proceedings of the IEEE*, 65(11):1565–1596, 1977. See page [12](#).
 - [78] S. C. Kleene. Representation of events in nerve nets and finite automata. Number 34, pages 3–41, 1956. See page [12](#).
 - [79] F. Rosenblatt. The perceptron: A probabilistic model for information storage and organization in the brain. *Psychological Review*, 65(6):386–408, 1958. See page [12](#).
 - [80] Y. LeCun, B. Boser, J. S. Denker, D. Henderson, R. E. Howard, W. Hubbard, and L. D. Jackel. Backpropagation Applied to Handwritten Zip Code Recognition. *Neural Computation*, 1(4):541–551, 12 1989. See page [14](#).
 - [81] Alex Krizhevsky, Ilya Sutskever, and Geoffrey E Hinton. Imagenet classification with deep convolutional neural networks. In F. Pereira, C.J. Burges, L. Bottou, and K.Q. Weinberger, editors, *Advances in Neural Information Processing Systems*, volume 25. Curran Associates, Inc., 2012. See page [14](#).
 - [82] Jia Deng, Wei Dong, Richard Socher, Li-Jia Li, Kai Li, and Li Fei-Fei. Imagenet: A large-scale hierarchical image database. In *2009 IEEE Conference on Computer Vision and Pattern Recognition*, pages 248–255, 2009. See page [14](#).
 - [83] G. E Hinton and R. S Zemel. Autoencoders, minimum description length, and helmholtz free energy. *Advances in neural information processing systems*, 6:3–10, 1994. See page [15](#).
 - [84] G. E. Hinton and R. R. Salakhutdinov. Reducing the dimensionality of data with neural networks. *Science*, 313(5786):504–507, 2006. See page [15](#).
 - [85] I Goodfellow, Y Bengio, and A. Courville. *Deep Learning*. MIT Press, 2016. See page [15](#).
 - [86] Jürgen S. Deep learning in neural networks: An overview. *Neural Networks*, 61:85–117, 2015. See page [15](#).
 - [87] Dor Bank, Noam Koenigstein, and Raja Giryes. Autoencoders, 2021. See page [15](#).
 - [88] P. Vincent, H. Larochelle, Y. Bengio, and P. A. Manzagol. Extracting and composing robust features with denoising autoencoders. In *Proceedings of the 25th International Conference on Machine Learning, ICML ’08*, page 1096–1103, New York, NY, USA, 2008. Association for Computing Machinery. See page [15](#).
 - [89] Sebastian Ruder. An overview of gradient descent optimization algorithms, 2017. See page [15](#).

- [90] L. Gondara. Medical image denoising using convolutional denoising autoencoders. In *2016 IEEE 16th International Conference on Data Mining Workshops (ICDMW)*, pages 241–246, Los Alamitos, CA, USA, dec 2016. IEEE Computer Society. See page 16.
- [91] Jonathan Masci, Ueli Meier, Dan Cireşan, and Jürgen Schmidhuber. Stacked convolutional auto-encoders for hierarchical feature extraction. In Timo Honkela, Włodzisław Duch, Mark Girolami, and Samuel Kaski, editors, *Artificial Neural Networks and Machine Learning – ICANN 2011*, pages 52–59, Berlin, Heidelberg, 2011. Springer Berlin Heidelberg. See page 16.
- [92] Olaf Ronneberger, Philipp Fischer, and Thomas Brox. U-net: Convolutional networks for biomedical image segmentation. In Nassir Navab, Joachim Hornegger, William M. Wells, and Alejandro F. Frangi, editors, *Medical Image Computing and Computer-Assisted Intervention – MICCAI 2015*, pages 234–241, Cham, 2015. Springer International Publishing. See page 16.
- [93] Hao Li, Zheng Xu, Gavin Taylor, and Tom Goldstein. Visualizing the loss landscape of neural nets. *CoRR*, abs/1712.09913, 2017. See page 16.
- [94] Hiya Roy, Subhajit Chaudhury, Toshihiko Yamasaki, Danielle DeLatte, Makiko Ohtake, and Tatsuki Hashimoto. Lunar surface image restoration using u-net based deep neural networks, 2019. See page 17.
- [95] Sehyung Lee, Makiko Negishi, Hidetoshi Urakubo, Haruo Kasai, and Shin Ishii. Mu-net: Multi-scale u-net for two-photon microscopy image denoising and restoration. *Neural Networks*, 125:92–103, 2020. See page 17.
- [96] Rina Komatsu and Tad Gonsalves. Comparing u-net based models for denoising color images. *AI*, 1(4):465–486, 2020. See page 17.
- [97] Phillip Isola, Jun-Yan Zhu, Tinghui Zhou, and Alexei Efros. Image-to-image translation with conditional adversarial networks. pages 5967–5976, 07 2017. See page 17.
- [98] Andreas Jansson, Eric Humphrey, Nicola Montecchio, Rachel Bittner, Aparna Kumar, and Tillman Weyde. Singing voice separation with deep u-net convolutional networks. 2017. See page 17.
- [99] Zhengxin Zhang, Qingjie Liu, and Yunhong Wang. Road extraction by deep residual u-net. *IEEE Geoscience and Remote Sensing Letters*, 15(5):749–753, May 2018. See page 17.
- [100] A. Legarda, A. Izaguirre, N. Arana-Arexolaleiba, and A. Iturrospe. A new method for scheimpflug camera calibration. 06 2011. See page 23.
- [101] T. Fournel, J.-M. Lavest, S. Coudert, and F. Collange. Self-calibration of piv video-cameras in scheimpflug condition. In M. Stanislas, J. Westerweel, and J. Kompenhans, editors, *Particle Image Velocimetry: Recent Improvements*, pages 391–405, Berlin, Heidelberg, 2004. Springer Berlin Heidelberg. See page 24.
- [102] D. Mejia-Parra, J. R. Sánchez, O. Ruiz-Salguero, M. Alonso, A. Izaguirre, E. Gil, J. Palomar, and J. Posada. In-line dimensional inspection of warm-die forged revolution workpieces using 3d mesh reconstruction. *Applied Sciences*, 9(6), 2019. See page 26.
- [103] J. Jouet, G. Francois, G. Tourscher, and B. de Lamberterie. Automatic flatness control at solmer hot strip mill using the lasershape sensor. *Iron Steel Eng.*, 65(8):50–56, 1988. See page 26.
- [104] Marianne Chiarella and Kenneth A. Pietrzak. An Accurate Calibration Technique for 3D Laser Stripe Sensors. In Donald J. S., editor, *Optics, Illumination, and Image Sensing for Machine Vision IV*, volume 1194, pages 176 – 185. International Society for Optics and Photonics, SPIE, 1990. See page 26.
- [105] P. Kierkegaard and L.-A. Classon. A new-generation optical flatness measurement system. *Iron and Steel Technology*, 12:76–81, 12 2015. See pages 26, 36.

-
- [106] Pär Kierkegaard. Developments and benefits from optical flatness measurement in strip processing lines. In *Congreso y Exposición Nacional de la Industria del Acero, CONAC*, pages 1–15, 2016. See pages 26, 36.
 - [107] J. Usamentiaga, R. Molleda, D. F. Garcia, and G. B. Francisco. Removing vibrations in 3d reconstruction using multiple laser stripes. *Optics and Lasers in Engineering*, 53:51–59, 2014. See pages 26, 36.
 - [108] Usamentiaga R. and D. F. Garcia. Robust registration for removing vibrations in 3d reconstruction of web material. *Optics and Lasers in Engineering*, 68:135–148, 2015. See pages 26, 36.
 - [109] L. Weinberg and P. Slepian. Takahasi’s results on tchebycheff and butterworth ladder networks. *IRE Transactions on Circuit Theory*, 7(2):88–101, 1960. See pages 27, 29.
 - [110] Stephen Butterworth et al. On the theory of filter amplifiers. *Wireless Engineer*, 7(6):536–541, 1930. See pages 27, 29.
 - [111] A.V. Oppenheim, R.W. Schafer, J.R. Buck, and L. Lee. *Discrete-time Signal Processing*. Prentice Hall international editions. Prentice Hall, 1999. See pages 27, 29.
 - [112] M. Alonso, D. Maestro, A. Izaguirre, I. Andonegui, and M. Graña. Depth data denoising in optical laser based sensors for metal sheet flatness measurement: A deep learning approach. *Sensors*, 21(21), 2021. See pages 28, 29, 30, and 31.
 - [113] M. Alonso, A. Izaguirre, I. Andonegui, and M. Graña. Optical dual laser based sensor denoising for online metal sheet flatness measurement using hermite interpolation. *Sensors*, 20(18), 2020. See pages 29, 30, and 35.
 - [114] Ingrid Daubechies. *Ten Lectures on Wavelets*. Society for Industrial and Applied Mathematics, USA, 1992. See page 29.
 - [115] Y. Meyer. *Ondelettes et opérateurs*. Number v. 1 in Actualités mathématiques. Hermann, 1990. See page 29.
 - [116] Morten Nielsen. On the construction and frequency localization of finite orthogonal quadrature filters. *Journal of Approximation Theory*, 108(1):36–52, 2001. See page 29.
 - [117] Bingyang Guo, Kechen Song, Hongwen Dong, Yunhui Yan, Zhibiao Tu, and Liu Zhu. Nernet: Noise estimation and removal network for image denoising. *Journal of Visual Communication and Image Representation*, 71:102851, 2020. See page 29.
 - [118] Shi Guo, Zifei Yan, K. Zhang, W. Zuo, and Lei Zhang. Toward convolutional blind denoising of real photographs. *2019 IEEE/CVF Conference on Computer Vision and Pattern Recognition (CVPR)*, pages 1712–1722, 2019. See page 29.
 - [119] Chunwei Tian, Yinlong Xu, and W. Zuo. Image denoising using deep cnn with batch renormalization. *Neural networks*, 121:461–473, 2020. See page 29.
 - [120] K. Zhang, W. Zuo, and Lei Zhang. Ffdnet: Toward a fast and flexible solution for cnn-based image denoising. *IEEE Transactions on Image Processing*, 27:4608–4622, 2018. See page 29.
 - [121] Kai Zhang, Wangmeng Zuo, Yunjin Chen, Deyu Meng, and Lei Zhang. Beyond a gaussian denoiser: Residual learning of deep cnn for image denoising. *IEEE Transactions on Image Processing*, 26(7):3142–3155, Jul 2017. See page 29.

CHAPTER

6



Appendix

**6.1 Publication 1: A Multi Camera and Multi Laser
Calibration Method for 3D Reconstruction of
Revolution Parts**

Article

A Multi Camera and Multi Laser Calibration Method for 3D Reconstruction of Revolution Parts

Hugo Álvarez ^{1,*}, Marcos Alonso ^{2,3}, Jairo R. Sánchez ¹ and Alberto Izaguirre ²

¹ Vicomtech Foundation, Basque Research and Technology Alliance (BRTA), Parque Científico y Tecnológico de Gipuzkoa, Paseo Mikeletegi 57, 20009 San Sebastián, Spain; jrsanchez@vicomtech.org

² Robotics and Automation Group, ECS Department, Mondragon University, Loramendi Kalea 4, 20500 Mondragon, Spain; malonson@mondragon.edu (M.A.); aizagirre@mondragon.edu (A.I.)

³ Computational Intelligence Group, CCIA Department, UPV/EHU, Paseo Manuel de Lardizabal 1, 20018 San Sebastian, Spain

* Correspondence: halvarez@vicomtech.org

Abstract: This paper describes a method for calibrating multi camera and multi laser 3D triangulation systems, particularly for those using Scheimpflug adapters. Under this configuration, the focus plane of the camera is located at the laser plane, making it difficult to use traditional calibration methods, such as chessboard pattern-based strategies. Our method uses a conical calibration object whose intersections with the laser planes generate stepped line patterns that can be used to calculate the camera-laser homographies. The calibration object has been designed to calibrate scanners for revolving surfaces, but it can be easily extended to linear setups. The experiments carried out show that the proposed system has a precision of 0.1 mm.

Keywords: optical sensor; laser sensor; calibration; 3D reconstruction



Citation: Álvarez, H.; Alonso, M.; Sánchez, J.R.; Izaguirre, A. A Multi Camera and Multi Laser Calibration Method for 3D Reconstruction of Revolution Parts. *Sensors* **2021**, *21*, 765. <https://doi.org/10.3390/10.3390/s21030765>

Academic Editor: Giovanni Agati and Steve Vanlanduit

Received: 4 December 2020

Accepted: 21 January 2021

Published: 24 January 2021

Publisher's Note: MDPI stays neutral with regard to jurisdictional claims in published maps and institutional affiliations.



Copyright: © 2021 by the authors. Licensee MDPI, Basel, Switzerland. This article is an open access article distributed under the terms and conditions of the Creative Commons Attribution (CC BY) license (<https://creativecommons.org/licenses/by/4.0/>).

1. Introduction

In the context of laser triangulation systems, the calibration of the different optical elements is critical for the accuracy of the obtained reconstructions. These systems are composed by a laser line that forms a plane that intersects with the object being measured, and a camera that captures the produced laser line interception. The calibration of these elements involves the characterization of the camera parameters and the relationship between image and laser planes.

Standard calibration methods, usually referred as “sheet of light calibration”, are based mainly on two methods. The former uses planar objects with chessboard or circular patterns that are used to calculate all the calibration parameters simultaneously [1–5]. Detecting these control points in the image allows obtaining the camera parameters and the pose of the calibration object with respect to the camera. At the same time, the detection of the projection of the laser plane in the calibration pattern enables us to estimate its pose with respect to the camera, completely characterizing the triangulation system. The latter employs a moving part whose geometry (usually a diamond shaped object) is well known [6]. Nevertheless, the motion of the part has to be well controlled, e.g., by means of an accurate stepper motor.

Besides that, the depth of field of standard cameras is centered on a world plane that is parallel to the image sensor. However, laser camera systems should have the depth of field focused on the laser plane. For these cases, the lens is usually tilted with respect to the image plane through the use of an adapter (or analogously, the image sensor is tilted with respect to the lens) to ensure that the desired world plane is correctly focused (Scheimpflug principle [5]). It is noteworthy that, although some authors (e.g., [2,4]) have applied standard calibration methods based on planar objects in scenarios with Scheimpflug, it is not an easy procedure. The main difficulty is to capture images of the planar calibration

pattern in which a large area of the pattern is focused, which implies that the calibration plate should be placed almost parallel to the laser plane. Furthermore, there are situations where several lasers or cameras are needed because of the geometry of the object being captured. This configuration increases the complexity of the calibration since all laser and image planes must be related to each other under the same reference system. This fact implies that the control points of the calibration pattern have to be visible at the same time by the cameras tied to the same laser. However, this may not be possible due to occlusions derived from the convergence angles of the cameras with respect to the laser plane.

In this work, we address the calibration of a laser triangulation system composed by three cameras and two laser lines that are configured as shown in Figure 1. This system is used to reconstruct revolution parts that are fixed in a rotating stage.

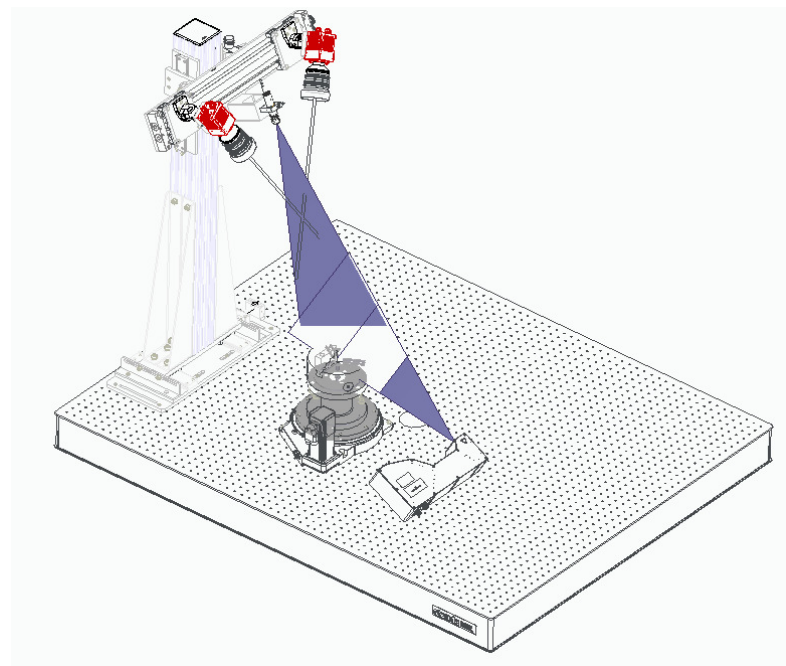


Figure 1. The proposed laser 3D triangulation system with 3 camera-laser pairs plus a motorized rotation stage. Two cameras and one laser have been placed at the top (to obtain the reconstruction of the interior of the object), while the remaining camera and laser have been placed at the bottom (to reconstruct the external surface of the object). The rotation stage ensures visibility throughout 360 degrees of the object.

Taking this into account, we propose a calibration method that uses a 3D calibration object with a conical shape that can be used to determine the homographies [7] between laser and image planes. In order to estimate these homographies, the camera undistortion map under Scheimpflug conditions has to be identified, or sufficient conditions have to be met in which the undistortion map calculation can be discarded.

In this paper, we present a more detailed investigation of camera-laser calibration based on homographies under Scheimpflug conditions. Section 2 provides related work in camera-laser triangulation. Section 3 explains an overview of the employed calibration methodology. Section 4 summarizes the practical calibration of the real setup. Section 5 describes the usage of the 3D reconstruction system. Section 6 provides experiments and discussion, and finally, Section 7 enumerates conclusions. Additionally, please refer to [8] to see a complementary work that provides an industrial application of the presented optical system.

2. Related Work

A 3D triangulation system is composed of at least one laser and one camera. However, it is common to find solutions that combine multiple lasers [9–12], lasers of different colors [13] or multiple cameras [14,15] to extend the range of visibility and avoid blind areas.

Moreover, the 3D triangulation systems are generally combined with external actuators such as linear stepper motors [10,12,13,15], turntables [9,10,15–17] or robotic arms [11,18] to extend the scanning line to a wider regions.

There are several solutions in the literature to calibrate a 3D triangulation system identifying the relative pose between each of the devices forming the system. Although some of them perform a self-calibration (no calibration object is required), these alternatives do not recover the scale of the scene and are not of interest to this work (see [5] for an in-depth explanation). The most common way to calibrate a 3D triangulation system is to use a calibration target. Because of its simplicity and good performance, planar targets are very popular, especially chessboards [10,12,14,16] and those with dot patterns [11,13]. In some cases planar targets are not a feasible solution (for example, in an arrangement where the planar pattern cannot be seen by all cameras simultaneously), so a 3D calibration target is used instead. These 3D calibration objects are specific to each application and can be of different shapes and sizes, such as a stepped [15] or creased [18] gauge, a 3D cube with a white mark in the middle [15], a 3D sphere [17], or a 3D cone [9], among others. Regardless of the calibration object, the overall calibration procedure is similar, cameras capture the projection of the laser lines on the calibration target at different points of views (controlled by the external actuators) to identify some control points with known 3D coordinates that allow to extract the positioning of each device in a common global coordinate system. Traditionally, this procedure implies solving equations using standard mathematical tools, but with the evolution of the Machine Learning in recent years there is also a new trend that combines traditional mathematical methods with compensation networks (to correct errors and improve accuracy [15]).

Some of the laser 3D triangulation solutions assume that the cameras have already been calibrated, i.e., that the camera intrinsic parameters are known before doing the calibration of the whole triangulation system. The camera calibration is a standard and well known procedure, except for those cameras with Scheimpflug. Thus, with these adapters we are able to focus the laser projection in a wider range, which is a desirable property for a 3D triangulation system. This improvement is specially noticeable when dealing with objects of a considerable size, in which the laser beam hits the surface of the object at different distances (depths) from the camera. Despite its benefits, it also increases complexity, specially when doing the calibration of the camera (additional tilt parameters need to be estimated [2,4,5,19]).

Compared to the existing solutions, this work describes a 3D triangulation system that uses cameras with Scheimpflug adapters and proposes a calibration procedure that requires a 3D calibration pattern that has been carefully designed for this application. Thanks to the use of this specific 3D calibration pattern, the calibration process is quick and simple, without requiring much intervention.

3. Methodology of the Calibration Method

Classical methods consider a laser triangulation system composed by the set of cameras $\mathcal{C} = \{c_1, c_2, \dots, c_n\}$ and the set of lasers $\mathcal{L} = \{l_1, l_2, \dots, l_m\}$, each of them defining a local coordinate system. Given a point $P_j \in \mathbb{R}^3$ that belongs to the plane defined by the laser l_j , its position $P_i \in \mathbb{R}^3$ in the coordinate system defined by camera c_i can be obtained as:

$$P_i = T_{ij}(P_j) \quad (1)$$

where $T_{ij} \in SE(3)$ is the rigid transform relating the laser l_j with the camera c_i .

This point can be expressed in a common reference frame by means of another rigid transform $T_{wi} \in SE(3)$ that relates the camera c_i to the world coordinate system:

$$P_w = T_{wi}(P_i) = T_{wi}T_{ij}(P_j). \quad (2)$$

The main objective of the calibration is to find all the transforms $\hat{T} \subset \{T_{ij}, T_{wi}\}$ where $T_{ij} \in \hat{T}$ if the laser l_j is visible by the camera c_i . In order to calibrate the laser frames respect to the observing cameras, most methods use planar checkboards [12] or even 3D calibration boards [20], placed such that so that the laser lines cut across squares of the checkboard. The drawbacks to this type of calibrations is that the intrinsic parameters of the cameras have to be estimated with high accuracy, especially in the case of Scheimpflug cameras.

Our method assumes that the images are undistorted (either computing Scheimpflug distortion maps as calculated in the next subsections or that the distortion can be considered negligible). Instead of computing the previous matrices, we use a calibration object that can be easily detected in the images of the cameras, the method being similar to [21]. Given that all the points P_j reflected by a laser are contained in the same plane, whose frame is defined having the Z coordinate equal to zero, the calibration can be computed in \mathbb{P}^2 as the homography relating points in the laser plane to their projections in the image plane, that works both for regular and Scheimpflug cameras.

$$p_i = H_{ij}p_j \quad (3)$$

where $p_j \in \mathbb{P}^2$ is the point P_j expressed in the local reference system of the laser plane l_j , and $p_i \in \mathbb{P}^2$ is the corresponding point in the camera plane c_i in pixels. Note that the intrinsic parameters of the camera are implicitly included in H_{ij} if p_i is expressed in pixel coordinates, which makes the calibration simpler and less error-prone.

In the same way, if a laser is visible in two or more cameras they can also be related by another homography, having as a result the relationship between all the reference systems. In case that there are several lasers, the transformation between the local laser frames can be derived by using calibration patterns that have a shape that favours the estimation of this transformation (see Section 4).

These homographies are recovered using the Direct Linear Transform (DLT) algorithm [22] and the corresponding transforms in \hat{T} are finally extracted using the decomposition described in [23].

3.1. Scheimpflug Model

In this section, different methods to identify and correct the camera Scheimpflug distortions are shown, as well as identification of the cases in which image distortion correction is irrelevant.

3.1.1. Projection Model

As shown in Equation (3), the relationship between the laser and the image planes, even in the case of different measurement units (e.g., millimeters in the laser plane and pixel in the image plane) is a homography in the absence of the image distortion correction, which also works for the case of Scheimpflug cameras. The camera projection in the case of tilted cameras is given by the equation:

$$s(x_t, y_t, 1)^T = KH_p(x_{cam}, y_{cam}, 1)^T \quad (4)$$

where $(x_t, y_t, 1)^T$ corresponds to the homogeneous coordinates of a point in the tilted camera frame in pixels, $(x_{cam}, y_{cam}, 1)^T$ corresponds to the homogeneous coordinates of the observed laser point in the camera frame in normalized image coordinates (projection of the observed point into a camera with focal distance equal to 1), K corresponds to the intrinsic pinhole camera projection with principal distance c equal to the distance between the optical center and the camera sensor. H_p corresponds to the transformation of points

between the untilted and the tilted image planes, whose origin is at a distance $d = m_p * c$ from the projection center and m_p corresponds to the pupil magnification factor.

Note that in the case that the plane is no tilted, H_p is a unit matrix, so that the above equation corresponds to the standard pinhole camera projection. The transformation H_p of points in the camera frame to the Scheimpflug plane is given by the following homography [5]:

$$H_p = \begin{bmatrix} r_{11}r_{33} - r_{13}r_{31} & r_{21}r_{33} - r_{23}r_{31} & 0 \\ r_{12}r_{33} - r_{13}r_{32} & r_{22}r_{33} - r_{23}r_{32} & 0 \\ r_{13}/d & r_{23}/d & r_{33} \end{bmatrix} \quad (5)$$

where r_{ij} is the i, j element of the matrix R_t that defines the rotation part of the transformation between the tilted and untilted frames.

The model described by Equation (3) remains valid since it can be expressed as a composition of homographies:

$$p_i = KH_p C_{Nij} p_j = H_{ij} p_j \quad (6)$$

where C_{Nij} is the normalized camera matrix with focal unit length [22], i.e., $C_{Nij} = (\mathbb{I} \mid 0) \begin{pmatrix} R_{ij} & T_{ij} \\ 0 & 1 \end{pmatrix} = (R_{ij} \mid T_{ij})$, and R_{ij} , T_{ij} are the rotation and translation part of the pose of the laser frame j relative to the camera frame i .

3.1.2. Distortion Model

The radial distortion model of Brown [24] computes radial and decentering distortions in the normalized plane (plane at a unit focal length). In case of untilted cameras, radial distortions are accurate enough to model it. For the Scheimpflug model presented here, the transformation of pixels from the tilted plane at distance d to the normalized untilted unit plane is made with the transformation:

$$s(x_u, y_u, 1)^T = H_p^{-1} K^{-1} (x_t, y_t, 1)^T \quad (7)$$

with the matrix H_p being the unit matrix, as the plane at distance d is untilted, and $(x_u, y_u, 1)$ corresponds to the camera projection in the untilted plane in normalized coordinates. Thus, the radial distortion calculation is made the same way as in a regular pin-hole camera. In order to calculate the distortion map in the tilted plane (in pixels), first the coordinates of the distorted point $(x_d, y_d)^T$ are calculated:

$$s \begin{bmatrix} x_d \\ y_d \end{bmatrix} = \begin{bmatrix} x_u(1 + K_1 r^2 + K_2 r^4 + \dots) \\ y_u(1 + K_1 r^2 + K_2 r^4 + \dots) \end{bmatrix}; r^2 = x_u^2 + y_u^2 \quad (8)$$

Then, the distorted point in the tilted image plane in pixels results in:

$$s(x_{dt}, y_{dt}, 1)^T = KH_p(x_d, y_d, 1)^T \quad (9)$$

As an example, one of our cameras with 50 mm focal length is tilted 25° with magnification ratio of 1. The untilted and tilted distortion map are shown in Figure 2. The Matlab code for the calculation for these maps has been included in Appendix ??.

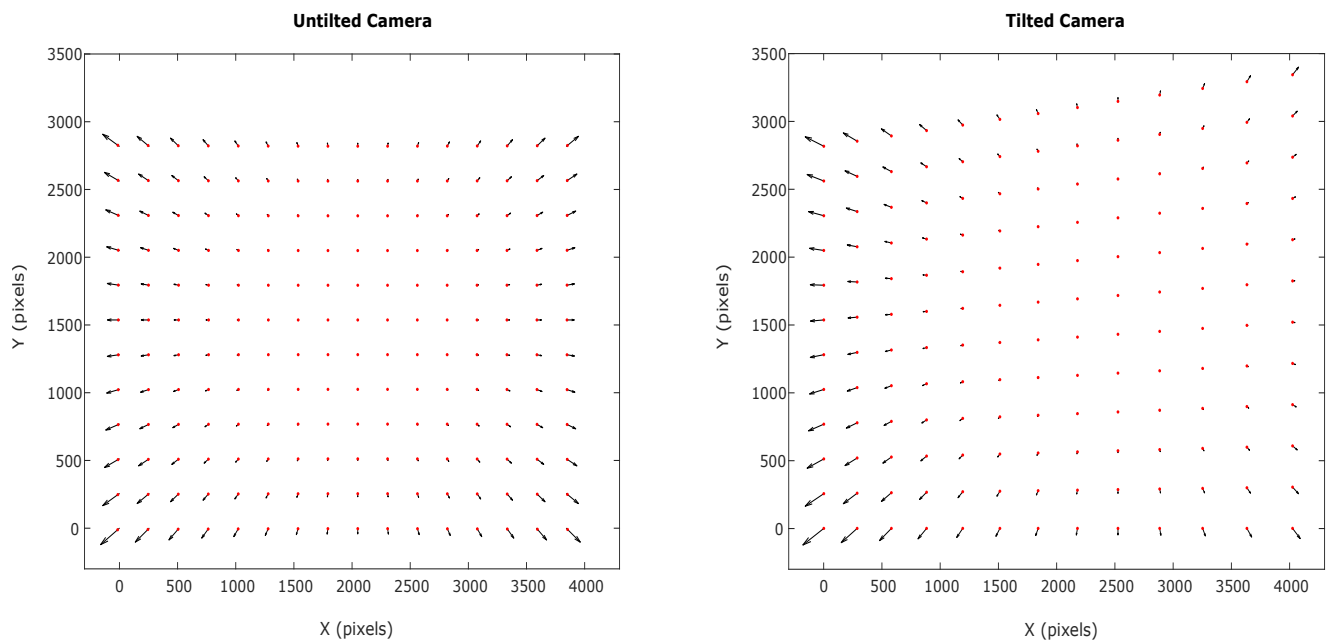


Figure 2. Distortion map errors amplified 10 times for an untilted and tilted camera by 25° and magnification ratio $m_p = 1$.

3.1.3. Distortion Model Calculation

There are different methods to calculate the Scheimpflug distortion:

- Calculation of the distortion radial coefficients in case that a similar untilted camera is available. In this case the lens can be fitted into this camera and a standard camera calibration can identify the radial parameters. With this data, and the knowledge of the tilted Scheimpflug angle as well as the magnification factor m_p , the Scheimpflug distortion map can be calculated as in the previous section.
- Other alternatives consist of performing a Scheimpflug calibration as in [5], which has already been implemented in the Halcon-Mvtec software [25]. The identified (radial distortions and H_p transformation matrix) allows one calculation of the Scheimpflug distortion map.
- In cases where the tilted angle is small (Scheimpflug angles smaller than 6°), [4] showed that the decentering distortion parameters (also called tangential parameters) compensate the Scheimpflug angle effects. Thus, a pin-hole standard calibration with radial and decentering parameters can be used in order to calculate the Scheimpflug distortion map.

3.1.4. Usage of the Scheimpflug Distortion

Many lenses with large focal lengths present almost no image distortion. In addition to this favorable scenario, in order to calculate the laser-camera homography without Scheimpflug distortion compensation, but with a given accuracy, one of the following procedures should be followed to ensure that the right conditions exist in order to discard distortion compensations:

- An initial approximated Scheimpflug distortion map can be estimated employing one of the previous methods. With the initial estimation of the laser-camera homography, the laser projections should be calculated for the pixels on the border of the image (the ones having largest distortions) with and without distortion. If the error obtained in the laser plane is smaller than the precision needed in the reconstruction, then the calculation of the accurate Scheimpflug map compensations can be avoided.
- Laser lines produced by the laser or other lines in the scene should be observed in the camera image. If the line fitting errors of the projected lines in pixels is similar to the

errors in the estimation of the laser pick detector, Scheimpflug distortion maps can be avoided.

In the proposed solution we have discarded the Scheimpflug distortion compensation because we have tested that we get the desired accuracy without applying it (see Section 6.1).

4. Implementation and Calibration for the Presented Setup

Figure 1 represents our laser 3D triangulation system composed by two lasers and three cameras, plus a motorized rotation stage (model 8MRB240-152-59—Large Motorized Rotation Stage of Standa with an accuracy of 15') that includes claws to fix the object. This setup has been specifically designed to capture revolution parts such as the one shown in Figure 3.

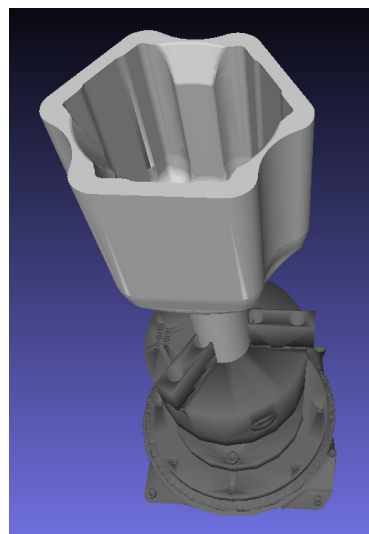


Figure 3. Example of revolution part that is handled with the proposed laser 3D triangulation system. The part (colored in light gray) is tied by the claws of the rotation stage (colored in dark gray).

Two cameras and one laser have been placed at the top to obtain the reconstruction of the interior of the object (the second camera is intended to avoid occlusions). Similarly, the remaining camera and laser have been placed at the bottom to reconstruct the external surface of the object. Given that, the proposed system has 3 camera-laser pairs.

Both lasers have been oriented in such a way that their projected lines are aligned with the rotation axis of the rotation stage, i.e., both laser projections and the rotation axis are coplanar. Furthermore, to ensure a focused image in the maximum area of the laser plane, each camera includes a Scheimpflug adapter to make its image plane and the corresponding laser plane as perpendicular as possible (Figure 4).

4.1. Modeling

Following the methodology depicted in Section 3, this setup is composed by three cameras c_1, c_2, c_3 and two lasers. However, as both lasers are coplanar, the setup can be simplified as a single laser configuration with l_1 in a first step, although an alignment refinement is presented in Section 4.4.5.

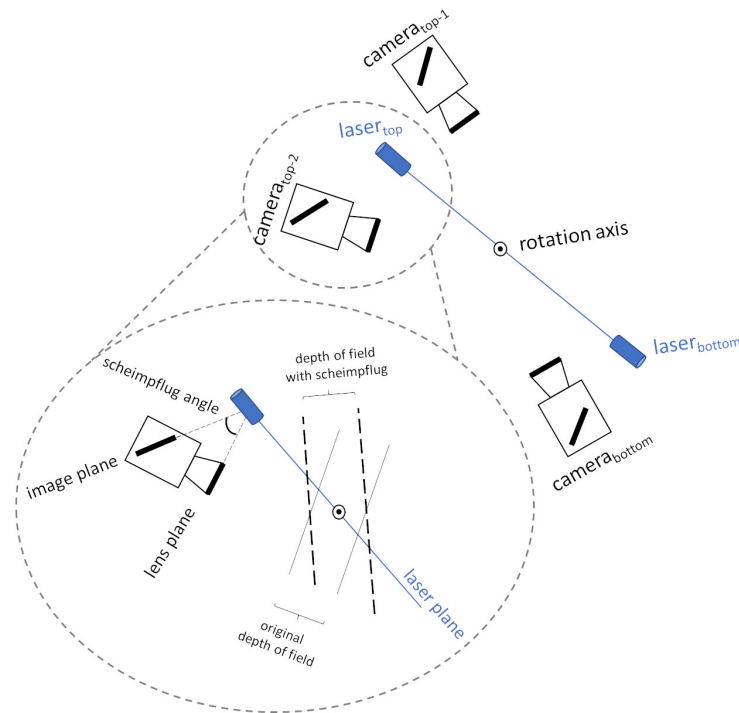


Figure 4. Arrangement of cameras and lasers in the proposed laser 3D triangulation system. The Scheimpflug principle is detailed for one of the camera-laser pairs.

With this assumption, the system is completely described by Equation (6) as:

$$\begin{aligned} p_{c1} &= H_1 p_{l1} \\ p_{c2} &= H_2 p_{l1} \\ p_{c3} &= H_3 p_{l1} \end{aligned} \quad (10)$$

where H_1, H_2, H_3 are the homographies relating the laser plane with the three cameras.

To get a 3D reconstruction of an object, it is placed on the rotation stage and a complete rotation (360 degrees) is performed automatically (controlled by the motorized rotation stage). It is noteworthy that the piece is fixed with claws to center it in the stage, as well as to avoid unexpected displacements during the rotational motion.

For each rotation step (1 degree in our case), each camera-laser pair takes a capture, so that each camera-laser pair provides 360 profiles in total. Note that this movement is analytically equivalent to a setup with 360 laser planes, where each plane $l_j \mid 1 \leq j \leq 360$ is related to a world plane with a rotation R_j around the axis of the stage.

Without loss of generality, if we assume that the axis of the stage is at the origin of the reference system, the reconstruction of a point p_w captured by the camera i at the step j can be expressed as follows:

$$p_w = R_j H_i^{-1} p_i \quad (11)$$

4.2. Calibration Pattern

The calibration pattern that has been used is the one shown in Figure 5. It has a conical shape and it is formed by five coaxial cylinders of different diameters to which a cut has been applied to get two planar faces (inner and outer) with the same orientation. Its design has been inspired by the one used in [8], but a planar face has been added to be able to solve the degree of freedom associated with the turn about the axis of rotation (see below).

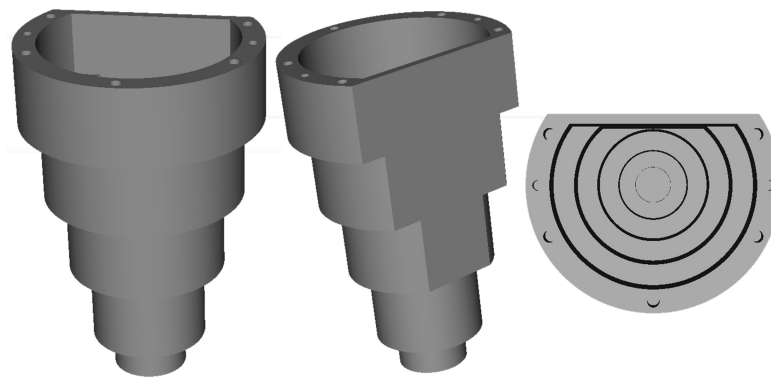


Figure 5. Calibration pattern. Front (**left**), back (**middle**) and top (**right**) views of the 3D model.

This design has been chosen for the following reasons:

- When a laser beam hits the pattern in the part of the cylinders, the beam describes a staircase shape and its intersection points can be detected and act as control points to get the calibration homographies (see Sections 4.4.1 and 4.4.2). This staircase shape appears on both sides of the pattern, on the outer face as well as on the inner face. The outer face is visible by the camera at the bottom while the inner face is visible by the two cameras at the top.
- After having an initial solution of the calibration, a 3D reconstruction of the calibration pattern can be performed. In this 3D reconstruction, the two planar faces can be detected automatically and used to refine the alignment between the top and bottom camera-laser pairs along the axis of revolution (see Section 4.4.5).

4.3. Laser Capture

The accuracy of a 3D reconstruction using laser linear illumination is significantly determined by the accuracy of the line segmentation in the image. Since the pattern of image intensity in the normal direction to the line has a Gaussian profile, finding the center of the line in the image corresponds to detect the point of maximum intensity in the normal direction, i.e., the laser peak. This peak can be detected by different algorithms using the intensity distribution along a column of the sensor image, e.g., finding the position of maximum intensity, finding thresholding points or finding the center of gravity [26–28]. In the proposed sensor, a Savitzky-Golay [29] finite impulse response (FIR) differential filter is applied to the image intensity profile of the laser line computing the zero-crossings with sub-pixel accuracy [30–32].

4.4. Method

In order to calibrate the system, the calibration pattern is placed on the rotation stage and rotated 360 degrees while each camera-laser pair takes a capture per degree. After capturing this set of profiles, the steps shown in Figure 6 are executed for camera-laser pair to automatically extract the corresponding homographies.

The shape of the calibration pattern (Section 4.2) generates images that have a staircase shape as shown in Figure 7. For each image generated by each camera-laser pair a line detection algorithm is applied to extract predominant lines (Section 4.4.1). The intersection points of these lines are matched to their reference (nominal) counterparts that are specified in a global coordinate system (Section 4.4.2). Using these correspondences, for each camera-laser pair the homography that transforms points from the image plane to the laser plane can be estimated (Section 4.4.3). Additionally, the 3D reconstruction for each camera-laser pair is obtained by applying the corresponding rotation angle (given by the encoder of the rotation stage) using Equation (11) (Section 4.4.4). Therefore, each partial 3D reconstruction is accumulated to build the final 3D reconstruction. In the last refinement step these partial 3D reconstructions are aligned with each other using the planar reference faces of the calibration pattern. This faces are automatically detected so that the final homographies

make them share the same normal (Section 4.4.5). An overview of the whole pipeline is shown in Figure 6.

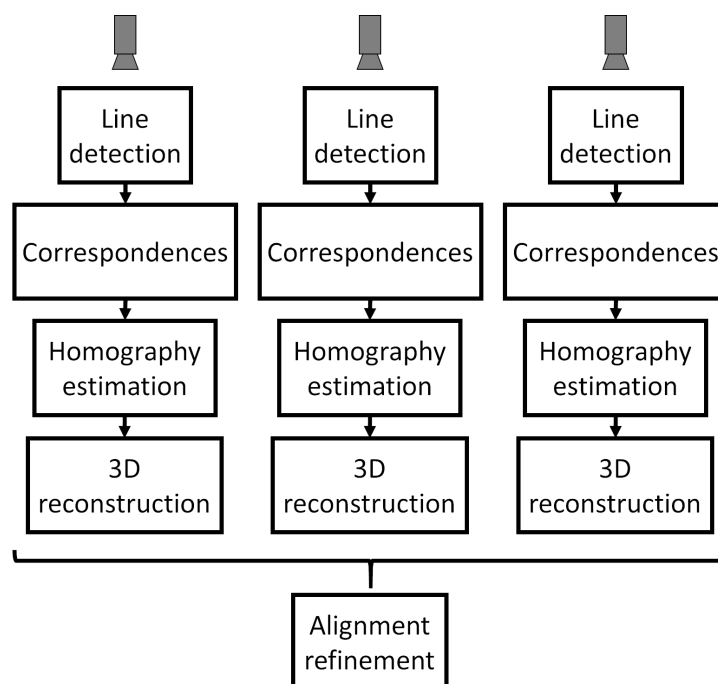


Figure 6. Calibration pipeline.

4.4.1. Line Detection

Figure 7 shows an example of a captured laser profile of the calibration pattern at each rotation step. The raw captured profile contains some noise (highlighted in red in the top of Figure 7), especially at the extremes, since the laser beam can hit other objects apart from the calibration pattern. As this noise usually appears at the extremes and is separated from the main part, to remove it a point clustering is done based on the euclidean distance, and the biggest cluster is only retained.



Figure 7. Example of captured laser profile for the calibration pattern. Raw data with noise highlighted in red (top), and the result after removing noise and detect lines (bottom).

With the cleaned profile, N predominant lines are searched using RANSAC [33], which is a hypothesis-verification technique. We execute RANSAC N times or until no points are available, and for each execution the predominant line is obtained and its inlier points (those points whose distance to the line is less than a predefined threshold) are

removed from the profile for the next execution. N represents the maximum number of lines to be detected for each profile and is a predefined parameter that depends on the shape of calibration pattern and its visibility from the camera. Taking into account visibility limitations, in our configuration, we have set N as 11 for the bottom camera-laser pair and 9 for the top camera-laser pairs (see Figure 8 to substantiate how these numbers are defined). It should be emphasized that less than N lines will be detected in the planar side of the calibration pattern because the stop criterion will be given by the absence of more available points to form line hypothesis.

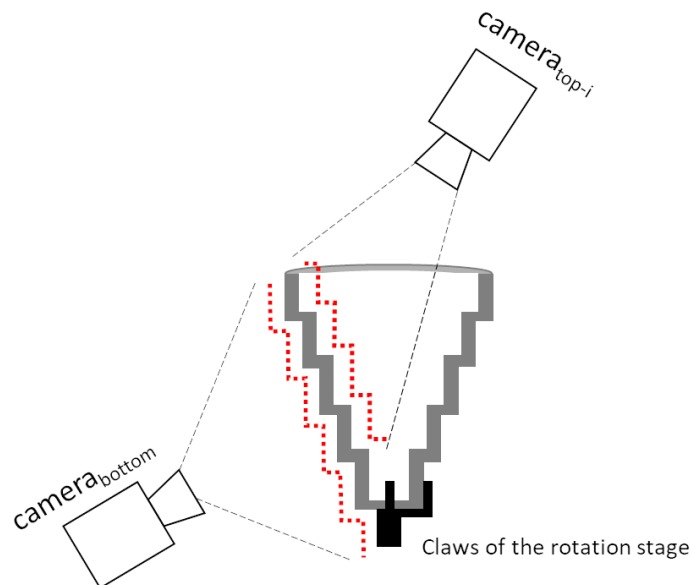


Figure 8. Maximum number of lines of the calibration pattern that are visible by each camera-laser pair in each profile (highlighted in red). The body of the claws of the rotation stage increases the number of lines for the bottom camera-laser pair. The bottom part of the inner side of the calibration pattern is not visible by the top cameras.

To avoid undesired line detections, such as the line that crosses the entire profile and which would have a large number of positive votes in RANSAC, we have included the following heuristics to the original RANSAC algorithm.

- *Length restrictions:* Instead of considering 2 random points to form a line hypothesis, we only consider those pairs of points whose distance is between a predefined range. Thus, we discard hypotheses that are formed by too close points (which offers unstable estimation of the line direction) as well as those formed by too distant points (to reduce the appearance of hypotheses with considerable length). When assigning positive votes to a line hypothesis, we also discard those points that are too distant from the 2 original points that form the line hypothesis.
- *Direction restrictions:* Given the staircase shape of our profile, the new line to be detected in the current RANSAC execution has to be almost 90 degrees from the line detected in the previous execution, i.e., we use the normal of the previous detected line as an initial estimation of the direction for the current line. We estimate the normal for each point using the k closest points at the beginning, so that line hypothesis are only formed by point pairs that have similar normal. Similarly, when assigning positive votes to a line hypothesis, we discard those points whose normal is not similar to the normal of the line hypothesis.

Additionally, the line estimated after each RANSAC execution need to pass a *fitting quality* control to be considered as valid. Within the inlier point set of the line, the two most extreme points are taken to form the longest segment, and its oriented bounding box is

calculated and used to retain those points from the whole profile that are inside it, i.e., to get a potential inlier point set. Thus, the ratio $\text{number_of_inlier_points}/\text{number_of_potential_inlier_points}$ represents the fitting quality and must be higher than a predefined value to register the current line as a good one. This test is mainly focused on discarding lines with a spatially non-uniform and dispersed set of inliers (generally produced by several groups of independent points), and which is usually associated with a bad estimate.

To speed up all the calculations (including the initial point clustering), we work on a subsampled profile (we apply a non-maximum suppression), and once we detect the lines, we refine them using the original profile points to improve the accuracy of line estimation.

4.4.2. Correspondences

After the previous step, we have several line estimations for each profile, and each line can be represented by the longest segment formed by the the two most extreme points of the inlier set. Thus, for each profile we sort its segments using the coordinates of these points (those closest to the origin first), and then, compute the intersections between consecutive segments. To avoid bad configurations, we only retain those intersection points that are close to one of the extreme points of both segments. Moreover, from the whole set of 360 profiles, we initially select those for which the number of intersection points is equal to the number of nominal intersections.

These selected profiles provide an unambiguous correspondence between detected and nominal intersection points, which are the control points used to calculate the homography between the camera and the laser plane. The nominal intersection points have been obtained by measuring the calibration pattern using a Coordinate Measuring Machine (CMM). In our case, we have used the Mitutoyo Crysta-Apex S 9106 CMM model to do this measurement, which offers a high accuracy (~ 0.002 mm). As the cylinders of the pattern are symmetrical about the central axis of the pattern (which coincides with the axis of rotation of the system), the CMM has measured the intersection points along a plane that cuts the pattern and passes through the central axis, which is coincident with the laser plane (see Figure 9 for a graphical representation).

Many times the set of selected profiles are concentrated in one small area of the calibration pattern, so the posterior results can be overfit to this area. Furthermore, since the calibration pattern has manufacturing tolerances, the results may vary depending on the area used. To avoid this problem, we make a second pass to try to include some intersection points from unselected profiles and get correspondences that are distributed in a more uniform way throughout the entire surface of the calibration pattern. Using the intersection points of the selected profiles, we compute the median for each of the $N - 1$ intersection points, and then, for each unselected profile we check if its intersection points are close to these median values. In case of finding at least 2 valid intersection points, the unselected profile is considered to be partially good and its validated intersection points are included to the set of correspondences.

4.4.3. Homography Estimation

The previous step provides a set of correspondences between the intersection points detected in the image and the reference intersection points that are in global coordinates and rest on the laser plane. More precisely, for each of the $N - 1$ different reference intersection points we have several correspondences. Under our experience, instead of using a RANSAC style algorithm with all correspondence samples, we have had more stable results making the median of the detected image correspondences for each of the $N - 1$ different reference points, and then, computing the homography (in a least squares sense) using the resultant $N - 1$ correspondences (Figure 9). The median values are used to compensate possible manufacturing tolerances (eccentricities, etc.) of the calibration pattern.

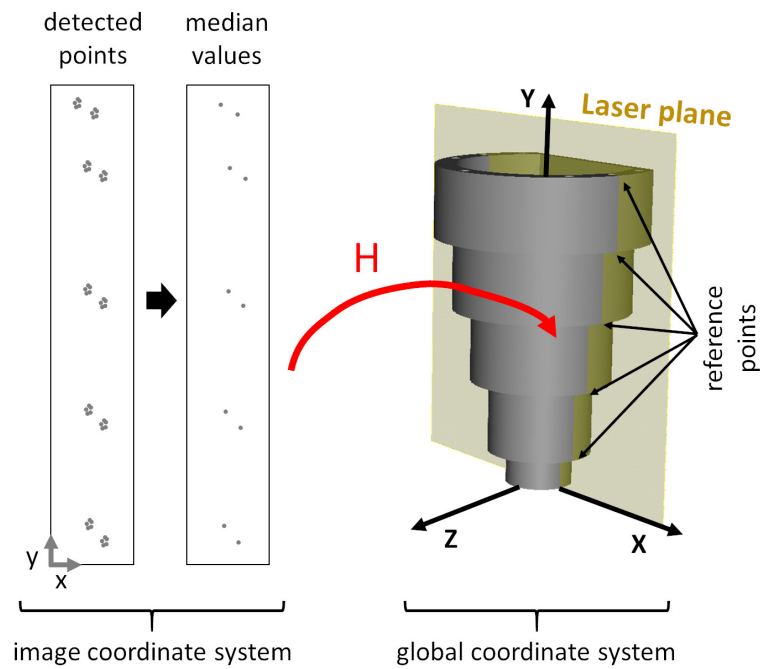


Figure 9. Conceptual representation of the homography estimation. Intersection points of the whole profile set are simplified using median values and used as correspondences of the reference intersection points. The computed homography transforms points from the image plane (in image coordinates) to the laser plane (in global coordinates).

The homography that is estimated transforms points from the image plane to the laser plane (or viceversa if its inverse is used, since a homography is a 3×3 invertible matrix). For clarification purposes, we assume that the laser plane coincides with the XY plane of the global coordinate system, i.e., $Z = 0$. Given that, and following the notation of Equation (11), the homography transformation chain can be expressed as

$$\begin{aligned} p_w &= (X, Y, W)^T = H_i^{-1}(x, y, 1)^T = H_i^{-1}(p_i, 1)^T \\ P_w &= (X/W, Y/W, 0)^T \end{aligned} \quad (12)$$

where p_w are the XY homogeneous coordinates of the laser points, P_w are the 3D coordinates of the laser point in the global coordinate system.

4.4.4. 3D Reconstruction

According to Equation (12) points of each of the 360 captured profiles can be transformed to the global coordinate system. However, this transformation moves all points to the laser plane, i.e., all the profiles are accumulated in the same plane. To reconstruct properly each profile we have to apply the corresponding rotation to each profile. When a profile is captured, we know at which rotation step has been captured, since this information is provided by the encoder of the rotation stage. Thus, the points of the profile k , which has been captured at the rotation step j (which equals to j degrees, as 360 profiles are captured in 360 degrees, i.e., rotation step is 1 degree), must be transformed as follows

$$(X', Y', Z')^T = \begin{bmatrix} \cos(j) & 0 & \sin(j) \\ 0 & 1 & 0 \\ -\sin(j) & 0 & \cos(j) \end{bmatrix} P_w^k = R_j P_w^k \quad (13)$$

where P_w^k represents the points of the profile k after applying Equation (12), R_j is a rotation matrix of j degrees about the axis of rotation of the system (which coincides with the Y axis

of the global system), and $(X', Y', Z')^T$ are the resultant global coordinates of the point and which are used to build the 3D reconstruction of the scanned object (the calibration pattern).

4.4.5. Alignment Refinement

All the processing steps described in the previous Sections 4.4.1–4.4.4 are executed by each camera-laser pair independently. As a result, we obtain several partial 3D reconstructions of the calibration pattern, one for each camera-laser pair. These partial 3D reconstructions are correctly aligned in translation and in the rotations of the X and Z axes, but the alignment in the rotation of the Y axis (the main axis of the rotation stage) is not guaranteed, since each camera-laser pair has a different origin of the rotation (different starting point) through the Y axis when applying Equation (13). If this rotation ambiguity is not solved, the partial reconstructions are not well aligned on the Y axis, and therefore, if these partial reconstructions were joined, a bad global reconstruction would be seen (there would be an offset between them). This misalignment effect would be appreciated especially in those objects that are not completely symmetrical along the Y axis.

To ensure a correct alignment in the rotation of the Y axis we use the planar faces of the calibration pattern (Figure 5). In each partial 3D reconstruction we can search for the predominant plane and use its normal to align them all together, i.e., find a rotation delta in Y axis (Δ_i) for each camera-laser pair (i) to force that all the plane normals match and point in the same direction. The final global coordinates $(X'', Y'', Z'')^T$ that are used to build the 3D reconstruction of the scanned object (the calibration pattern) are obtained after applying this rotation delta to the Equation (13).

$$(X'', Y'', Z'')^T = \begin{bmatrix} \cos(\Delta_i) & 0 & \sin(\Delta_i) \\ 0 & 1 & 0 \\ -\sin(\Delta_i) & 0 & \cos(\Delta_i) \end{bmatrix} (X', Y', Z')^T \quad (14)$$

Given that, it is noteworthy that the calibration of each camera-laser pair (i) will be given by its own homography (H_i) and rotation delta (Δ_i) as shown in Equations (12)–(14). Likewise, the final 3D reconstruction will be given by merging all partial 3D reconstructions of all camera-laser pairs.

The extraction of the predominant plane for each partial 3D reconstruction can be speed up using the grouping of profiles done in Section 4.4.2. The profiles that were discarded as correspondences for not having multiple intersection points between lines, are precisely those that will belong to the part of the calibration pattern where the plane is located. Therefore, we can identify these profiles and only use their 3D reconstruction to find the predominant plane.

5. Reconstruction of Revolving Objects

Previous section describes the calibration process of the proposed 3D laser triangulation system. Thus, once the system has been calibrated, it can be used to build the 3D reconstruction of revolving objects, such as the one shown in Figure 3.

The procedure to scan and reconstruct an object is straightforward. The user has to place the desired object in the rotation stage and ties it. Then, the user pushes a button and the system automatically applies a complete rotation (360 degrees) while capturing profiles with the different camera-laser pairs. Afterwards, the system uses the calibration data (H_k and Δ_k) of each camera-laser pair (k) to apply Equations (12)–(14) to the corresponding profiles and to obtain the 3D reconstruction of the object.

6. Experiments and Results

6.1. Scheimpflug Distortion

In our experiment an approximated Scheimpflug distortion map for the used cameras (C5-4090-GigE cameras from Automation Technology GmbH and Zeiss Planar T* 50 mm lenses from Nikon) and the estimated homography were calculated resulting in maximum errors of 2 microns. These errors comes from the fact that a similar camera but without

Scheimplug angle, i.e., perpendicular camera, has been calibrated with the same lens used in the Scheimplug camera. A very precise dot calibration pattern with precision of about 2 microns has been used to calibrate the perpendicular camera, noticing practically no radial distortion, with a re-projection error that comes from the errors of the calibration plate. The Scheimplug distortion map, calculated with the matlab code of Appendix ??, shows distortions of a similar magnitude that the distortions of untilted camera.

Real calibration of the laser-camera homography was made by fitting projecting the laser over a calibrated revolution cone, assuming that the distortion map can be avoided. The errors obtained in the homography estimation were smaller than 7 microns. The advantage of this method resides on the fact that difficult and error-prone Scheimplug calibration procedures can be avoided, which can at the end be more costly and less precise than this simpler method.

6.2. Calibration Repeatability and Accuracy

In order to demonstrate the repeatability of the proposed calibration method, we have performed the calibration 10 times. Moreover, to introduce variability in the data, the pattern has been placed in a different initial position for each calibration, providing a different set of profiles as input. At each calibration execution we have calculated the calibration data and the 3D reconstruction of two different objects: (1) the calibration pattern, and (2) an object that is similar in shape to the calibration pattern, but with a small change in the size (different height and different diameter lengths). The idea of introducing this second object is to see results without the possible effects of overfitting due to the usage of the same object for both calibration and test.

We have used these 3D reconstructions to perform some measurements and provide a comparison between them. More precisely, we have measured the diameter of several cylinders. Furthermore, the height of a plane at different locations has been estimated for the calibration pattern as well (see Figure 10 for a graphical representation of measured cylinders and planes). In all cases we have used points of the inner and outer part of the 3D model to estimate cylinders and planes of the outer and inner parts respectively.

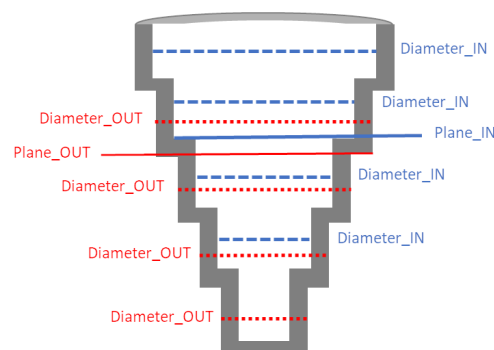


Figure 10. Measured cylinders and planes for each calibration execution during the repeatability experiments (see text for details). Inner cylinders and plane are highlighted in blue, while outer cylinders and plane are in red color.

Tables 1 and 2 show the error (expressed in millimeters) of these measurements respect to the nominal values, which have been obtained using a CMM (Mitutoyo Crysta-Apex S 9106, which offers a high accuracy, ~ 0.002 mm).

To provide a robust central tendency, truncated mean of the results of the 10 calibrations has been calculated, i.e., extreme values (best and worst) have been discarded during the mean computation. Moreover, the standard deviation of the error of these 10 calibrations is shown for each measurement. These standard deviation values are low, which indicates that the calibration algorithm offers a good repeatability.

Table 1. Mean and standard deviation error (in mm) of some primitives (cylinders and planes) of the calibration pattern respect to nominal values using different calibrations.

Calibration Pattern		Error	
Measurement	Nominal	Mean	Stdev
Diameter_OUT	44	0.064	0.009
Diameter_OUT	71	0.115	0.005
Diameter_OUT	97.01	0.017	0.005
Diameter_OUT	123	0.059	0.016
Diameter_IN	50.94	0.031	0.008
Diameter_IN	76.95	0.067	0.041
Diameter_IN	102.95	0.084	0.087
Diameter_IN	129	0.18	0.047
Plane_OUT	121.96	0.194	0.014
Plane_IN	132	0.061	0.012

Table 2. Mean and standard deviation error (in mm) of some primitives (cylinders) of an object, which is similar in shape to the calibration pattern, respect to nominal values using different calibrations.

Object with Similar Shape		Error	
Measurement	Nominal	Mean	Stdev
Diameter_OUT	72.044	0.126	0.011
Diameter_OUT	98.062	0.244	0.014
Diameter_OUT	124.075	0.268	0.031
Diameter_OUT	150.091	0.053	0.06
Diameter_IN	46.948	0.068	0.016
Diameter_IN	71.99	0.055	0.04
Diameter_IN	96.96	0.1	0.094
Diameter_IN	121.992	0.107	0.142

To obtain each measurement (related to cylinder or plane), points of the 3D reconstruction that are close to the corresponding nominal value have been sampled, and then, a specified fitting algorithm has been applied. Thus, it is noteworthy that the errors that are shown in Tables 1 and 2 accumulate the error of: (i) the laser (sensor accuracy), (ii) the centering of the object on the axis of rotation, (iii) the proposed calibration method and (iv) the fitting algorithms. In fact, the effect of the error in the centering of the object, which mechanically depends on the claws that tie the object at its bottom, is noticeable by observing the errors, since in the upper and outer areas of the object there is more error than in the lower and bottom areas respectively (a slight pitching effect).

As an supplementary measure of accuracy, we have calculated the distance between the 3D reconstructed model and its corresponding original 3D model for the object with similar shape. We have compared each of the previous 10 3D reconstructions of this object against its original 3D model. The mean and standard deviation of the errors of these 10 comparisons has turned out to be 0.151 mm and 0.015 mm respectively. As stated before, these errors values accumulate the error of several sources (the laser, the centering of the object, the quality of the calibration and the fitting algorithm).

Taking into account all the experiments presented above, we can point out that the system offers an accuracy of tenths of a millimeter with a variability of hundredths of a millimeter.

Real Case

As an additional evidence of the validation of the proposed system, we have made experiments with an industrial part (Figure 3) that is being used in a real factory. We have used it as a reference to validate the accuracy of the calibration. Being a result of an industrial manufacturing process, this part undergoes a series of measurements (designed and defined by expert metrologists) at some key points to ensure that the tolerances are

met. These measurements are usually performed using a CMM, which offers high precision results. Thus, we have considered several of these measurements and we have calculated them using both the CMM and a metrology software which we have provided as input the scanned and reconstructed 3d model of the part using the laser 3d triangulation system described above (Section 4).

Comparing the results of both alternatives, we observed that the errors are less than 0.1 mm, which indeed, is accurate enough to be used for this real application. The details of the repeatability and reproducibility (R&R) experiments that led to this value can be found in [8].

6.3. Discussion

The proposed calibration methodology requires the use of a calibration pattern, whose main design features have been defined in Section 4.2. Getting a similar pattern can be a laborious task, but it only needs to be done once. In return, the proposed calibration process itself is fast (it takes less than 1 minute), simple, and requires minimal user intervention. Summing up, the user places the calibration pattern on the rotation stage and ties it, and then, the system automatically applies a complete rotation (360 degrees) while capturing profiles with the different camera-laser pairs. Afterwards, the system process automatically each profile to extract the lines, the correspondences against the reference points and estimate the calibration data. It should be noted that the automatic processing of each profile has proven robust to the noise that can appear during the capture of profiles.

The experiments have been carried out using two different surface materials. The calibration object is made of machined steel finished with a dark coating which has a certain specular component, while the validation object is made of plastic resin that has a greater diffuse component. In both cases we have observed an adequate behavior of the optical system, requiring only to adjust the exposure time of the cameras. Additionally it has also been tested with forged steel objects. It is noteworthy that very specular materials, such as glass or machined metals, are not suitable for the proposed system.

Considering the intended use we wanted to give to the proposed laser 3d triangulation system (emphasize simplicity and automaticity of use within some bounds of accuracy), we have discarded the use of the Scheimpflug distortion. The impact on accuracy (microns according to our experiments of Section 6.1) is not significant, and it simplifies greatly the calibration process, allowing us to offer an almost automatic solution.

Apart from being synchronized with a rotation stage, the proposed calibration method requires knowledge of the coordinates of the reference control points (Section 4.4.2) to perform automatically all the processing. Given that, our calibration method could be adapted to work with other calibration patterns just by providing the new coordinates of the reference control points. The requirement for these new calibration patterns is that they must generate a staircase shape in the profiles when the laser hits their surface (see Figure 7).

7. Conclusions

This paper describes a laser 3d triangulation system oriented to revolving pieces. It combines 3 cameras and 2 lasers to capture and reconstruct most of the surface of the objects that want to be scanned. Moreover, it includes Scheimpflug adapters to offer more flexibility in the setup of the cameras and lasers, i.e., to maximise the focus of the depth of field of the camera on the laser plane despite the orientation of both devices. Aside from the flexibility of the setup, another advantage of the proposed system is that it is easy to use, offering a high degree of automation of the entire process. The object to be reconstructed is automatically rotated using a rotation stage, and the 3 camera-laser pairs are synchronized in such a way that in each rotation step profiles are captured and processed automatically. The entire scan and reconstruct process takes less than 1 minute for each object, so it is another point in favor of the proposed 3d triangulation system as well.

Likewise, a fast and automatic calibration method is proposed to fine-tune the system. This calibration method uses a calibration pattern that has been designed to generate a staircase shape when the laser planes intersect with its surface. Indeed, this shape is what allows to perform an automatic processing of profiles in search of lines, their intersections, generate correspondences against the reference control points and to estimate the calibration data. For the calibration process, the calibration pattern is treated as an object in the sense that the user places the pattern on the rotation stage and it is rotated automatically to capture the profiles. Thus, the proposed calibration method is automatic and takes less than 1 minute. In order to achieve this high degree of automaticity and speed in calibration, the effect of Scheimpflug distortion has not been considered. Nonetheless, this has little impact on accuracy when using 50 mm lenses (microns, according to our experiments). Finally, in cases where the Scheimpflug distortion cannot be avoided, simple procedures for its calculation and the conditions where it can be avoided have been also presented.

The presented experiments validate the accuracy of the proposed laser 3d triangulation system when compared against the measurements made with a CMM. We have reported an accuracy of few tenths of a millimeter, which could be enough for several applications. In fact, as an evidence of its potential use, this system is already being used in a real factory to control the quality of the manufacturing process of an industrial part.

Author Contributions: Conceptualization, all authors; methodology, all authors; software, all authors; validation, all authors; formal analysis, all authors; investigation, all authors; resources, H.Á. and J.R.S.; data curation, H.Á. and J.R.S.; writing—original draft preparation, H.Á.; writing—review and editing, all authors; visualization, H.Á.; supervision, all authors; project administration, H.Á. and J.R.S.; funding acquisition, H.Á. and J.R.S. All authors have read and agreed to the published version of the manuscript.

Funding: This research received no external funding.

Acknowledgments: We thank our colleagues from GKN Driveline Legazpi S.A., who tested the algorithm in their manufacturing line and provided material for the experiments. We also thank our colleagues from Sariki Metrología S.A., whose knowledge on dimensional inspection has been very valuable during this research. Likewise, we express our gratitude to EKIDE Group for helping us with the manufacturing of the calibration objects.

Informed Consent Statement: Not applicable.

Conflicts of Interest: The authors declare no conflict of interest.

References

1. Huynh, D.Q.; Owens, R.A.; Hartmann, P.E. Calibrating a Structured Light Stripe System: A Novel Approach. *Int. J. Comput. Vis.* **1999**, *33*, 73–86. [\[CrossRef\]](#)
2. Legarda, A.; Izaguirre, A.; Arana-Arexolaleiba, N.; Iturrospe, A. A new method for Scheimpflug camera calibration. In Proceedings of the 10th International Workshop on Electronics, Control, Measurement and Signals, Liberec, Czech Republic, 1–3 June 2011; doi:10.1109/IWECMS.2011.5952376. [\[CrossRef\]](#)
3. So, E.; Michieletto, S.; Menegatti, E. Calibration of a dual-laser triangulation system for assembly line completeness inspection. In Proceedings of the 2012 IEEE International Symposium on Robotic and Sensors Environments Proceedings, Magdeburg, Germany, 16–18 November 2012; pp. 138–143. [\[CrossRef\]](#)
4. Legarda, A.; Izaguirre, A.; Arana-Arexolaleiba, N.; Iturrospe, A. Comparison and error analysis of the standard pin-hole and Scheimpflug camera calibration models. In Proceedings of the IEEE 11th International Workshop of Electronics, Control, Measurement, Signals and Their Application to Mechatronics, Toulouse, France, 24–26 June 2013; pp. 1–6. [\[CrossRef\]](#)
5. Steger, C. A Comprehensive and Versatile Camera Model for Cameras with Tilt Lenses. *Int. J. Comput. Vis.* **2016**, *123*, 121–159. [\[CrossRef\]](#)
6. Forest, J.; Salvi, J. A review of laser scanning three-dimensional digitisers. In Proceedings of the IEEE/RSJ International Conference on Intelligent Robots and Systems, Lausanne, Switzerland, 30 September–4 October 2002; Volume 1, pp. 73–78.
7. Fournel, T.; Lavest, J.M.; Coudert, S.; Collange, F. Self-Calibration of PIV Video-Cameras in Scheimpflug Condition. In *Particle Image Velocimetry: Recent Improvements*; Stanislas, M., Westerweel, J., Kompenhans, J., Eds.; Springer: Berlin/Heidelberg, Germany, 2004; pp. 391–405.

8. Mejia, D.; Sánchez, J.R.; Ruiz-Salguero, O.; Alonso, M.; Izaguirre, A.; Gil, E.; Palomar, J.; Posada, J. In-Line Dimensional Inspection of Warm-Die Forged Revolution Workpieces Using 3D Mesh Reconstruction. *Appl. Sci.* **2019**, *9*, 1069. [\[CrossRef\]](#)
9. Picon, A.; Bereciartua, A.; Gutierrez, J.; Perez, J. 3D High Precision Tube Bevel Measurement using laser based Rotating Scanner. In Proceedings of the IEEE Conference on Emerging Technologies and Factory Automation, Prague, Czech Republic, 20–22 September 2006; pp. 1190–1197. [\[CrossRef\]](#)
10. Lee, M.; Baek, S.; Park, S. 3D foot scanner based on 360 degree rotating-type laser triangulation sensor. In Proceedings of the 2017 56th Annual Conference of the Society of Instrument and Control Engineers of Japan (SICE), Kanazawa, Japan, 19–22 September 2017; pp. 1065–1070.
11. Idrobo-Pizo, G.A. Motta, J.; Sampaio, R. A Calibration Method for a Laser Triangulation Scanner Mounted on a Robot Arm for Surface Mapping. *Sensors* **2019**, *19*, 1783. [\[CrossRef\]](#) [\[PubMed\]](#)
12. So, E.; Munaro, M.; Michieletto, S.; Antonello, M.; Menegatti, E. *Real-Time 3D Model Reconstruction with a Dual-Laser Triangulation System for Assembly line Completeness Inspection*; Advances in Intelligent Systems and Computing, AISC; Springer: Berlin/Heidelberg, Germany, 2013; Volume 194, pp. 707–716. [\[CrossRef\]](#)
13. Peiravi, A.; Taabbodi, B. A Reliable 3D Laser Triangulation-based Scanner with a New Simple but Accurate Procedure for Finding Scanner Parameters. *Marsland Press J. Am. Sci.* **2010**, *6*, pp. 80–85.
14. Vilaça, J.L.; Fonseca, J.C.; Pinho, A.M. Calibration procedure for 3D measurement systems using two cameras and a laser line. *Opt. Laser Technol.* **2009**, *41*, 112–119. [\[CrossRef\]](#)
15. Yang, S.; Shi, X.; Zhang, G.; Lv, C. A Dual-Platform Laser Scanner for 3D Reconstruction of Dental Pieces. *Engineering* **2018**, *4*, 796–805. [\[CrossRef\]](#)
16. Li, D.; Zhang, H.; Song, Z.; Man, D.; Jones, M. An automatic laser scanning system for accurate 3D reconstruction of indoor scenes. In Proceedings of the IEEE International Conference on Information and Automation (ICIA), Macau, China, 18–20 July 2017; pp. 826–831. [\[CrossRef\]](#)
17. Song, L.; Sun, S.; Yang, Y.; Zhu, X.; Guo, Q.; Yang, H. A Multi-View Stereo Measurement System Based on a Laser Scanner for Fine Workpieces. *Sensors* **2019**, *19*, 381. [\[CrossRef\]](#) [\[PubMed\]](#)
18. Santolaria, J.; Guillomía, D.; Cajal, C.; Albajez, J.A.; Aguilar, J.J. Modelling and calibration technique of laser triangulation sensors for integration in robot arms and articulated arm coordinate measuring machines. *Sensors* **2009**, *9*, 7374–7396. [\[CrossRef\]](#) [\[PubMed\]](#)
19. Fasogbon, P.; Duvieubourg, L.; Lacaze, P.A.; Macaire, L. Intrinsic camera calibration equipped with Scheimpflug optical device. In *Twelfth International Conference on Quality Control by Artificial Vision 2015*; Meriaudeau, F., Aubreton, O., Eds.; International Society for Optics and Photonics: Bellingham, Washington, 2015; Volume 9534, pp. 313–319. [\[CrossRef\]](#)
20. Xu, G.; Hao, Z.; Li, X. An optimization solution of a laser plane in vision measurement with the distance object between global origin and calibration points. *Sci. Rep.* **2015**, *5*, 123. [\[CrossRef\]](#) [\[PubMed\]](#)
21. Collado, F. New Methods for Triangulation-Based Shape Acquisition Using Laser Scanners. Ph.D. Thesis, Departament d'Electrònica, Informàtica i Automàtica, Universitat de Girona, Girona, Spain, 2004. Available online: <http://www.tdx.cat/handle/10803/7730> (accessed on 23 January 2021).
22. Hartley, R.; Zisserman, A. *Multiple View Geometry in Computer Vision*, 2nd ed.; Cambridge University Press: New York, NY, USA, 2003.
23. Malis, E.; Vargas, M. *Deeper Understanding of the Homography Decomposition for Vision-Based Control*; 2007. Available online: <https://hal.inria.fr/inria-00174036> (accessed on 23 January 2021).
24. Brown, D.C. Close-range camera calibration. *Photogramm. Eng.* **1971**, *37*, 855–866.
25. Mvtec. *MvTec Halcon Camera Calibration*; 2012. Available online: https://www.mvtec.com/doc/halcon/12/en/calibrate_cameras.html (accessed on 23 January 2021).
26. Fisher, R.B.; Naidu, D.K., A Comparison of Algorithms for Subpixel Peak Detection. In *Image Technology: Advances in Image Processing, Multimedia and Machine Vision*; Sanz, J.L.C., Ed.; Springer: Berlin/Heidelberg, Germany, 1996; pp. 385–404. [\[CrossRef\]](#)
27. Haug, K.; Pritschow, G. Robust laser-stripe sensor for automated weld-seam-tracking in the shipbuilding industry. In Proceedings of the IECON '98 24th Annual Conference of the IEEE Industrial Electronics Society (Cat. No. 98CH36200), Aachen, Germany, 31 August–4 September 1998; Volume 2, pp. 1236–1241.
28. Forest, J.; Salvi, J.; Cabruja, E.; Pous, C. Laser stripe peak detector for 3D scanners. A FIR filter approach. In Proceedings of the 17th International Conference on Pattern Recognition, ICPR 2004, Cambridge, UK, 26–26 August 2004; Volume 3, 646–649.
29. Schafer, R.W. What Is a Savitzky-Golay Filter? [Lecture Notes]. *IEEE Signal Process. Mag.* **2011**, *28*, 111–117. [\[CrossRef\]](#)
30. Flesia, A.G.; Ames, G.; Bergues, G.; Canali, L.; Schurrer, C. Sub-pixel straight lines detection for measuring through machine vision. In Proceedings of the IEEE International Instrumentation and Measurement Technology Conference (I2MTC), Montevideo, Uruguay, 12–15 May 2014; pp. 402–406.
31. Aggarwal, N.; Karl, W.C. Line detection in images through regularized hough transform. *IEEE Trans. Image Process.* **2000**, *15*, 582–591. [\[CrossRef\]](#) [\[PubMed\]](#)
32. Hagara, M.; Kulla, P. Edge Detection with Sub-pixel Accuracy Based on Approximation of Edge with Erf Function. *Radioengineering* **2011**, *20*, 516–524.

-
33. Fischler, M.A.; Bolles, R.C. Random Sample Consensus: A Paradigm for Model Fitting with Applications to Image Analysis and Automated Cartography. *Commun. ACM* **1981**, *24*, 381–395. [[CrossRef](#)]

**6.2 Publication 2: Optical Dual Laser Based Sensor
Denoising for Online Metal Sheet Flatness
Measurement Using Hermite Interpolation**

Article

Optical Dual Laser Based Sensor Denoising for Online Metal Sheet Flatness Measurement Using Hermite Interpolation

Marcos Alonso ^{1,*} , Alberto Izaguirre ¹, Imanol Andonegui ¹ and Manuel Graña ² 

¹ Robotics and Automation Group, ECS Department, Mondragon University, 20500 Mondragon, Spain; aizaguirre@mondragon.edu (A.I.); iandonegui@mondragon.edu (I.A.)

² Computational Intelligence Group, Computer Science Faculty, University of the Basque Country, UPV/EHU, 00685 San Sebastian, Spain; manuel.grana@ehu.es

* Correspondence: malonson@mondragon.edu

Received: 5 August 2020; Accepted: 19 September 2020; Published: 22 September 2020



Abstract: Flatness sensors are required for quality control of metal sheets obtained from steel coils by roller leveling and cutting systems. This article presents an innovative system for real-time robust surface estimation of flattened metal sheets composed of two line lasers and a conventional 2D camera. Laser plane triangulation is used for surface height retrieval along virtual surface fibers. The dual laser allows instantaneous robust and quick estimation of the fiber height derivatives. Hermite cubic interpolation along the fibers allows real-time surface estimation and high frequency noise removal. Noise sources are the vibrations induced in the sheet by its movements during the process and some mechanical events, such as cutting into separate pieces. The system is validated on synthetic surfaces that simulate the most critical noise sources and on real data obtained from the installation of the sensor in an actual steel mill. In the comparison with conventional filtering methods, we achieve at least a 41% of improvement in the accuracy of the surface reconstruction.

Keywords: cubic Hermite interpolation; laser triangulation; metal sheet; flatness measurement; roller leveling; smooth surface reconstruction; shape measurement system

1. Introduction

Laser based optical sensors have been widely used in industrial environments for various applications like online programming, part measurement and quality control, and part identification and localization.

The requirements for the surface quality of sheet metal products are continuously increasing. Flatness defects are a major problem in many industrial areas such as architectural panel works [1,2] and the automotive industry [3], just to name a few. If the incoming raw material has flatness defects, the manufacturer cannot correct it and must reject it or produce inferior quality products. Therefore, it is critical to ensure that the metal sheet products achieve high quality flatness, meeting customer requirements. Accurate, cost effective, and real-time surface measurement systems are necessary for steel sheet products' online quality assurance.

The flatness of a metal sheet is its levelness when the sheet is free of tension. The main institution providing the definitions of flatness and how to measure it for steel sheet products is the American Society for Testing and Materials (ASTM), allowing purchasers and providers to understand each other using the same characterizations of flatness and the means of the detection of flatness anomalies. The two main standardized measures of flatness are the Steepness Index [4], and the I-Unit [5]. In a sheet whose surface exhibits sinusoidal waves of height H and period L , its Steepness Index value is

defined as H/L . The surface analysis of a metal sheet makes a series of lengthwise virtual cuts of the sheet sample that result in narrow strips, which are commonly referred to as strip fibers. These fibers are treated as lines characterizing the profile of the surface. Using the length of one of these fibers as a reference, L_{ref} , the I-Unit value I_i for an individual fiber i , is defined as:

$$I_i = \Delta L_i / L_{ref} 10^5 \quad (1)$$

where ΔL_i is the difference between the length of the fiber i and the reference fiber L_{ref} , and the constant 10^5 is a standard scaling factor.

Optical sensors based on laser line triangulation are becoming the most widespread solutions to acquire a dense 3D mapping of metal surfaces [6]. Using triangulation techniques, it is possible to compute the surface height from the laser line segmented on the image, where each column of the imaging sensor corresponds to a virtual fiber of the metal sheet. However, these measurements are sensitive to the noise produced by some other mechanical processes, e.g., degreasing, cleaning, polishing, shearing, and transporting roll systems, as well as the illumination effects from the ambient light and the speckles generated by the laser coherent light. Therefore, a high quality flatness measuring system strongly depends on the noise removal methods applied on the captured surface height profile.

The contributions of this paper are the following: (1) the design and implementation in a real industrial operation of a surface flatness sensor that uses two parallel laser lines and an industrial high speed area scan camera providing height maps of the metal sheets moving below the sensor; and (2) a noise removal system based on Hermite polynomial interpolation that effectively removes high frequency noisy wave patterns induced in the sheet by mechanical manipulation. The flowchart in Figure 1 provides a representation of the computational process carried out by the sensor.

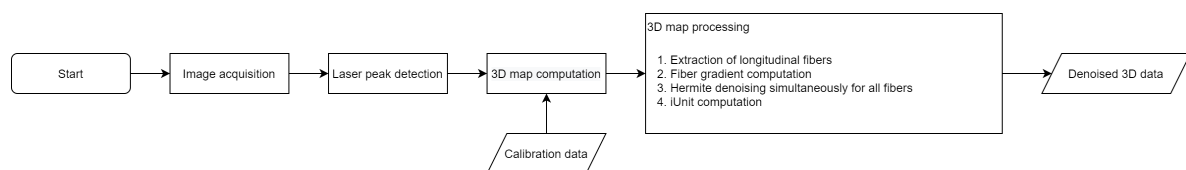


Figure 1. Flowchart of the computational process carried out by the sensor.

The filtering process is validated on synthetic and real industrial production data. This allows analyzing and filtering the information even when the surface flatness information is extremely hidden under the influence of noise sources whose amplitude exceeds several times the amplitude of the original signal. In particular, a noise source produced by a cutting station near the sensor location was removed successfully from the synthetic and real data.

The structure of the paper is as follows: Section 2 reviews the state-of-the-art techniques and devices used to measure the flatness quality of metal sheets. Section 3 focuses on the foundations of laser based optical flatness measurement devices. Section 4 gives the formal details of the numerical method used for improved noise filtering of the fiber surface height measurement maps by Hermite cubic interpolation. Section 5 discusses the sources of numerical errors. Section 6 deals with real-time surface reconstruction processing. Section 7 discusses the performance of the system using both synthetic and real data acquired on a real industrial metal sheet process. Finally, Section 8 gives some conclusions and directions for future work.

2. Related Works

Early metal sheet flatness measurement techniques relied on manual gauging [5], demanding skilled operators able to identify the sheet surface shape deviations for every coil and to manually operate the settings of the roll leveler machine in order to correct these deviations. The first online flatness measuring system, known as the stressometer, was devised using pressure transducers [7] in the late 1960s. Different kinds of shape measurement rolls, based on piezoelectric load sensors

and air-bearing rotors, enabled closed loop control of the roll leveling process with reference to a target profile [8–10]. Whilst shape measurement rolls are currently commonly used in cold rolling mills, they are rarely used in hot, very thick rolled products, roll leveling lines, or finishing lines. The downsides of this measurement technique is that it is very sensitive to force adjustments and can cause scratching of the metal surface.

With the advent of computer vision technologies, optical flatness sensors were introduced [11] to measure manifest flatness, i.e., flatness not hidden by tension. These systems allow measuring smaller defects at higher line-speeds, enabling real-time control and a higher level of integration. The most commonly used optical surface flatness inspection systems are based on the laser triangulation principle [6]. Some designs include several laser emitters for increased robustness [12]. Alternatively, some other optical flatness measuring devices are based on ultra diffuse light or moiré pattern projection. Ultra diffuse light systems use LEDs and an elaborate system of light conductor units and mirrors, ensuring that a uniformly diffuse light bar is projected onto the material. This light bar is recorded with a matrix camera. The light intensity, the light reflection angles, and the change of both factors are evaluated while the material is moving [13]. Moiré pattern projection based systems use the output of a topographic shadow contour pattern, which must be analyzed so that the required 3D information can be formed [14]. These systems are very sensitive to motion error due to the mechanical positioning of the sheets and the shadows and light patterns created by the uncontrolled environmental lighting.

In the computer vision field, there is a long tradition of approaches dealing with surface estimation using gradient data, which are often very noisy [15–19]. Instances of optical based techniques proposed in the literature for the measurement of 3D geometries of objects are the use of deflectometry sensors, able to measure phase changes of light reflected from specular surfaces [20], and the reconstruction of ground surfaces from clouds of points obtained by remote sensors [21]. Integration of 1D gradient data for curve estimation is a well solved problem in the literature [22–26]. However, when dealing with 2D gradient data, we find at least two main kinds of procedures. When the data integration is carried out along specified lines crossing the surface in a privileged direction, we know them as local methods [22,27,28]. Their advantage is their simplicity, low computational cost, and the high resolution recovering height variations. Their disadvantage is their lack of robustness against error propagation along the line. When the data integration is carried out by variational approaches minimizing a functional with 2D support, the approach is a global method [16,29–31], which is more robust to error propagation due to the diverse noise sources due to the metal strip manipulation, but having much greater computational cost, which prevent real-time implementations.

We devised an optical measurement system comprised of two laser lines and a matrix camera that allows the computation of both the height and gradient information along each 1D fiber. Using a combination of both pieces of information, we developed a method capable of obtaining a precise surface reconstruction that is robust against all kinds of noise sources [32,33]. The approach based on piece-wise cubic Hermite spline interpolation is based on a global technique that allows filtering out undesirable noise sources using both surface gradient and height information. Our method addresses this problem by dividing each fiber into multiples pieces, each cubic Hermite spline minimizing both data surface and gradient information, resulting in an interpolated, smooth, globally continuous, and differentiable curve built up as a combination of cubic Hermite splines to retrieve an accurate and real-time estimation of the metal sheet surface, allowing flatness defect detection. We discarded the application of 2D interpolation methods such as bicubic interpolation splines because they do not meet the real-time requirements imposed by the industrial application that sets the stage for this article. For instance, Hermite RBF interpolations [34] are used for denoising scanner data, requiring computational times in the order of minutes, which is obviously out of question to contemplate in our application. A previously published conference paper [35] provides a rough overview discussion of our approach.

3. Laser Based Optical Flatness Measurement System

In this section, we address some fundamental aspects of the implemented sensor, namely the sheet-of-light triangulation principle, optical design considerations, the use of peak image intensity detector techniques, and the calibration of the camera and laser line sensor.

3.1. Sheet-of-Light Triangulation Principle

The sheet-of-light technique is based on the principle of triangulation [36], performing a three-dimensional reconstruction of the surface of an opaque and diffuse reflecting solid by using an area scan camera and a light line projectors. Although sheet-of-light techniques are the most commonly used for surface reconstruction, other laser projected patterns like multiple laser stripes, patterns like circles [37–39], concentric multiple circles, and grids may be used. The proposed flatness sensor relies on sheet-of-light triangulation technique using two laser line projectors. The camera and the line projector must be mounted so that their main axes form an angle for triangulation. The value of this triangulation angle is typically between 30° and 60°. The projected light line defines a plane in 3D space. This plane intersects the surface of the solid under measurement, creating a profile of the surface that is visible to the camera. By moving the solid surface in front of the laser line projector, it is possible to record the whole surface of the solid. In order to increase the measurement range, a Scheimpflug configuration is used, where the detector plane has a tilted angle with respect to the imaging plane [40].

The measurement principle of the sheet-of-light technique is illustrated for a single laser line triangulation setup in Figure 2, where $\mathbf{P} = [X, Y, Z]$ is a point in the world coordinate system and $\mathbf{P}' = [x, y]$ is its projection in the image plane. Equations (2) and (3) show how the 3D point \mathbf{P} can be computed knowing its projection on the camera image plane. Equation (2) corresponds to the projected line of the observation of point \mathbf{P} by the camera, and Equation (3) corresponds to the laser plane. Their intersection provides the desired world coordinates \mathbf{P} .

$$\mathbf{P} = \lambda \mathbf{v} + \mathbf{P}_0 \quad (2)$$

$$\mathbf{n}^T (\mathbf{P} - \mathbf{P}'_0) = [a \ b \ c] \begin{bmatrix} P_x \\ P_y \\ P_z \end{bmatrix} + d = 0 \quad (3)$$

where \mathbf{P}_0 is the camera optical center, \mathbf{v} is the unitary vector between \mathbf{P}_0 and the observed projection of the point \mathbf{P} in the laser plane, $\mathbf{n} = [a, b, c]^T$ is the plane's normal vector, and \mathbf{P}'_0 is any point lying on the laser plane [41].

3.2. Speckle Noise and Spurious Reflections

Sheet-of-light laser triangulation requires robust image segmentation of the laser line in the image captured by the camera. However, spurious reflections and speckle noise make this computation difficult.

Lasers light can be focused in a narrow and bright line. Moreover, the coherent nature of laser light allows using narrow-bandwidth optical filters on the camera, removing image noise from ambient light. However, the downside of coherence is that it creates speckles in the imaging system. Speckles are interference effects of coherent light photons that travel slightly different distances from the source to the sensor, produced by surface roughness at the order of the wavelength of the incident coherent light. It gives a characteristic granular appearance when the surface is imaged under highly coherent light [42]. Speckle noise can impair the segmentation of the laser line in the image. The size of the speckle noise on the image is proportional to the laser wavelength and the lens aperture: a larger aperture generates smaller speckles in the image [43].

Spurious reflections are another big problem in the 3D surface scanning of shiny metallic surfaces. The reflected light from the targeted area of the surface may illuminate some other areas of the same surface that are detected by the segmentation of the images, causing fake measurements [44].

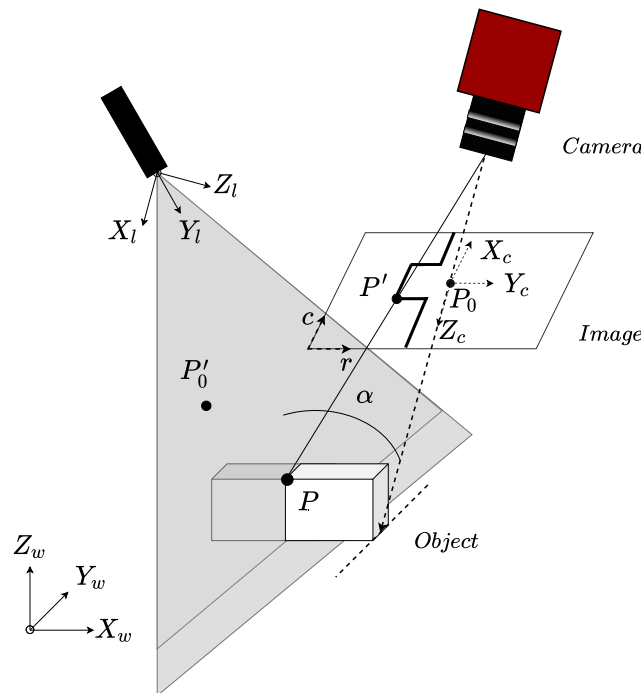


Figure 2. General configuration of a laser triangulation system.

To minimize speckle and spurious reflections, the proposed sensor features a blue laser emitter at wavelength $\lambda = 450$ nm. Red laser emitters ($\lambda = 630$ nm) penetrate deeper into the target surfaces as compared with blue lasers. Therefore, they substantially increase the area of the blurry region corresponding to the laser line captured by the camera. Moreover, blue laser emitters generate a much more focused laser on the object surface, minimizing the light reflected back to the camera.

3.3. Image Intensity Peak Detector

The accuracy of a 3D reconstruction using laser linear illumination is significantly determined by the accuracy of the line segmentation in the image. Since the pattern of image intensity in the normal direction to the line has a Gaussian profile, finding the center of the line in the image corresponds to detecting the point of maximum intensity in the normal direction, also known as the laser peak, which can be detected by different algorithms using the intensity distribution along a column of the sensor image, e.g., finding the position of maximum intensity, finding thresholding points, or finding the center of gravity [45–47]. In the proposed sensor, a Savitzky–Golay [48] finite impulse response (FIR) differential filter is applied to the image intensity profile of the laser line, computing the zero-crossings with sub-pixel accuracy [49–51].

3.4. Sensor Calibration

3.4.1. Background

The purpose of sensor calibration is to identify the camera intrinsic parameters and the mapping between the laser plane and the camera. Since the sensor consists of a laser projector and a camera, camera modeling and calibration become an integral part of the sensor calibration procedure. The conventional approach consists of using first a standard camera calibration technique [52,53] to estimate the camera parameters, then the laser plane parameters are estimated by capturing the

correspondences of 3D known points and applying the least squares method [54–56]. The calibration methods are dependent on the form of calibration target, the method for extracting control points for camera calibration and laser plane calibration, and the calibration algorithms used, for instance the 2D plane with controlled movement [57], and the 3D target with the invariance of the cross ratio [58,59] could be used. An alternative sensor calibration approach consists of finding the mapping function between the image plane and laser plane, treating the sensor as a black box carrying out a plane mapping function. This approach requires the estimation of at least eight parameters [60] by the plane constraint methods [61] or a least squares polynomial fitting method [62].

Scanning large 3D objects, such as flattened rolled metal sheets, implies that the object is moving relative to the 3D scanner. Depth measurements computed from laser triangulation are synchronized with the motion of the metal sheet using an incremental encoder located after the roll leveler stage. This ensures a uniform data acquisition and minimizes the effect of the motion jitter.

3.4.2. Proposed Calibration Method

The standard accuracy requirements in the steel processing industry are as follows: for the height, better than $2\sigma = 0.35$ mm assuming that the measurement error follows a normal distribution with zero mean and σ^2 variance; for the strip cross direction, better than 200 measurement zones per meter. After calibration, our sensor is capable of a height accuracy of $2\sigma = 0.25$ mm and 650 measurement zones per meter. For the proposed sensor, accuracy requirements and the cost effectiveness lead us to use a method based on direct linear mapping functions (DLM). In the pinhole camera model, the mapping between a 3D point in the world coordinate frame to the image coordinate frame is:

$$s\mathbf{m} = \mathbf{K}[\mathbf{R}, \mathbf{t}] \mathbf{M} \quad (4)$$

where $\mathbf{m} = \begin{bmatrix} u, v, 1 \end{bmatrix}^T$ is the vector of homogeneous coordinates in the image plane, $\mathbf{M} = \begin{bmatrix} X_w, Y_w, Z_w, 1 \end{bmatrix}^T$ is the vector of homogeneous 3D coordinates of a point in the world coordinate frame, s is an arbitrary scale factor, \mathbf{R} and \mathbf{t} are the rotation and translation components of the transformation matrix from the world coordinate frame to the camera coordinate frame, and \mathbf{K} is the matrix of intrinsic camera parameters:

$$\mathbf{K} = \begin{bmatrix} \alpha & r & u_s \\ 0 & \beta & v_s \\ 0 & 0 & 1 \end{bmatrix} \quad (5)$$

then we have:

$$s \begin{bmatrix} u \\ v \\ 1 \end{bmatrix} = \mathbf{K} \begin{bmatrix} \mathbf{r}_1, \mathbf{r}_2, \mathbf{r}_3, t \end{bmatrix} \begin{bmatrix} X_w \\ Y_w \\ Z_w \\ 1 \end{bmatrix} \quad (6)$$

assuming that all the calibration points are placed on a plane with $Y_w = 0$ and $\mathbf{R} = [\mathbf{r}_1, \mathbf{r}_2, \mathbf{r}_3]$

$$s \begin{bmatrix} u \\ v \\ 1 \end{bmatrix} = \mathbf{K} \begin{bmatrix} \mathbf{r}_1, \mathbf{r}_3, t \end{bmatrix} \begin{bmatrix} X_w \\ Z_w \\ 1 \end{bmatrix} \quad (7)$$

Define $\mathbf{H} = \mathbf{K} \begin{bmatrix} \mathbf{r}_1, \mathbf{r}_3, t \end{bmatrix}$, $\mathbf{m} = \begin{bmatrix} u, v, 1 \end{bmatrix}^T$, and $\mathbf{M} = \begin{bmatrix} X_w, Z_w, 1 \end{bmatrix}^T$; we obtain the following expression for the mapping between the 2D image points and the 3D calibration planar points:

$$s\mathbf{m} = \mathbf{H}\mathbf{M} \quad (8)$$

Given a set of calibration points and their corresponding image coordinates, the transformation matrix \mathbf{H} , also known as homography, can be estimated by solving the previous linear equation. Let us assume that the laser plane XZ is our reference coordinate system. Let $\mathbf{P}_{li} = [X_{li}, Z_{li}]$ be a point in the laser plane and $\mathbf{P}_{ci} = [X_{ci}, Y_{ci}]$ the corresponding image plane point. The mapping between these two planes is given by:

$$s \begin{bmatrix} X_{ci} \\ Y_{ci} \\ 1 \end{bmatrix} = \begin{bmatrix} h_{11} & h_{12} & h_{13} \\ h_{21} & h_{22} & h_{23} \\ h_{31} & h_{32} & h_{33} \end{bmatrix} \begin{bmatrix} X_w \\ Z_w \\ 1 \end{bmatrix} \quad (9)$$

We estimated the intrinsic parameters of the camera before the installation of the camera in the sensor by a previous calibration process at the lab, achieving an average reprojection error of 0.04 pixels. We carry out the correction of the lens radial distortion so the mapping from the image plane to the laser plane becomes a linear function. The mapping transformation \mathbf{H} can be estimated by minimal linear least squares:

$$\begin{aligned} sX_{ci} &= h_{11}X_{li} + h_{12}Z_{li} + h_{13} \\ sY_{ci} &= h_{21}X_{li} + h_{22}Z_{li} + h_{23} \\ s &= h_{31}X_{li} + h_{32}Z_{li} + h_{33} \end{aligned} \quad (10)$$

For a set of corresponding points $\{\mathbf{P}_{li} = [X_{li}, Z_{li}]\}_i$ and $\{\mathbf{P}_{ci} = [X_{ci}, Y_{ci}]\}_i$, we can set $h_{33} = 1$ without loss of generality. Rearranging the system of equations of Equation (10), we get a linear system of equations $\mathbf{HA} = \mathbf{0}$, where \mathbf{A} and \mathbf{H} are given by Equation (11).

$$\mathbf{A} = \begin{bmatrix} -X_{li} & -Z_{li} & -1 & 0 & 0 & 0 & X_{ci}X_{li} & X_{ci}Z_{li} & X_{ci} \\ 0 & 0 & 0 & -X_{li} & -Z_{li} & -1 & Y_{ci}X_{li} & Y_{ci}Z_{li} & Y_{ci} \\ \vdots & \vdots & \vdots & \vdots & \vdots & \vdots & \vdots & \vdots & \vdots \\ -X_{ln} & -Z_{ln} & -1 & 0 & 0 & 0 & X_{cn}X_{ln} & X_{cn}Z_{ln} & X_{cn} \\ 0 & 0 & 0 & -X_{ln} & -Z_{ln} & -1 & Y_{cn}X_{ln} & Y_{cn}Z_{ln} & Y_{cn} \end{bmatrix}_{2n \times 9} \quad (11)$$

$$\mathbf{H} = \begin{bmatrix} h_{11} \\ h_{12} \\ \vdots \\ h_{32} \\ h_{33} \end{bmatrix}_{1 \times 2n} \quad (12)$$

3.5. Dual Linear Laser Flatness Sensor

The proposed flatness sensor is comprised of two illuminating parallel linear laser sources perpendicular to the metal sheet translation axis separated by a distance $\Delta_d = 100$ mm from each other and a CCD camera capturing the area illuminated by the lasers, as shown in Figure 3.

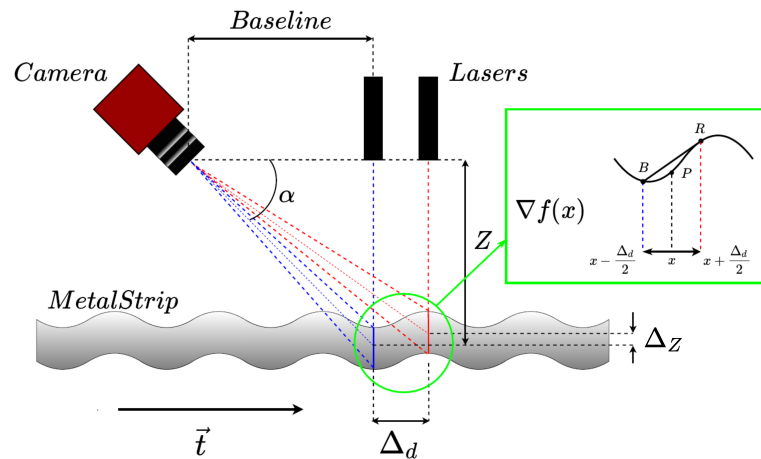


Figure 3. Design of the laser-camera sensor featuring two parallel laser lines allowing the computation of surface height and its gradient. The color of the representation is not related to the actual laser color, which is the same for both laser sources.

This dual laser line approach allows separating high frequency vertical vibrations from low frequency flatness defects by detecting variations between lasers lines [12], as shown in the inset of Figure 3. In the implemented sensor, the baseline separation between camera and laser sources is $\Delta_B = 900$ mm, and the triangulation angle is $\alpha = 45^\circ$ so that the center of the camera captures the middle of both laser lines at $Z = 0$ mm. The displacement between laser emitters is $\Delta_d = 100$ mm. The laser line emitters are collimated, and their wavelength is $\lambda = 450$ nm, while their line aperture is 90° . The camera features a 2048×2048 matrix CCD sensor, and the focal length of the lens is $f = 6$ mm, placed at $Z = 1140$ mm over a moving steel strip. The information of both laser lines allows the local gradient to be calculated as the slope of the line joining two measured points corresponding to each laser line, as seen in the inset of Figure 3. This slope remains constant no matter what vertical displacements of the metal sheet surface are produced. The height value P at point x is computed as $P = (B + R)/2$ under the assumption that the gradient does not change significantly in the interval $\left[x - \frac{\Delta_d}{2}, x + \frac{\Delta_d}{2}\right]$.

The proposed optical flatness sensor was installed in a finishing process line just after an industrial roll leveler close to a cutting station, as shown in Figure 4. The precision roller leveler has 13 rolls with a diameter of 130 mm. This leveler has the ability to apply controlled roll bend through flights of adjustable backup rollers. This line is capable of processing hot rolled materials with yield strengths in the range [300, 700] MPa (mild steel) and thickness ranging from 3 mm to 8 mm. The sensor shown in Figure 5 is clamped to a frame placed at the output of the leveler, and it is isolated from its structure by a polymer that efficiently reduces the vibrations produced by the manufacturing process.

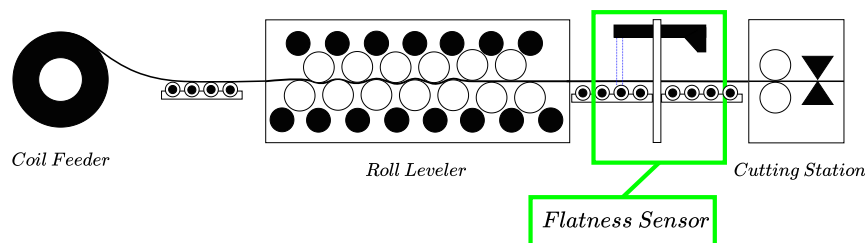


Figure 4. A simplified block diagram showing an industrial finishing line. The flatness sensor lies between the roll leveler and the cutting station.



Figure 5. Close view of the devised sensor comprised of two linear lasers and a camera, installed over an industrial steel roll leveler processing line.

4. Cubic Hermite Spline Interpolation with Global Continuous Derivatives

The approximation of surface profiles by splines allows the detection of surface defects as regions of the surface that show a high distance relative to the approximating spline functions [32]. Specifically, the transform based on Hermite splines has a very convenient property, namely that the coefficients of a function corrupted with Gaussian noise follow a Gaussian distribution [63]. This property allows efficient denoising by simple thresholding of the coefficients. A cubic Hermite interpolator is a third order parametric polynomial curve $Z(t) = \mathbf{T}\mathbf{M}_H\mathbf{G}_H$, where $t \in [0, 1]$, \mathbf{T} is a row vector containing the coefficients of the third order polynomial function, \mathbf{M}_H is the square matrix form composed of the four Hermite basis functions, and \mathbf{G}_H is the column vector form composed of the interval endpoints values and their derivatives,

$$\begin{aligned} \mathbf{T} &= \begin{bmatrix} t^3 & t^2 & t & 1 \end{bmatrix} \\ \mathbf{M}_H &= \begin{bmatrix} 2 & 1 & -2 & 1 \\ -3 & -2 & 3 & -1 \\ 0 & 1 & 0 & 0 \\ 1 & 0 & 0 & 0 \end{bmatrix} \\ \mathbf{G}_H &= \begin{bmatrix} \rho(0) & \rho'(0) & \rho(1) & \rho'(1) \end{bmatrix}^T \end{aligned} \quad (13)$$

where $\rho(0)$ and $\rho(1)$ are the values at the boundaries of each interpolated curve, which may correspond to a surface fiber in our application, and $\rho'(0)$ and $\rho'(1)$ are their corresponding first derivatives with respect to t . A series of curve sampling intervals $\{\rho_k, \rho'_k\}_{k=1}^n$ can be interpolated by imposing boundary conditions such that the derivatives are continuous at the endpoints of neighboring intervals. These boundary conditions yield an interpolated curve consisting on cubic Hermite splines that is globally continuous and differentiable in $(t(1), t(k))$, i.e., it belongs to C^0 and C^1 [64].

However, in order to use the piece-wise cubic Hermite interpolation method, several considerations must be taken into account. On the one hand, the surface fiber recovered from the sensor must have a signal-to-noise ratio (SNR) high enough to allow data interpolation. On the other hand, according to the Nyquist–Shannon sampling theorem [65], the gradient data sampling frequency must be at least twice that of the highest frequency of the original signal. Thus, the accuracy of the surface gradient is determined by the distance between the sensor laser projection planes. The flatness defects produced by leveling processes are of a much lower frequency than the sensor sampling frequency. Therefore, in the absence of high frequency vibrations due to mechanical effects, the system has enough resolution to acquire the relevant flatness information.

5. Sources of Error

There are two different sources of error in the laser-camera triangulation process. One is the error in the estimation of the homography between the laser planes, and the other is the sub-pixel laser detection errors described in Section 3.1.

5.1. Measurement Errors Due to the Laser-Camera Triangulation

Due to the fact that the homography is estimated using several points, the errors due to this estimation may overcome the errors induced by the laser line intensity peak detection in the image. The segmentation errors of the laser points projected in the image plane have a normal distribution, zero mean, and a standard deviation σ . Therefore, the reprojection errors propagate to the estimation of the real-world coordinates using the homography as follows:

$$\tilde{\mathbf{p}}_{mm} = \mathbf{H}(\tilde{\mathbf{p}}_{px} + \tilde{\mathbf{e}}_{px}) \quad (14)$$

where \mathbf{H} is the homography, $\tilde{\mathbf{p}}_{mm} \in \mathbb{R}^2$ are the homogeneous coordinates of the real triangulated point, $\tilde{\mathbf{p}}_{px} \in \mathbb{R}^2$ are the homogeneous coordinates of the segmented point in the image plane, and $\tilde{\mathbf{e}}_{px} \in \mathbb{R}^2$ is the reprojection error with the last row value equal to zero.

5.2. Measurement Errors Due to the Gradient Estimation

Gradient estimation errors are due to numerical differentiation, truncation, and round-off errors [66]. The error bounds between the truncated Taylor expansion of the 1D function derivative and the central difference computed at point \mathbf{p}_{mm} are:

$$|E_d| \leq \left| \frac{h^2}{6} f'''(\xi) \right| + \left| \frac{\epsilon}{h} \right| \quad (15)$$

where $\left| \frac{h^2}{6} f'''(\xi) \right|$ is the Taylor expansion truncation error at point with h the step of the central difference in \mathbf{p}_{mm} and $\left| \frac{\epsilon}{h} \right|$ the round-off error.

Flatness calculation in rolled metal steel assumes that flatness defects can be approximated by sinusoidal waveforms, so that the maximum absolute derivative $|E_s|$ and the relative estimation errors η for a sinusoidal fiber along the unrolled metal sheet of amplitude B and period τ , respectively, are given by the following Equations:

$$|E_s| \leq \frac{B}{6} \left(\frac{2\pi}{\tau} \right)^3 h^2 \quad (16)$$

$$\eta \leq \frac{1}{6} \left(\frac{2\pi}{\tau} \right)^2 h^2 \quad (17)$$

6. Real-Time Surface Reconstruction Based on Hermite Interpolation

To inspect rolled products detecting flatness defects, it is necessary to scan the sheet as it moves along the processing line. The feeding rate of some lines reaches speeds up to 120 m/min, posing stringent requirements for accurate real-time surface estimation.

To compute the noise-free reconstruction of one metal strip fiber $\hat{\mathbf{f}}$ using piece-wise Hermite cubic interpolation, the fiber is uniformly partitioned into n intervals, each one discretized into m samples of its height measurement z_1, \dots, z_m . Height derivatives z'_1, \dots, z'_m are computed using the information retrieved from the proposed two laser line sensor. Consecutive intervals must be continuous functions in C_0, C_1 . The boundary conditions of the signal intervals are set according to the computing strategy shown in Figure 6, i.e., the last measure of an interval is the first one for the next interval.

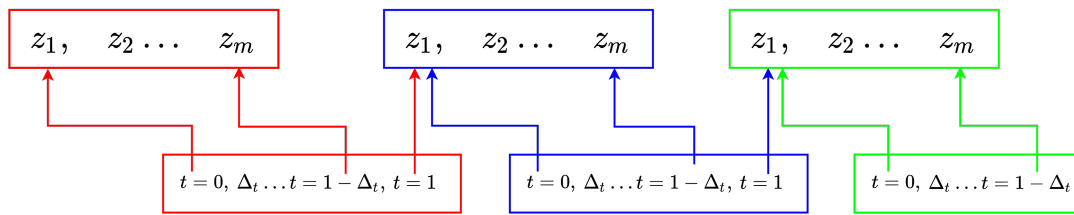


Figure 6. Scheme showing the signal partition scheme followed to allow Hermite splines' interpolation.

In Figure 6, $\Delta t = 1/m$, and the value z_1 corresponding to the next interval is both calculated as the Hermite value for $t = 1$ of the actual interval and also for $t = 0$ of the next interval. The same computational scheme is applied to the derivatives, leading to the following linear equation $\hat{\mathbf{f}} = \mathbf{G}(\mathbf{f}) \mathbf{A}$, which is constructed as follows:

$$\hat{\mathbf{f}} = \begin{bmatrix} \rho_1 \\ \rho_2 \\ \vdots \\ \rho_n \\ \rho'_1 \\ \rho'_2 \\ \vdots \\ \rho'_n \end{bmatrix} = \begin{bmatrix} \mathbf{A}_H & 0 & 0 & \dots & 0 \\ 0 & \mathbf{A}_H & 0 & \dots & 0 \\ \vdots & \vdots & \vdots & \vdots & \vdots \\ 0 & 0 & 0 & \dots & \mathbf{A}_H \\ \mathbf{A}'_H & 0 & 0 & \dots & 0 \\ 0 & \mathbf{A}'_H & 0 & \dots & 0 \\ \vdots & \vdots & \vdots & \vdots & \vdots \\ 0 & 0 & 0 & \dots & \mathbf{A}'_H \end{bmatrix}_{(2n \times m) \times (4 \times n)} \quad (18)$$

where:

$$\mathbf{A}_H = \begin{bmatrix} \mathbf{T} \mathbf{M}_H(t=0) \\ \vdots \\ \mathbf{T} \mathbf{M}_H(t=1-\Delta t) \end{bmatrix}_{m \times 4} \quad (19)$$

$$\mathbf{A}'_H = \begin{bmatrix} \mathbf{T}' \mathbf{M}_H(t=0) \\ \vdots \\ \mathbf{T}' \mathbf{M}_H(t=1-\Delta t) \end{bmatrix}_{m \times 4}$$

and:

$$\rho_i = [z_{i1}, \dots, z_{im}]^T$$

$$\rho'_i = [z'_{i1}, \dots, z'_{im}]^T$$

z_{ij} and z'_{ij} correspond to the measured height of the j th sample and its derivative at the i th interval of the fiber \mathbf{f}_i , respectively. For a fiber \mathbf{f}_i , these derivatives are computed as follows:

$$\frac{\Delta \mathbf{f}_i}{\Delta t} = \frac{\Delta \mathbf{f}_i}{\Delta x} \frac{\Delta x}{\Delta t} \quad (20)$$

where Δx is the actual discretization step in the direction of the surface translation. Finally, $\mathbf{G}(\mathbf{f})$ contains the end points and its derivatives for each sampled interval along fiber \mathbf{f} , which can be calculated by linear methods. Real-time computation using the previous scheme can be extended to all the fibers captured over the total metal sheet surface, resulting in:

$$[\hat{\mathbf{f}}_1 \dots \hat{\mathbf{f}}_K] = \mathbf{A} [\mathbf{G}(\mathbf{f}_1) \dots \mathbf{G}(\mathbf{f}_K)] \quad (21)$$

where:

$$\mathbf{G}(\mathbf{f}_k) = [\rho_{i1}^T, \dots, \rho_{in}^T | \rho_{i1}'^T, \dots, \rho_{in}'^T]^T \quad (22)$$

The matrix \mathbf{A} is common to all longitudinal metal sheet fibers $\{\mathbf{f}_k\}_{k=1}^K$; therefore, it is computed only once, facilitating real-time implementation.

7. Results

We apply the proposed polynomial filtering and reconstruction method to both simulated and real data in order to test its ability to remove high frequency noise due to mechanical manipulation of the metal sheet.

7.1. Synthetic Data Results

We created a synthetic surface showing two of the most common defects in a roll leveler processing line, namely center buckles and wavy edges. The period and amplitude of these sinusoidal flatness defects are 1800 mm and 12 mm on the translation axis of the metal sheet and 1500 mm and 12 mm across the width of the metal sheet, respectively. The simulated surface is shown in

The first computational experiment is carried out over the synthetic surface described above without additional noise, in order to simulate an ideal production line and check the accuracy of our method. The surface filtering has been made with a sampling interval for the Hermite interpolation of $\Delta_x = 3$ mm. Each fiber interval contains 33 samples, which corresponds to the distance between lasers (Δ_d). The total length of the sheet is 9000 mm. The proposed Hermite filtering method maximum surface reconstruction error is $0.64 \mu\text{m}$ with standard deviation $\sigma = 0.16 \mu\text{m}$. The relative error in the gradient computation according to the theoretical maximum error defined by Equation (16) is 0.507% for $h = \Delta_d/2$.

In the second computational experiment, we introduced different kinds of noise to simulate the vibrations induced in the sheet metal as a result of the mechanical elements of the roll leveler line. Additionally, we introduced another noise source controlled by a single parameter that simulates the triangulation error of the 3D sensor. The noise sources that characterize the mechanical vibrations have an amplitude of 2.5 mm following a Gaussian distribution. A high frequency sinusoidal signal with a maximum amplitude of 0.5 mm and a spatial period of 50 mm is also added in order to simulate the eccentricity of the rolls over which the sheet is displaced. The noise introduced as a consequence of the laser peak detection error has a standard deviation of 1/16 pixel, which corresponds to typical camera laser peak detection errors. The results obtained comparing the reconstructed surface to the theoretical noise-free surface are a maximum estimation error of 0.35 mm and a standard deviation of 0.12 mm. These errors meet the standards currently used to measure flatness quality in roll leveled products.

In the third experiment, we added a localized damped sine wave along the longitudinal axis of the synthetic sheet with an initial amplitude of the envelope of 50 mm, a decay constant of 0.07, and a period of 10 mm. This signal models the vibrations induced by a sheet metal cutting station located near the scanning area, as shown in Figure 7. The existing literature rarely considers the effects produced by processes subsequent to the roll leveling. Using our filtering method, we obtain a maximum error of 1.15 mm and a standard deviation of 0.38 mm.

These results show that the Hermite interpolation filtering method is very robust and that it enables an accurate and reliable surface estimation despite the presence of external noise sources, improving over other methods based on FIR techniques, e.g., Butterworth, Savitzky–Golay, etc. Figure 8 shows the the estimated filtered surface from the noisy surface data of Figure 7. Maximum errors occur at the high amplitude damped noise regions, due to the loss of reliable surface height information obtained by the sensor. These results are also shown in Figure 9, where the raw data retrieved from the sensor are shown first, the estimated surface using our method is presented in the middle, and finally, two insets provide more detailed information from the dashed areas colored in red and blue color, respectively.

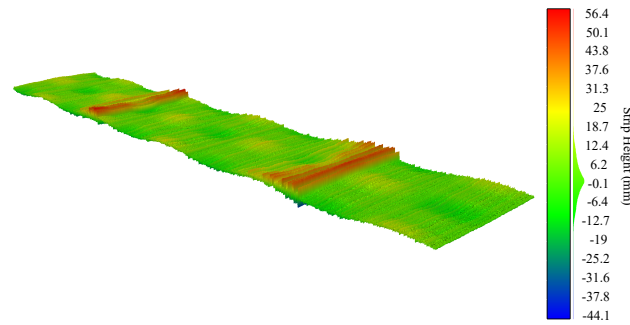


Figure 7. The synthetic surface after adding the effect of vibrations induced by different mechanical sources such as the shearing station (noise sources added).

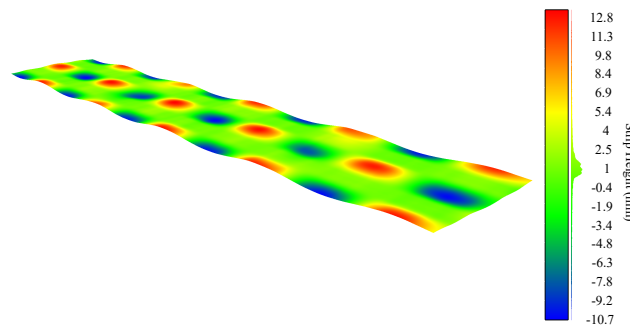


Figure 8. 3D representation of the theoretical surface results after applying the proposed filtering method.

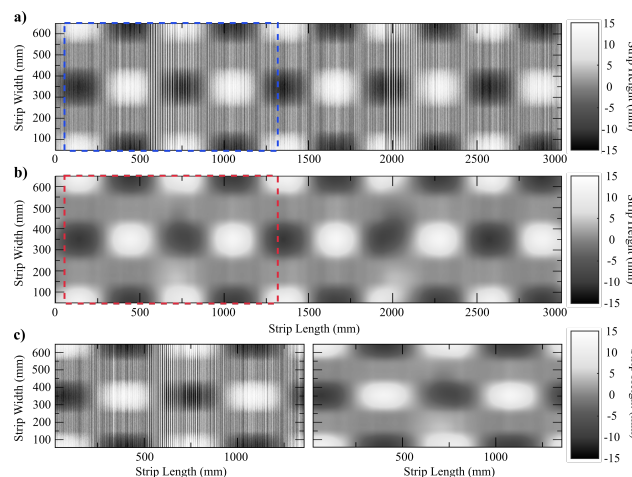


Figure 9. Visualization as a grayscale image of the synthetic surface results of the interpolation with Hermite splines. (a) Synthetic surface corrupted with high frequency noisy vibrations; (b) filtered surface; (c) a close up view of a region in both images. Intensity corresponds to height relative to the mean of the surface. White = positive; dark = negative.

These results show that the flatness sensor and the proposed filtering method are both robust and accurate enough against different noises sources, in particular to localized high amplitude noises produced by a simulated cutting station placed after the rolling leveler and the devised 3D sensor.

For a quantitative evaluation of the improvement achieved by our proposal, we implemented the following approaches for surface denoising:

1. A moving-average filter featuring a sliding window of 33 samples in length.
2. A third order low-pass Chebyshev Type II filter [67] with 33 dB of stopband attenuation and a stopband edge frequency of 0.02 specified in normalized frequency units.
3. A third order Savitzky–Golay FIR smoothing filter [48] with a frame length of 99 samples.
4. A third order Butterworth IIR digital filter [68] with a cutoff frequency for the point 6 dB below the passband value of 0.01 specified in normalized frequency units.

Table 1 presents the comparative results of the implemented denoising methods over the synthetic surface discussed above. Improvements in MAE achieved by our approach range from 45% relative to the Butterworth filter approach up to 50% relative to the Savitzky–Golay approach. Regarding the RMSE, our approach improves by 41% over the second best approach, and up to 49% over the Chebyshev filter.

Table 1. Comparative results of our approach with other conventional denoising approaches. MAE = mean absolute error; MaxAE = maximum absolute error; STD = standard deviation of the absolute error; RMSE = root mean squared error.

Method	MAE	MaxAE	STD	RMSE
Hermite (ours)	0.413	1.15	0.38	0.459
Butterworth	0.760	4.423	0.735	0.781
Savitzky–Golay	0.842	6.436	0.779	0.853
Moving Average	0.801	5.463	0.928	0.865
Chebyshev Type II	0.828	5.040	0.828	0.903

7.2. Results on Real Industrial Data

During the experimental data acquisition, we used sheet samples from two kinds of steel S235JR steel coils (thicknesses of 3mm, Young’s modulus $E = 205$ GPa, Poisson’s ratio $\nu = 0.301$, yield stress $\sigma_0 = 215$ MPa) and S500MC high yield steel coils (a thickness of 8 mm, Young’s modulus $E = 210$ GPa, Poisson’s ratio $\nu = 0.304$, yield stress $\sigma_0 = 500$ MPa), which are middle carbon steels manufactured by rolling. They are annealed and skin passed. The coil specimens have a length of about 800 m. The sensor takes measurements along 3000 mm in each measurement cycle. The widths are in the range [800, 2300] mm. The behavior of these specimens was characterized by uniaxial tensile tests conducted at room temperature. The raw depth information from the sensor for samples of these two different kinds of steel coil are visualized as grayscale images in Figures 10a and 11a. Flatness information is highly corrupted by high frequency noisy vibrations from the cutting station and other mechanical effects on the steel sheet. Namely, the cutting station produces high amplitude/high frequency noisy waves on the metal strip every T seconds depending on the cutting length program, and the conveyor belt produces overall high frequency waves. The resulting interference pattern is a rather complex spatial form of noise, hindering the detection of flatness defects.

The proposed flatness measuring sensor succeeds at acquiring the surface information at the real-time production speed of 30 m/min. The Hermite polynomial filtering procedure manages to successfully retrieve the surface features of the material and the denoised flatness measures, as shown in Figures 10b and 11b, depicting the smooth reconstructed surface after the noisy waves have been removed. In Figure 11b, filtering unveils center buckles, i.e., another kind of common flatness defect in which sinusoidal waves restrain the central fibers of the metal sheet. Finally, Figure 12 shows the reconstruction of one of the surface fibers from the raw data of Figure 10.

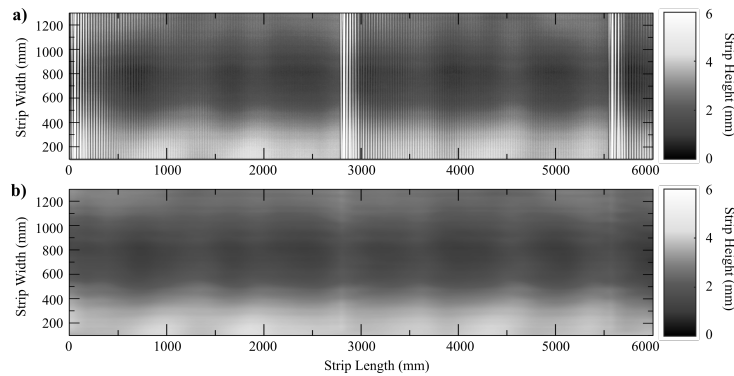


Figure 10. (a) Sensor raw data for a S235JR steel coil with observed high frequency transient noisy waves and background noise. (b) Denoised sensor data using the proposed Hermite interpolation filtering method.

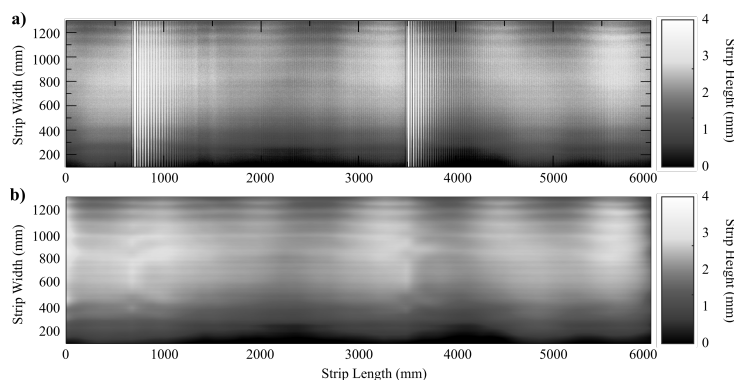


Figure 11. (a) Sensor raw data for a S500MC high yield steel coil with with observed periodic transient impulses and background noise. (b) Denoising results of the sensor raw data using the proposed Hermite interpolation filtering method.

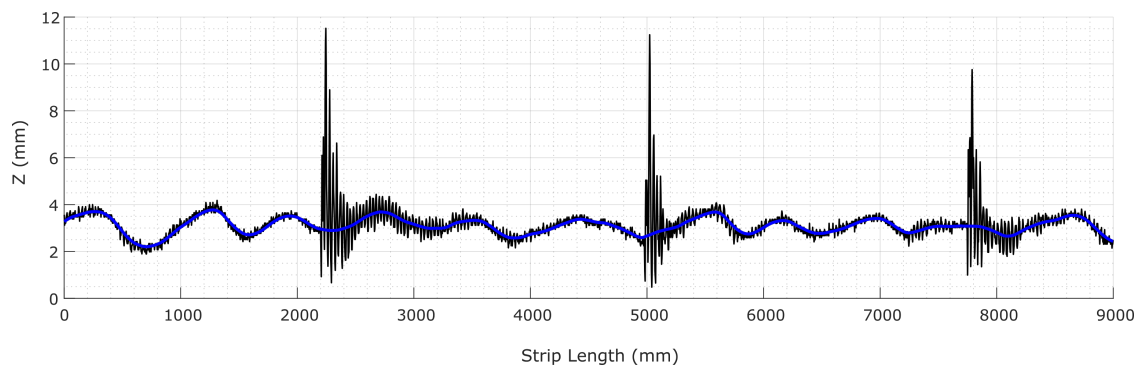


Figure 12. An instance of longitudinal fiber reconstruction (light blue line) by Hermite interpolation from the raw data of Figure 10 (dark line).

7.3. Limitations of the Real Data Results

Estimation of the measurement error on real sensor measures remains very challenging. Actually, there is no way to carry out a fair comparison between the measures obtained by our sensor with those of a precision measuring instrument, such as a coordinate-measuring machine (CMM). Measuring a test specimen of a metal sheet out of the roll leveling machine with a CMM has some inherent bias, because the sheet is released from tensile and traction stresses, while our optical sensor measures the strip under stress. Therefore, the flatness measures yielded by a CMM cannot be fairly compared with those of an online sensor measuring the actual production.

The measuring device and the filtering method proposed in the manuscript solves flatness data reconstruction in a real-time framework. In fact, it takes an average of 0.35 s seconds to filter a metal

sheet of 6000 mm in length by 2300 mm in width. The sampling distance in the longitudinal direction (rolling direction) is 3 mm and in the transversal direction is 2 mm; thus 1150 fibers are computed concurrently in this time. The time that this sheet will take to go under the measuring sensor at maximum speed of 120 m/min is about 3 s, so that real-time measurement is feasible in operational conditions. Furthermore, our system uses a first in first out (FIFO) queue to store acquired data until the filtering process finishes.

The proposed sensor relies on the motion of the steel sheet for the measurement. Doing the measurements off-line for comparison with contact sensor measurements carried out off-line would require building up a complete setup where the sensor is displaced over the cut steel plate. We carried out some comparisons of the measurements done by the sensor online with off-line measurements by shape measurement rolls. The differences were on the order of 0.25 mm, within standard industry resolution requirements. It must be taken into account that the off-line contact sensor measurements do not suffer from the transport tension, cutting, and other vibration sources.

Finally, this method can be used to concatenate as many processed sheets as needed. In order to ensure the C_0 , C_1 continuities between consecutive processed sheets, the Hermite surface reconstruction method can be easily enhanced, by imposing as boundary conditions for the actual piece the height values and the derivatives of the previous piece.

8. Conclusions

In this paper, we propose a hardware-software system that carries out in real time the estimation of the flatness of a metal strip moving below the unrolling mill that flattens a roll of steel cutting it into sheets of predefined lengths. Online quality inspection of the unrolled metal strip before cutting is achieved by this system. The standard flatness anomalies to be detected are wavy edges, center buckles, and bow defects, which are low frequency variations in the height of the metal surface. The mechanical manipulation of the metal, such as the jerking due to the strip pulling and tugging, and the cutting process, induces high frequency variations in surface height that are successfully removed by our surface reconstruction software system, which is based on a Hermite interpolation approach.

The nonlinear combination of the different noise sources on this particular process means that filtering the sensor signals with the desired precision cannot be achieved by conventional linear filtering techniques. We validated the filtering approach on synthetic and real industrial operation data, showing significant improvement over linear conventional approaches. In the comparison with Savitzky–Golay, Chebyshev, and Butterworth filters applied to the reconstruction of the surface after noise addition, we achieved more than a 41% improvement. Furthermore, we were able to assess the accuracy of the sensor against off-line contact sensor measurements, reporting an average error of 0.25 mm within standard industry accuracy requirements.

The proposed sensor and surface reconstruction system can pave the way for online closed-loop control systems, low cost real-time flatness quality inspection, and high efficiency and quality manufacture of rolled steel products. More extensive and detailed analysis of the impact of gradient estimation numerical errors should be carried out.

Author Contributions: Conceptualization, M.A., A.I., and M.G.; methodology, M.A., I.A., and M.G.; software, M.A., A.I., and I.A.; validation, M.A.; formal analysis, M.A. and M.G.; writing, original draft preparation, M.A., A.I., I.A., and M.G.; writing, review and editing, M.A. and M.G.; visualization, M.A. and I.A.; project administration, M.G.; funding acquisition, M.G. All authors read and agreed to the published version of the manuscript.

Funding: This work was partially supported by FEDER funds through MINECO project TIN2017-85827-P, RFCS EU funded project FLATBEND with Grant Number 800730, and Grant IT1284-19 of the university research group of excellence from the Basque Government.

Conflicts of Interest: The authors declare no conflict of interest.

Abbreviations

The following abbreviations are used in this manuscript:

ASTM American Society for Testing and Materials

References

1. Zahner, L. *Architectural Metals: A Guide to Selection, Specification, and Performance*; Wiley: Hoboken, NJ, USA, 1995.
2. Zahner, L. *Stainless Steel Surfaces: A Guide to Alloys, Finishes, Fabrication and Maintenance in Architecture and Art*; Architectural Metals Series; Wiley: Hoboken, NJ, USA, 2019.
3. Llewellyn, D. *Steels: Metallurgy and Applications*; Elsevier Science: Amsterdam, The Netherlands, 2013.
4. ASTM A568/A568M-17a. Standard Specification for Steel, Sheet, Carbon, Structural, and High-Strength, Low-Alloy, Hot-Rolled and Cold-Rolled, General Requirements for. 2017. Available online: <https://www.astm.org/Standards/A568.htm> (accessed on 22 September 2020).
5. ASTM A1030/A1030M-11, Measuring Flatness Characteristics of Steel Sheet Products, Standard Practice for. 2011. Available online: <https://www.astm.org/DATABASE.CART/HISTORICAL/A1030A1030M-11.htm> (accessed on 22 September 2020).
6. Molleda, J.; Usamentiaga, R.; García, D.F. On-Line Flatness Measurement in the Steelmaking Industry. *Sensors* **2013**, *13*, 10245–10272. [CrossRef] [PubMed]
7. Sivilotti, O.; GuiseppePervi, C. Arrangement in Strip Rolling Mills for Measuring the Distribution of the Strip Tension Over the Strip Width. Germany Patent DE1573407B1, November 1966.
8. Bergman, G.; Enneking, A.; Helmut Thies, K. Displacement-Type Shape Sensor for Multi-Roll Leveler. U.S. Patent 6,857,301, February 2005.
9. Tsuzuki, S.; Kira, Y.; Misumi, K. Flatness Control System of Cold Rolling Process with Pneumatic Bearing Type Shape Roll. *IHI Eng. Rev.* **2009**, *42*, 54–60.
10. *Air Bearing Shapemeter, Shapemeter for the Rolling Industry*; White Paper; Primetals: London, UK, 2015.
11. Jouet, J.; Francois, G.; Tourscher, G.; de Lamberterie, B. Automatic flatness control at Solmer hot strip mill using the Lasershape sensor. *Iron Steel Eng.* **1988**, *65*, 50–56.
12. Kierkegaard, P.; Classon, L.A. A new-generation optical flatness measurement system. *Iron Steel Technol.* **2015**, *12*, 76–81.
13. Vollmer, F. *VIP08 Flatness Measurement System*; Sucuri Inc.: Canaan, CT, USA, 2010. Available online: <https://vollmeramerica.com/vip-08-flatness-measurement-system/> (accessed on 22 September 2020).
14. Paakkari, J. On-Line Flatness Measurement of Large Steel Plates Using Moiré Topography. Ph.D. Thesis, The University of Oulu, Oulu, Finland, 1998.
15. Agrawal, A.; Chellappa, R.; Raskar, R. An algebraic approach to surface reconstruction from gradient fields. In Proceedings of the Tenth IEEE International Conference on Computer Vision (ICCV'05) Volume 1, Beijing, China, 17–21 October 2005; Volume 1, pp. 174–181. [CrossRef]
16. Frankot, R.T.; Chellappa, R. A method for enforcing integrability in shape from shading algorithms. *IEEE Trans. Pattern Anal. Mach. Intell.* **1988**, *10*, 439–451. [CrossRef]
17. Karaçali, B.; Snyder, W. Reconstructing Discontinuous Surfaces from a Given Gradient Field Using Partial Integrability. *Comput. Vis. Image Underst.* **2003**, *92*, 78–111. [CrossRef]
18. Klette, R.; Schluens, K. Height data from gradient maps. In *Machine Vision Applications, Architectures, and Systems Integration V*; Solomon, S.S., Batchelor, B.G., Waltz, F.M., Eds.; International Society for Optics and Photonics (SPIE): Bellingham, WA, USA, 1996; Volume 2908, pp. 204–215. [CrossRef]
19. Agrawal, A.; Raskar, R.; Chellappa, R. What Is the Range of Surface Reconstructions from a Gradient Field? In *Computer Vision—ECCV 2006*; Leonardis, A., Bischof, H., Pinz, A., Eds.; Springer: Berlin/Heidelberg, Germany, 2006; pp. 578–591.
20. Knauer, M.C.; Kaminski, J.; Hausler, G. Phase measuring deflectometry: A new approach to measure specular free-form surfaces. In *Optical Metrology in Production Engineering*; Osten, W., Takeda, M., Eds.; International Society for Optics and Photonics (SPIE): Bellingham, WA, USA, 2004; Volume 5457, pp. 366–376. [CrossRef]
21. Rychkov, I. Locally controlled globally smooth ground surface reconstruction from terrestrial point clouds. *arXiv* **2012**, arXiv:1206.0513.

22. Wu, Z.; Li, L. A line integration based method for depth recovery from surface normals. In Proceedings of the 9th International Conference on Pattern Recognition, Rome, Italy, 14 May–17 November 1988; Volume 1, pp. 591–595, doi:10.1109/ICPR.1988.28301. [[CrossRef](#)]
23. Yaroslavsky, L.P.; Moreno, A.; Campos, J. Frequency responses and resolving power of numerical integration of sampled data. *Opt. Express* **2005**, *13*, 2892–2905. [[CrossRef](#)]
24. Elster, C.; Weingartner, I. High-accuracy reconstruction of a function $f(x)$ when only $df(x)/dx$ or $d(2)f(x)/dx(2)$ is known at discrete measurement points. In *X-ray Mirrors, Crystals, and Multilayers II*; Freund, A.K., Macrander, A.T., Ishikawa, T., Wood, J.L., Eds.; International Society for Optics and Photonics (SPIE): Bellingham, WA, USA, 2002; Volume 4782, pp. 12–20. [[CrossRef](#)]
25. Campos, J.; Yaroslavsky, L.P.; Moreno, A.; Yzuel, M.J. Integration in the Fourier domain for restoration of a function from its slope, comparison of four methods. *Opt. Lett.* **2002**, *27*, 1986–1988. [[CrossRef](#)]
26. Moreno, A.; Campos, J.; Yaroslavsky, L. Frequency response of five integration methods to obtain the profile from its slope. *Opt. Eng.* **2005**, *44*, 033604. [[CrossRef](#)]
27. Coleman, E.N.; Jain, R. Obtaining 3-dimensional shape of textured and specular surfaces using four-source photometry. *Comput. Graph. Image Process.* **1982**, *18*, 309–328. [[CrossRef](#)]
28. Healey, G.; Jain, R. *Depth Recovery from Surface Normals*; Center for Robotics and Integrated Manufacturing, Robot Systems Division, University of Michigan: Ann Arbor, MI, USA, 1984.
29. Horn, B.K.P. Height and gradient from shading. *Int. J. Comput. Vis.* **1990**, *5*, 37–75. [[CrossRef](#)]
30. Horn, B.K.; Brooks, M.J. The variational approach to shape from shading. *Comput. Vision Graph. Image Process.* **1986**, *33*, 174–208. [[CrossRef](#)]
31. Welch, W.; Witkin, A. Variational Surface Modeling. *SIGGRAPH Comput. Graph.* **1992**, *26*, 157–166. [[CrossRef](#)]
32. Pernkopf, F. 3D surface acquisition and reconstruction for inspection of raw steel products. *Comput. Ind.* **2005**, *56*, 876–885. [[CrossRef](#)]
33. Usamentiaga, R.; Garcia, D.F.; Molleda, J.; Bulnes, F.G.; Bonet, G. Vibrations in steel strips: Effects on flatness measurement and filtering. In Proceedings of the 2013 IEEE Industry Applications Society Annual Meeting, Lake Buena Vista, FL, USA, 6–11 October 2013; pp. 1–10.
34. Macedo, I.; Gois, J.P.; Velho, L. Hermite Radial Basis Functions Implicits. *Comput. Graph. Forum* **2011**, *30*, 27–42. [[CrossRef](#)]

35. Alonso, M.; Izaguirre, A.; Andonegui, I.; Graña, M. An Application of Laser Measurement to On-Line Metal Strip Flatness Measurement. In Proceedings of the 15th International Conference on Soft Computing Models in Industrial and Environmental Applications (SOCO 2020), Burgos, Spain, 16–18 September 2020; Herrero, A., Cambra, C., Urda, D., Sedano, J., Quintian, H., Corchado, E., Eds.; Springer International Publishing: Cham, Switzerland; pp. 835–842.
36. Amann, M.C.; Bosch, T.; Lescure, M.; Myllylä, R.; Rioux, M. Laser ranging: a critical review of usual techniques for distance measurement. *Opt. Eng.* **2001**, *40*, 10–19.
37. Zhang, G.; He, J.; Li, X. 3D vision inspection for internal surface based on circle structured light. *Sensors Actuators Phys.* **2005**, *122*, 68–75. [[CrossRef](#)]
38. Jarvis, R.A. A Perspective on Range Finding Techniques for Computer Vision. *IEEE Trans. Pattern Anal. Mach. Intell.* **1983**, *PAMI-5*, 122–139. [[CrossRef](#)]
39. Mundy, J.L.; Porter, G.B. A Three-Dimensional Sensor Based on Structured Light. In *Three-Dimensional Machine Vision*; Kanade, T., Ed.; Springer US: Boston, MA, USA, 1987; pp. 3–61. [[CrossRef](#)]
40. Miks, A.; Novak, J.; Novak, P. Analysis of imaging for laser triangulation sensors under Scheimpflug rule. *Opt. Express* **2013**, *21*, 18225–18235. [[CrossRef](#)]
41. Collado, J.F. *New Methods for Triangulation-Based Shape Acquisition using Laser Scanners*; Universitat de Girona: Girona, Spain, 2004.
42. Goodman, J.W. Statistical properties of laser speckle patterns. In *Laser Speckle and Related Phenomena*; Dainty, J.C., Ed.; Springer: Berlin/Heidelberg, Germany, 1975; pp. 9–75. [[CrossRef](#)]
43. Roelandt, S.; Meuret, Y.; Craggs, G.; Verschaffelt, G.; Janssens, P.; Thienpont, H. Standardized speckle measurement method matched to human speckle perception in laser projection systems. *Opt. Express* **2012**, *20*, 8770–8783. [[CrossRef](#)] [[PubMed](#)]
44. Amir, Y.; Thörnberg, B. High Precision Laser Scanning of Metallic Surfaces. *Int. J. Opt.* **2017**, *2017*, 4134205. [[CrossRef](#)]
45. Fisher, R.B.; Naidu, D.K. A Comparison of Algorithms for Subpixel Peak Detection. In *Image Technology: Advances in Image Processing, Multimedia and Machine Vision*; Sanz, J.L.C., Ed.; Springer: Berlin/Heidelberg, Germany, 1996; pp. 385–404. [[CrossRef](#)]
46. Haug, K.; Pritschow, G. Robust laser-stripe sensor for automated weld-seam-tracking in the shipbuilding industry. In *IECON '98, Proceedings of the 24th Annual Conference of the IEEE Industrial Electronics Society (Cat. No.98CH36200)*, Los Alamitos, CA, USA, 31 August–4 September 1998; IEEE: Piscataway, NJ, USA, 1998; Volume 2, pp. 1236–1241.
47. Forest, J.; Salvi, J.; Cabruja, E.; Pous, C. Laser stripe peak detector for 3D scanners. A FIR filter approach. In Proceedings of the 17th International Conference on Pattern Recognition, Cambridge, UK, 26–26 August 2004; Volume 3, pp. 646–649.
48. Schafer, R.W. What Is a Savitzky-Golay Filter? [Lecture Notes]. *IEEE Signal Process. Mag.* **2011**, *28*, 111–117. [[CrossRef](#)]
49. Flesia, A.G.; Ames, G.; Bergues, G.; Canali, L.; Schurrer, C. Sub-pixel straight lines detection for measuring through machine vision. In Proceedings of the 2014 IEEE International Instrumentation and Measurement Technology Conference (I2MTC) Proceedings, Montevideo, Uruguay, 12–15 May 2014; pp. 402–406.
50. Aggarwal, N.; Karl, W.C. Line detection in images through regularized hough transform. *IEEE Trans. Image Process.* **2000**, *15*, 582–591. [[CrossRef](#)]
51. Hagara, M.; Kulla, P. Edge Detection with Sub-pixel Accuracy Based on Approximation of Edge with Erf Function. *Radioengineering* **2011**, *20*, 516–524.
52. Tsai, R. A versatile camera calibration technique for high-accuracy 3D machine vision metrology using off-the-shelf TV cameras and lenses. *IEEE J. Robot. Autom.* **1987**, *3*, 323–344. [[CrossRef](#)]
53. Salvi, J.; Armangué, X.; Batlle, J. A comparative review of camera calibrating methods with accuracy evaluation. *Pattern Recognit.* **2002**, *35*, 1617–1635. [[CrossRef](#)]
54. Bolles, R.C.; Kremers, J.H.; Cain, R.A. *A Simple Sensor to Gather Three-Dimensional Data*; Technical Report; AI Center, SRI International: Menlo Park, CA, USA, 1981.
55. Chen, C.H.; Kak, A.C. Modelling and calibration of a structured light scanner for 3D robot vision. In Proceedings of the IEEE Conference on Robotics and Automation, Raleigh, NC, USA, 31 March–3 April 1987; pp. 807–815.

56. Chiarella, M.; Pietrzak, K.A. An accurate calibration technique for 3-D laser stripe sensors. In *Optics, Illumination, and Image Sensing for Machine Vision IV*; International Society for Optics and Photonics: Bellingham, WA, USA, 1990.
57. Tiddeman, B.; Duffy, N.; Rabey, G.; Lokier, J. Laser-video scanner calibration without the use of a frame store. *IEE Proc. Vision Image Signal Process.* **1998**, *145*, 244–248. [[CrossRef](#)]
58. Huynh, D.Q.; Owens, R.A.; Hartmann, P.E. Calibrating a Structured Light Stripe System: A Novel Approach. *Int. J. Comput. Vis.* **1999**, *33*, 73–86. [[CrossRef](#)]
59. Zhou, F.; Zhang, G. Complete calibration of a structured light stripe vision sensor through planar target of unknown orientations. *Image Vis. Comput.* **2005**, *23*, 59–67. [[CrossRef](#)]
60. Reid, I.D. Projective calibration of a laser-stripe range finder. *Image Vis. Comput.* **1996**, *14*, 659–666. [[CrossRef](#)]
61. DePiero, F.W.; Trivedi, M.M. *3-D Computer Vision Using Structured Light: Design, Calibration, and Implementation Issues*; Elsevier: Amsterdam, The Netherlands, 1996; Volume 43, pp. 243–278. [[CrossRef](#)]
62. Trucco, E.; Fisher, R.B.; Fitzgibbon, A.W.; Naidu, D. Calibration, data consistency and model acquisition with laser strippers. *Int. J. Comput. Integr. Manuf.* **1998**, *11*, 293–310. [[CrossRef](#)]
63. Brajovic, M.; Stankovic, S.; Orovic, I. Analysis of Noisy Coefficients in the Discrete Hermite Transform Domain with Application in Signal Denoising and Sparse Signal Reconstruction. *Signal Process.* **2018**, *150*, 145–156. [[CrossRef](#)]
64. Hughes, J.F.; van Dam, A.; McGuire, M.; Sklar, D.F.; Foley, J.D.; Feiner, S.; Akeley, K. *Computer Graphics: Principles and Practice*, 3rd ed.; Addison-Wesley: Upper Saddle River, NJ, USA, 2013.
65. Jerri, A.J. The Shannon sampling theorem-Its various extensions and applications: A tutorial review. *Proc. IEEE* **1977**, *65*, 1565–1596. [[CrossRef](#)]
66. Conte, S.D.; Boor, C. Differentiation And Integration. In *Elementary Numerical Analysis*; Classics in Applied Mathematics; Society for Industrial and Applied Mathematics: Philadelphia, PA, USA, 2018; Chapter 7, pp. 294–345. [[CrossRef](#)]
67. Weinberg, L.; Slepian, P. Takahasi's Results on Tchebycheff and Butterworth Ladder Networks. *IRE Trans. Circuit Theory* **1960**, *7*, 88–101. [[CrossRef](#)]
68. Oppenheim, A.; Schaffer, R. *Discrete-Time Signal Process*; Pearson Education India: Bangalore, India, 1999.








© 2020 by the authors. Licensee MDPI, Basel, Switzerland. This article is an open access article distributed under the terms and conditions of the Creative Commons Attribution (CC BY) license (<http://creativecommons.org/licenses/by/4.0/>).

6.3. Publication 3: Depth Data Denoising in Optical Laser Based Sensors for Metal Sheet Flatness Measurement: A Deep Learning Approach

6.3 Publication 3: Depth Data Denoising in Optical Laser Based Sensors for Metal Sheet Flatness Measurement: A Deep Learning Approach

Article

Depth Data Denoising in Optical Laser Based Sensors for Metal Sheet Flatness Measurement: A Deep Learning Approach

Marcos Alonso ^{1,2,*} , Daniel Maestro ¹ , Alberto Izaguirre ¹ , Imanol Andonegui ¹  and Manuel Graña ² 

¹ Robotics and Automation Group, Electronic and Computer Science Department, Faculty of Engineering, Mondragon University, Loramendi Kalea, 4, 20500 Arrasate-Mondragon, Spain; dmaestro@mondragon.edu (D.M.); aizaguirre@mondragon.edu (A.I.); iandonegui@mondragon.edu (I.A.)

² Computational Intelligence Group, CCIA Department, UPV/EHU, Paseo Manuel de Lardizabal 1, 20018 San Sebastian, Spain; manuel.grana@ehu.es

* Correspondence: malonson@mondragon.edu

Abstract: Surface flatness assessment is necessary for quality control of metal sheets manufactured from steel coils by roll leveling and cutting. Mechanical-contact-based flatness sensors are being replaced by modern laser-based optical sensors that deliver accurate and dense reconstruction of metal sheet surfaces for flatness index computation. However, the surface range images captured by these optical sensors are corrupted by very specific kinds of noise due to vibrations caused by mechanical processes like degreasing, cleaning, polishing, shearing, and transporting roll systems. Therefore, high-quality flatness optical measurement systems strongly depend on the quality of image denoising methods applied to extract the true surface height image. This paper presents a deep learning architecture for removing these specific kinds of noise from the range images obtained by a laser based range sensor installed in a rolling and shearing line, in order to allow accurate flatness measurements from the clean range images. The proposed convolutional blind residual denoising network (CBRDNet) is composed of a noise estimation module and a noise removal module implemented by specific adaptation of semantic convolutional neural networks. The CBRDNet is validated on both synthetic and real noisy range image data that exhibit the most critical kinds of noise that arise throughout the metal sheet production process. Real data were obtained from a single laser line triangulation flatness sensor installed in a roll leveling and cut to length line. Computational experiments over both synthetic and real datasets clearly demonstrate that CBRDNet achieves superior performance in comparison to traditional 1D and 2D filtering methods, and state-of-the-art CNN-based denoising techniques. The experimental validation results show a reduction in error than can be up to 15% relative to solutions based on traditional 1D and 2D filtering methods and between 10% and 3% relative to the other deep learning denoising architectures recently reported in the literature.

Keywords: laser triangulation; metal sheet flatness measurement; smooth surface reconstruction; depth data denoising; Convolutional Neural Networks; deep learning; residual learning



Citation: Alonso, M.; Maestro D.; Izaguirre, A.; Andonegui, I.; Graña, M. Depth Data Denoising in Optical Laser Based Sensors for Metal Sheet Flatness Measurement: A Deep Learning Approach. *Sensors* **2021**, *21*, 7024. <https://doi.org/10.3390/s21217024>

Academic Editor: Steve Vanlanduit

Received: 17 September 2021

Accepted: 21 October 2021

Published: 23 October 2021

Publisher's Note: MDPI stays neutral with regard to jurisdictional claims in published maps and institutional affiliations.



Copyright: © 2021 by the authors. Licensee MDPI, Basel, Switzerland. This article is an open access article distributed under the terms and conditions of the Creative Commons Attribution (CC BY) license (<https://creativecommons.org/licenses/by/4.0/>).

1. Introduction

Increasingly stringent specifications in terms of flatness and surface quality in the manufacture of sheet metal products are becoming more demanding of real-time 100% quality-control processes. The end customer expects not only excellent mechanical and processing properties but also a high long-term value and a high quality of modern metallic materials. To meet these high expectations, the steel industry needs intelligent quality-control systems endowed with high-precision in-line sensors for real-time measurements.

In the manufacture of parts and assemblies, especially when parts are required to be assembled over a surface, flatness is a critical specification requirement. Any flatness defect will cause an undesirable optical effect and impact the overall appearance of the assembly. This need for zero defect manufacturing arises in areas as varied as the manufacture of

stainless steel sheets used in professional kitchens, metal panels for exterior decoration in architectural projects, or the manufacture of aluminum sheets in the automotive industry. For this reason, it is highly desirable to carry out a quality control in real time during the metal sheet manufacturing covering 100% of its surface in order to ensure that the required industry quality standards are met.

With the advances in computer vision technology, optical flatness sensors have become widespread [1] allowing manufacturing line human operators to measure manifest flatness, i.e., flatness not hidden by tension, at high line speeds, thus enabling real-time monitoring as well as a high degree of automation in the production phase. Most optical surface flatness inspection systems used in the metal sheet industry are based on the laser triangulation principle [2–4].

The large real-time inspection capabilities of these optical sensors are impeded by the non-linear high-frequency fluctuations induced in the steel sheet surface by the mechanical processes that take place in the manufacturing line, the juddering of the metal strip due to forward traction, as well as the shearing processes that cut to length the sheet. Under these circumstances, achieving a highly accurate flatness measurement requires a high performance signal denoising method to be applied to the height profile captured by the 3D sensor, removing the noise corresponding to such non-linear high-frequency fluctuations. The literature [5–11] presents different sensors based on laser triangulation, requiring the use of two or more laser lines to filter out external noise sources and reconstruct an accurate and smooth continuous 3D map of the metal sheet surface.

The main contribution of this paper is a novel deep learning architecture for the reconstruction of the range image captured by the 3D sensor removing the high-frequency noise due to mechanical processes in order to allow accurate flatness measurements for quality control. This deep learning architecture is inspired in the U-Net [12], originally developed for semantic segmentation. Instead of returning as output an decomposition of the image into regions, our architecture returns the noise-free range image by using a noise estimation module. The architecture is validated against synthetic and real range images that exhibit the most significant noise modalities produced by the mechanical processing induced vibrations on the steel sheet surface. Real data have been collected from an industrial roll leveling and cut-to-length line where the developed 3D sensor is installed. Moreover, the architecture is compared against image denoising deep learning architectures reported in the literature. To this end, we have retrained these architectures with our data from scratch.

The remainder of this paper is organized as follows: Section 2 reviews the industrial context regarding techniques and devices used to measure metal sheets flatness. Section 3 describes our noise model for the generation of synthetic data. Section 4 reviews computational approaches for image denoising, setting the stage for our proposal. Sections 5 and 6 present the proposed deep learning architecture for range image denoising and the collected Dataset, respectively. Section 7 reports the experimental results. Finally, Section 8 gives our conclusions and directions of future work.

2. Industrial Context

In order to inspect rolled products achieving accurate measurements and classification of flatness defects, it is necessary to capture the geometry of the steel sheet as it moves through the processing line. With sheet feeding rates reaching speeds of up to 120 m/min, real-time inspection imposes very strict requirements for accurate surface flatness quality control. The most typical flatness defects are wavy edges, centre buckles, and bow defects, which appear as low-frequency variations in the metal strip surface height.

On account of the strict requirements for real time quality control of surface flatness, the time efficiency of noise filtering methods poses a major challenge. Most of the literature [7,9,11] addresses this problem relying on the use of traditional filtering methods or explicit noise modeling, requiring extensive fine-tuning to adequately adapt to different noise levels, struggling in preserving details, and leading to local (sensor-specific) solutions.

Several successful applications of machine learning and fuzzy systems modeling for the detection of surface defects in flat steel products can be found in the literature [13–15], but they do not extend to the categorization of flatness defects. There are even machine learning approaches to link different types of defects with their causes [16,17].

Contrary to traditional hand crafted filtering methods, Convolutional Neural Networks (CNNs) are tuned by automated learning techniques guided by error minimization carried out by stochastic gradient descent and backpropagation algorithm. They have improved sensor data interpretation, analysis and control algorithms, being capable of dealing with non-linearities, noise, and uncertainty. In this regard, CNNs have become the state-of-the-art machine learning approach in many applications [18–22]. Recently, CNNs have been applied to classify surface defects in cold-rolled strips [23], and flatness measure prediction [24] from measurements of contact sensors attached to the roll mill instead of optical or range images of the surface. In order to adapt their 1D data from the sensor readings they fold these vectors into small images (5×8 or 20×20) which are the input for the CNNs, following the convention that CNNs are image classifiers or regressors. Note that the goal in [24] is the prediction of an overall measure of flatness from linear sensor readings.

However, to the best of the authors knowledge, there are no studies yet on CNN or other deep-learning-based methods to filter data obtained from optical flatness sensors in order to accurately reconstruct the surface of metal strips. In this regard, we are specifically interested in assessing the denoising performance of deep learning architectures when the input range image data contain high levels of non-linear noise.

Actual Sensor Installation

The flatness data were acquired with a simplified version of the optical flatness sensor described in [10]. The flatness sensor is comprised of a single illuminating linear laser source perpendicular to the metal sheet translation axis and a CCD camera capturing the area illuminated by the laser. In this simplified sensor version, the baseline separation between camera and the laser source is $\Delta_B = 900$ mm, and the triangulation angle is $\alpha = 45^\circ$ so that the center of the camera captures the middle of the laser line at $Z = 0$ mm. The laser line emitter is collimated, and its wavelength is $\lambda = 450$ nm, while its line aperture is 90° . The camera features a 2048×2048 matrix CCD sensor, and the focal length of the lens is $f = 6$ mm, placed at $Z = 1140$ mm over a moving steel strip. Figure 1 shows the scheme of the sensor.

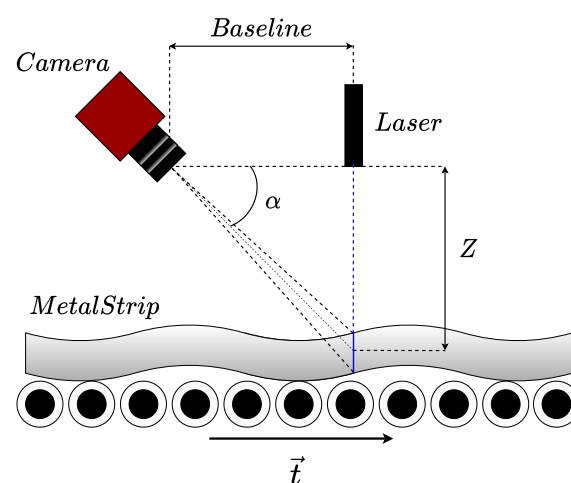


Figure 1. The flatness sensor scheme used for data acquisition, consisting of a single laser line laser triangulation scheme.

Figure 2 shows the scheme of the production line and the placement of the optical flatness sensor. Steel coils which are reduced to a specific thicknesses by rolling and

annealing and wound into a roll. These steel coils are further processed in a roll leveling and shearing line where they are cut to length. The range sensor was placed before the cutting tool, so the steel sheet surface propagates the vibrations induced by the cutting shocks. Each type of steel coil possesses different mechanical properties and thickness. As a result, they exhibit different propagation responses to the vibrations induced in the metal sheet during the leveling and cutting processes. This fact adds variability and robustness requirements to the proposed network.

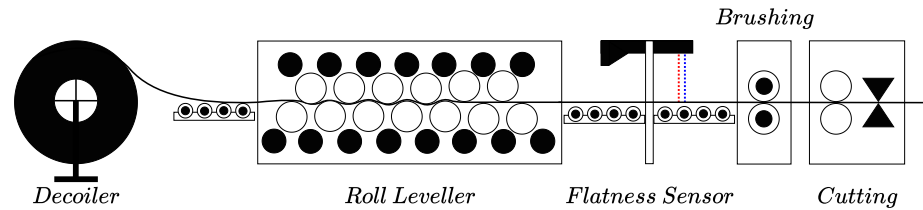


Figure 2. The experimental production line scheme and the optical flatness sensor placement. Blue and Red lines refer to laser planes used for pseudo-groundtruth calculation in real data experiments. Blue line refers to the laser plane which is further used for training, validation, and testing the proposed CBRDNet.

3. Noise Model for Synthetic Data Generation

Generating physically consistent surface data are crucial to train the proposed CBRDNet and increase its denoising generalization capability. However, modeling such metal surfaces is impeded by the lack of accurate experimental data. Custom metrology devices, such as coordinate measuring machines (CMM), rely on static measuring conditions and, thus, fail to retrieve the most characteristic surface deformation caused by the tensile and trachle stresses occurring at the metal strip roll leveling and cut to length processes. To cope with this lack of data, our synthetic samples rely on a model of experimentally reconstructed surface data shown in [10], which reproduce the most common defects in a roll leveler processing line, as well as the coupling noise produced by mechanical elements, such as cutting stage.

We model the range image captured by our sensor from metal surface data by a function that combines a high-frequency and high-amplitude bump produced by the cutting stage, modeled as a local Gaussian signal $\psi(x, y)$, a superposition of a set of stationary waves $\varphi(x, y)$, a low-frequency carrier $\theta(y)$ and a Gaussian noise term $\rho(x, y)$ modeling the data acquisition electronics error,

$$S(x, y) = \varphi(x, y) + \psi(x, y) + \theta(y) + \rho(x, y) \quad (1)$$

where

$$\begin{aligned} \varphi(x, y) = & \sum_{n=0}^N \sum_{m=0}^M \alpha_{n,m} \cos\left(\frac{2\pi nx}{\lambda_x}\right) \cos\left(\frac{2\pi my}{\lambda_y}\right) \\ & + \sum_{n=0}^N \sum_{m=0}^M \beta_{n,m} \cos\left(\frac{2\pi nx}{\lambda_x}\right) \sin\left(\frac{2\pi my}{\lambda_y}\right) \\ & + \sum_{n=0}^N \sum_{m=0}^M \gamma_{n,m} \sin\left(\frac{2\pi nx}{\lambda_x}\right) \cos\left(\frac{2\pi my}{\lambda_y}\right) \\ & + \sum_{n=0}^N \sum_{m=0}^M \delta_{n,m} \sin\left(\frac{2\pi nx}{\lambda_x}\right) \sin\left(\frac{2\pi my}{\lambda_y}\right) \end{aligned} \quad (2)$$

is a real-valued 2D Fourier series, where the amplitudes $\alpha = \delta = [0, 5]$ and $\beta = \gamma = 0$. $\lambda_x = \lambda_y = [0, 0.1]$ are the wavelengths in the x and y directions,

$$\psi(x, y) = \frac{\sin(f_b y A_b)}{1 + 4 \left[\frac{(y - y_0)}{L_b} \right]^2} \quad (3)$$

is a high-frequency, high-amplitude Gaussian wave mixed with a low-frequency carrier modeling the bump produced by the cutting device, where $f_b = 5$ represents the bump carrier frequency, $A_b = [1, 3]$ stands for the bump amplitude, $L_b = [10, 20]$ is the bump wave attenuation, and

$$\theta(y) = A_c \cos(K_c y) \quad (4)$$

is a low-frequency carrier that sets the offset of the surface data along the transversal y -direction, where $A_c = [0, 0.5]$ is the carrier amplitude and $K_c = [0, 0.1]$ represents the frequency in the y direction. Finally, $\rho(x, y)$ is the electronic noise that arises during data acquisition caused by the discrete nature of radiation, i.e., the fact that the optical sensor captures an image by collecting photons. Considering some assumptions, this noise can be approximated by an additive model in which the noise has a zero-mean Gaussian distribution determined by its variance $\sigma_n^2 = [0.1, 0.35]$. That is, each value in the noisy data is the sum of the real value and a random, Gaussian distributed noise value. The defined intervals of variation and constant values for these variables have been selected in order to obtain synthetic data that are as close as possible to that acquired by the sensor in real experiments. We disregarded strict boundary conditions, such as Dirichlet conditions due to the free form nature of the unrolled metal coils on the machine. A synthetic surface generated using this model is shown in Figure 3.

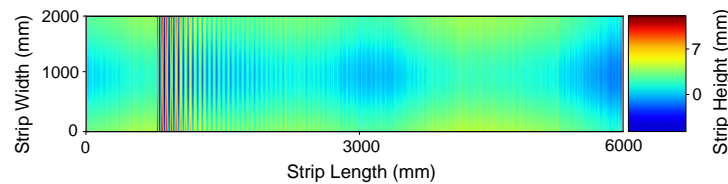


Figure 3. Synthetic flatness sensor data. (Color Online).

As shown in Figure 3, the proposed noise model allows us to generate synthetic data that are very similar to that acquired by the sensor in real experiments. The degree of concordance between our model and experimental data have been qualitatively validated by visual inspection. We cannot tune the model quantitatively because the noise source is not observable. We cannot observe the noise separated from the actual metal sheet surface, and the wave propagation and dumping properties are dependent of the actual metal sheet mechanical properties. We postulate that the success of the denoising system trained on the synthetic data are indirect proof of the validity of the model.

4. Deep Learning Denoising Approaches

An autoencoder is an unsupervised neural network architecture that is trained to reproduce the input as its output. It has a typical structure as a pair of funnels attached by the short end. The first funnel compresses the input data into a lower-dimension encoding, while the second funnel decompresses the encoding trying to recover the original input data. The encoder seeks to obtain a robust latent representation of the original data, which is often used for other purposes, such as features for another classification module. Autoencoders have been a popular field of study in neural networks in recent decades. The first applications of this type of neural networks date back to the 1980s [25–27]. Autoencoders have been used for classification, clustering, anomaly detection, dimensionality reduction, and signal denoising [28].

Proposed by Vincent et al. [29], the Denoising Autoencoders (DAEs) are an extension of classic autoencoders where the model is taught to predict original uncorrupted data from corrupted input data, i.e., the decoder attempts to reconstruct a clean version of the corrupted input from the autoencoder latent representation.

The encoder function f takes an input $\tilde{\mathbf{x}}$ and maps it to a hidden representation \mathbf{y} computed as:

$$\mathbf{y} = f_{\theta}(\tilde{\mathbf{x}}) = h(\mathbf{W}\tilde{\mathbf{x}} + \mathbf{b}) \quad (5)$$

where h is a typically nonlinear transfer function, \mathbf{W} and \mathbf{b} are the encoder network parameters, and $\theta = (\mathbf{W}, \mathbf{b})$.

The output \mathbf{x} , having a similar form to $\tilde{\mathbf{x}}$, is reconstructed from \mathbf{y} by the decoder g

$$\mathbf{x} = g_{\theta'}(\mathbf{y}) = h'(\mathbf{W}'\mathbf{y} + \mathbf{b}') \quad (6)$$

where h' is similar to h , \mathbf{W}' and \mathbf{b}' are the decoder network parameters, and $\theta' = (\mathbf{W}', \mathbf{b}')$.

The DAE training procedure consists on learning the parameters \mathbf{W} , \mathbf{W}' , \mathbf{b} , and \mathbf{b}' that minimise the autoencoder reconstruction error between the groundtruth \mathbf{x} and the reconstruction $g_{\theta'}(f_{\theta}(\tilde{\mathbf{x}}))$, using a suitable cost function. Typically, the function is minimised using Stochastic Gradient Descent (SGD) [30] for small batches of corrupted and clean sample pairs.

Convolutional Denoising Autoencoders (CDAEs) are Denoising Autoencoders implemented using convolutional encoding and decoding layers. Because CDAEs use CNNs for extracting high-order features from images, CDAEs differ from standard DAEs in that their parameters are shared across all input image patches to maintain spatial locality. Different studies show that CDAEs achieve better image processing performance when compared to standard DAEs [31,32].

The U-Net [12] has an encoding–decoding architecture inspired in the autoencoder with skip connections [33] that transfer the data from the encoder layers to the decoding layers. Input–output pairs are images and their desired semantic pixel labelling providing segmentation of the image in one shot. It has shown exceptional results for image segmentation and image restoration tasks [34–36]. Depending on the architectural modifications made to U-Net, it can be used to achieve different tasks beyond segmentation. Isola et al. [37] used U-Net as a generator to perform image-to-image translation tasks such as in the case of aerial images and their correspondence in maps or the conversion of gray-scale images to color images through adversarial learning. Jansson et al. [38] investigated the use of U-Net as a voice separator, using the magnitude of the spectrogram of the audio containing the mix of different singing voices as the input. Zhang et al. [39] modified U-Net with a residual block and proposed it as a tool for extracting roads from aerial maps.

State-of-the-art 2D deep learning image denoising methods that will be compared with our proposal are CBDNet [40], NERNet [41], BRDNet [42], FFDNet [43], and CD-nCNN_B [44]. CBDNet is a convolutional blind denoising network [40] that is composed of a noise estimation module and a non-blind denoising module that accepts the noise estimation to compute the clean image. The noise estimation module is a CNN without pooling (i.e., no dimension reduction), while the denoising module is a U-shaped network as discussed above. The work reported in [40] uses a realistic noise model that includes in-camera processing to generate synthetic images with known noise component for network training. The noise estimation and removal network NERNet [41] inherits the two module structure of CBDNet. The noise estimation module is enriched with a pyramidal feature fusion block that provides multi-scale noise estimation, while the CNN components are dilated convolutions. The noise removal module is U-shaped using dense convolution and dilation selective blocks. The synthetic images were generated adding white Gaussian noise (AWGN). In the batch renormalization denoising network BRDNet [42], the batch renormalization is claimed to address the internal covariate shift and small mini-batch problems. The network is composed of upper and lower networks. Upper network is composed of residual learning modules with batch renormalization, while the lower net-

work includes also dilated convolution blocks. Contrary to the previous networks, no explicit noise estimation module is designed. Noise is assumed to be AWGN. The fast and flexible denoising network FFDNet [43] is also designed for cleaning AWGN corrupted images. FFDNet is a CNN whose inputs are downsampled subimages and a noise level map, it does not have a module to estimate the noise. The denoising convolutional neural network (DnCNNs) [44] is able to handle Gaussian denoising with unknown noise level. The DnCNN uses residual learning in order to estimate the noise component of the image, which is later removed from the noisy image to obtain the clean image.

5. Proposed Deep Learning Image Denoising Architecture

We apply of U-Net architecture as a generalized denoising method for surface reconstruction from noisy range images. The proposed network should be capable of denoising the degraded range images as an alternative to traditional image denoising techniques like spatial filtering, transform domain filtering, or wavelet thresholding methods [45]. A denoising method should remove high- and low-frequency noises, reconstructing the original surface. Results presented in the literature show that CNNs outperform traditional techniques for denoising tasks [46,47]. Furthermore, once trained, CNNs are computationally very efficient as they may be run on high-performance graphic processing units (GPUs) [48,49].

Our study proposes a convolutional blind residual denoising network model (CBRDNet) based on the U-Net architecture for denoising flatness sensor data. Since in real-world scenarios only noisy input data are provided, correct estimation of the noise level has proven to be challenging [40]. Therefore, incorporating a noise estimation block, can enhance the network generalization capabilities as shown by Lan et al. [50] and Guo et al. [41]. Besides that, the combination of both synthetic and real noisy data in the model training is expected to improve the network's denoising efficiency [51].

The structure and denoising functionality of the proposed network are described within the following sub-section.

5.1. Network Architecture

The proposed CBRDNet architecture consists of mainly two stages, a blind residual noise estimation subnetwork (NE-SNet) and a noise removal subnetwork (NR-SNet). The overall scheme of the proposed network is shown in Figure 4

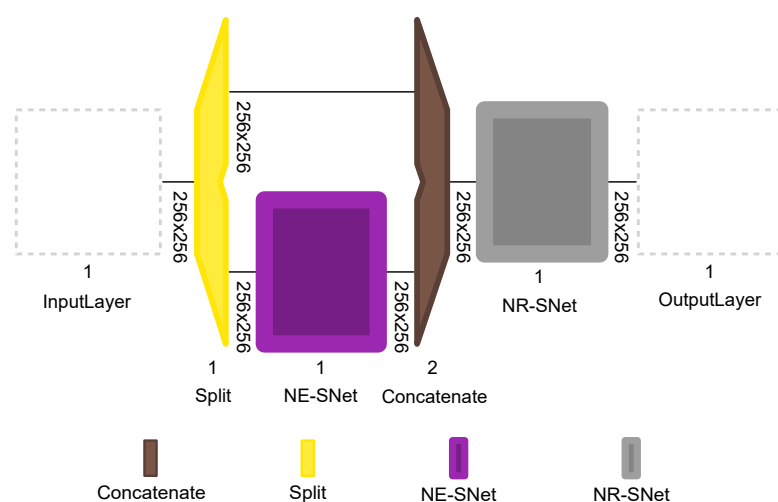


Figure 4. Overall scheme of the proposed CBRDNet network for close to real-time flatness data denoising.

The NE-SNet subnetwork takes a noisy observation and produces an estimated noise level map. It is composed of residual learning blocks that were first proposed as part of the ResNet architecture [52]. The layers of this subnetwork will increasingly separate image

structure from noise, creating a noise map that will be used later in the denoising stage. The NE-SNet is composed of five residual blocks with no pooling, each of which has two convolutional (Conv2D) layers with Batch Normalization (BN) and Rectified Linear Unit (ReLU) layers. The number of feature channels in each Conv2D layer is set to 64, and the filter size is set to 3×3 . The scheme of the NE-SNet subnetwork is shown in Figure 5.

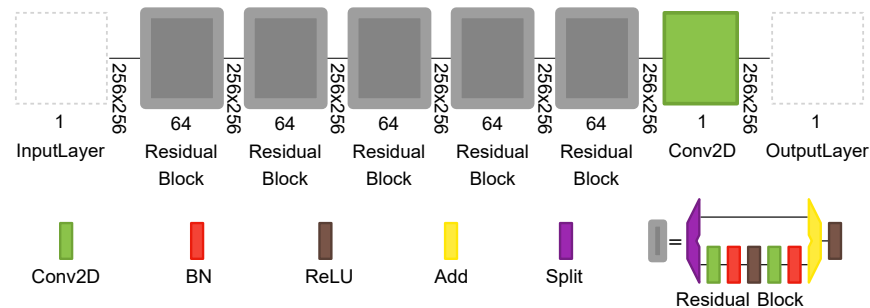


Figure 5. The proposed Noise Estimation Subnetwork NE-SNet composed of residual learning blocks.

The NR-SNet subnetwork is based on a traditional U-Net. This subnetwork is divided into two major paths: contracting (encoder) and expanding (decoder). The contracting path is comprised of downsampling layers consisting of a MaxPooling2D layer and two Conv2D layers with a filter size of 3×3 and “same” padding configuration. Each contracting block halves the size of feature maps and doubles the number of feature channels, starting with 64 channels in the first stage and ending with 512 channels in the last. The bottleneck connects both the expanding path and the contracting path; herein, the data has been resized to $32 \times 32 \times 512$. Similarly, the expanding path also comprises four upsampling blocks, which are composed of two Conv2D layers followed by a Conv2D Transpose. Each expanding block doubles the size of feature maps and halves the number of feature channels. We used concatenation layers to merge the feature maps in the expanding path with the corresponding feature maps in the contracting path. The last layer is a 1×1 Conv2D. The original U-Net architecture for image segmentation uses a sigmoid activation function in this last layer. Instead, our proposed architecture uses a linear activation function in order to recover the denoised image. The scheme of the NR-SNet subnetwork is given in Figure 6.

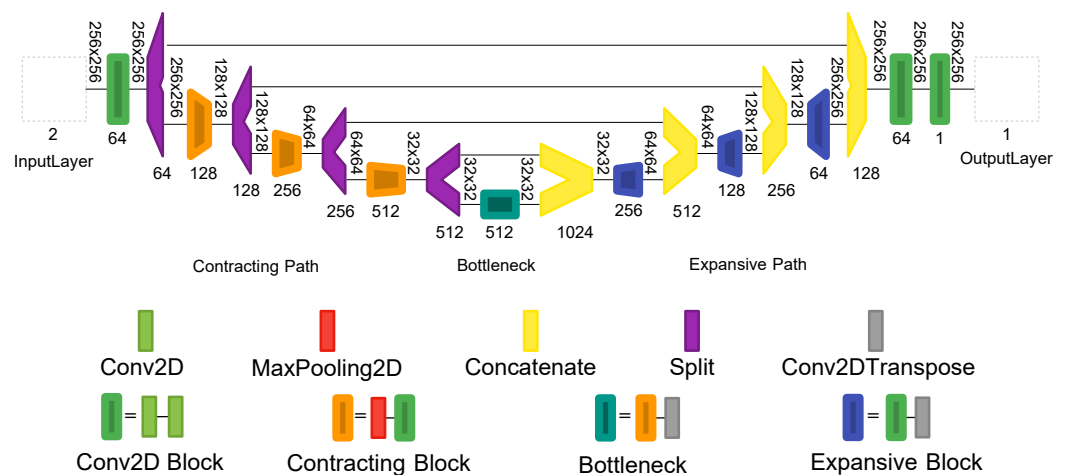


Figure 6. The proposed Noise Removal Subnetwork NR-SNet following a U-net architecture.

5.2. Training the Model

Given a 3D dataset encompassing data recovered from the laser based optical flatness sensor and synthetic 3D data described in Section 6, we generate a set of depth images,

which are decomposed into patches for processing. Using this dataset of local patches, we train our network to reconstruct the denoised versions of input depth images. In order to train the CBRDNet, we use the ADAM [53] algorithm with $\beta = 0.9$. Following most CNN-based data denoising methods, our network adopts the mean squared error (MSE) as the loss function and the initialization strategy of He [54]. The mini-batch size is 10, and each patch size is 256×256 pixels. The mini-batch size has been selected as a trade-off between our limited computational capabilities and the desired network generalization performance. Experimental results demonstrate that small batch sizes with small learning rates result in more reliable and stable training, better generalization performance, and a much lower memory footprint [55,56]. The model is trained for 100 epochs, with the learning rate for the first 20 epochs set to 10^{-3} and the learning rate 10^{-4} used to fine-tune the model. These settings are the same for all experiments discussed in this paper for uniformity. Besides that, both ReLU and LeakyReLU [57] have been tested as output layer activation functions in the CBRDNet training, the obtained results were almost identical and are shown in Section 7. We trained all the networks in this paper on a single NVIDIA® GeForce® RTX 2080 Super GPU with an on-board frame buffer memory of 8GB GDDR6, 3072 CUDA® Cores operating at 1815 MHz, compute capability 7.5, and Turing Generation microarchitecture, CUDA® 10.1 and CUDNN 7.6.1). The machine is equipped with an Intel® Core i9-10900K CPU @ 3.70GHz processor with 10 cores and 32 GB of RAM.

6. Dataset

The dataset used for both training and testing of the proposed architecture is composed of real production line and synthetic range image samples of steel coils from a roll levelling and shearing line. The synthetic data are used as a kind of data augmentation aiming to improve the network denoising performance because of the difficulties faced collecting a real dataset comprising a wide range of representative samples. Additionally, in real-world measurements the metal sheet is not free from tensile stresses during the manufacturing processes causing its elongation. After cutting the metal strip in single smaller sheets, the tensile stress release results in surface deformations. Thus, measurements obtained by an offline precision measuring device like a coordinate measuring machine (CMM) cannot be used as a validation ground truth for online measurement methods, whereas synthetic samples do.

In this paper, we generate 5500 synthetic noisy data samples using the noise model described in Section 3 together with 5500 real noisy samples from six different coils which are described in Section 6.1. The dataset is divided into a training set (80%), a validation set (10%) and a test set (10%).

6.1. Real Production Line Data

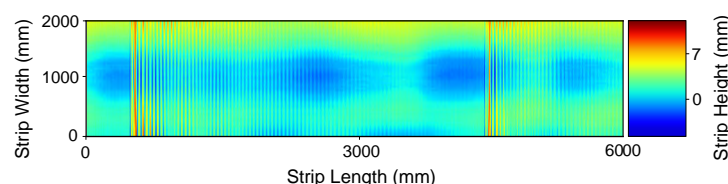
The experimental data coming from the real production line consists of 5500 samples from six different steel coils.

The specifications of the six steel coils are as follows: Two S235JR coils, a carbon (non-alloy) steel formulated for primary forming into wrought products with thicknesses of 3 mm, 8 mm and 1200 mm width, respectively, Young modulus $E = 205$ GPa, Poisson ratio $\mu = 0.301$, yield stress $\sigma = 215$ MPa, annealed and skin passed. One S420ML coil, a special structural steel with a thickness of 7 mm and 2000 mm width, Young modulus $E = 190$ GPa, Poisson ratio $\mu = 0.29$, yield stress $\sigma = 410$ MPa, it is an iron alloy steel manufactured by rolling. One S355M coil, an alloy steel formulated for primary forming into wrought products with a thickness of 3 mm and 1500 mm width, Young modulus $E = 190$ GPa, Poisson ratio $\mu = 0.29$, yield stress $\sigma = 360$ MPa, a middle carbon steel manufactured by rolling, annealing and skin passing. Two S500MC coils, a hot-rolled, high-strength low-alloy (HSLA) with excellent engineering bending and cutting characteristics with a thickness of 3 mm, 6 mm and 2200 mm width, respectively, Young modulus $E = 210$ GPa, Poisson ratio $\mu = 0.304$, yield stress $\sigma = 500$ MPa, produced through thermomechanical rolling. A summary is given in Table 1.

Table 1. Steel coils used for collecting real data and their specifications.

Coil	w × h (mm)	Young (GPa)	Poisson	Yield Stress (MPa)
S235JR	1050 × 3	205	0.301	215
S235JR	2000 × 8	205	0.301	215
S420ML	1650 × 7	190	0.290	410
S355M	1500 × 3	190	0.290	360
S500MC	1050 × 3	210	0.304	500
S500MC	1850 × 6	210	0.304	500

The coils are roughly 800 m long. In each measurement cycle, the optical flatness system senses 9000 mm. High-amplitude disruptive noises from the cutting station, as well as the mechanical processes carried out during the manufacturing greatly contaminate the flatness information generating noisy ripples on the metal strip sensor data. Additionally, the conveyor system generates high-frequency waves as a result of the metal strip advance. This interference patterns result in a complex spatial waveform, causing flatness information and surface defects difficult to detect. A raw depth data sample from one of these steel coils, captured by the optical flatness sensor, is visualised in Figure 7.

**Figure 7.** Raw optical flatness sensor data. (Color online).

7. Results

In this section, we assess the proposed CBRDNet for denoising both synthetic sheet samples and real data from the 3D flatness sensor. The proposed denoising network is employed to reconstruct both simulated and real data in order to test its ability to remove non-linear noises caused by mechanical manipulation of the metal sheet during the manufacturing process.

The metal sheet's flatness corresponds to its levelness when it is tension free. The I-Unit [58] is widely used as the standardized measurement unit of flatness. For the I-Unit calculation in a metal sheet with a sinusoidal surface, a series of virtual lines are drawn to model the surface profile. The I-Unit is computed over them and the reported flatness is the average over all lines. For this reason we compare our 2D methods with 1D denoising methods. We recall that the aim of the present work is to provide a CNN-based denoising method to be applied to range images obtained by optical sensors installed in metal sheet leveling and shearing production lines. The denoised surface range data will be used to carry out the necessary flatness measurement. Accordingly, the results provided below compare the denoised synthetic sheet samples and real ones with its corresponding groundtruth. The error measurements are expressed in millimeters.

7.1. Synthetic Data Results

We conducted three different comparative analyses. First, we apply some traditional 1D filtering methods such as Moving Average, Butterworth IIR [59,60], Savitzky-Golay FIR [61,62], Chebyshev Type II [63], and piecewise cubic Hermite interpolation [10] filters. Secondly, we apply 2D wavelet-based denoising methods. Specifically, we compute results using Daubechies, Symlets, Meyer, Coiflets, and Fejer-Korovkin wavelets [64–66]. Finally, we compare the performance of CBRDNet against some state-of-art 2D deep learning image denosing methods, specifically NERNet [41], CBDNet [40], BRDNet [42], FFDNet [43], and CDnCNN_B [44]. Instances of synthetic data denoising results are shown in Figures 8 and 9, where (a) is the noise-free sample, (b) is the noisy surface data and, finally, (c) is the denoised surface estimated using our method.

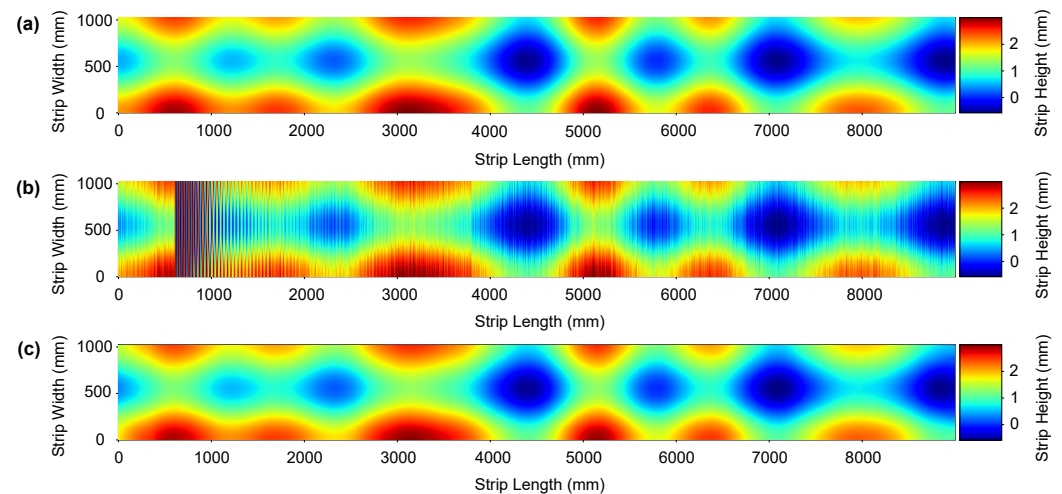


Figure 8. An instance of the denoising result on a synthetic strip. (a) Depicts the noise-free ground truth surface, (b) shows the noise corrupted surface, and (c) represents the denoised surface reconstructed using the proposed network. (Color online).

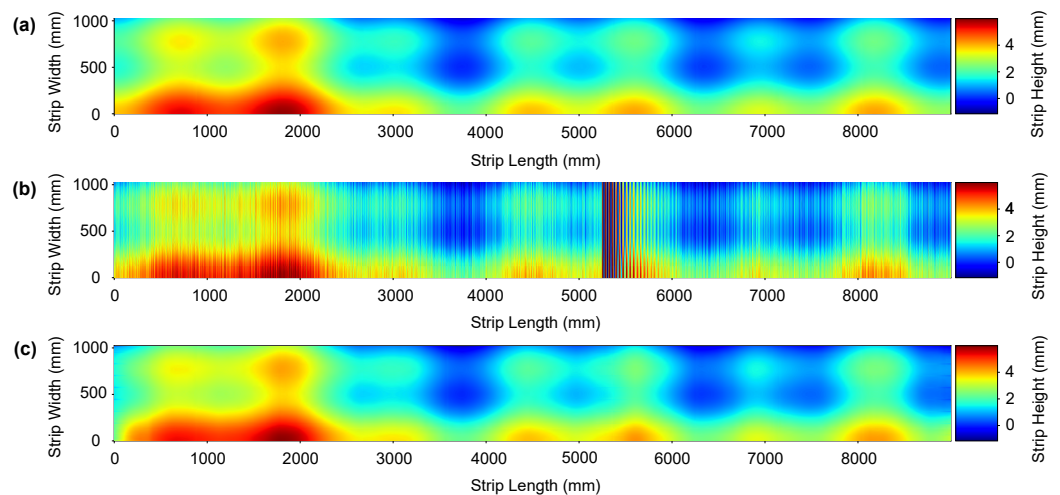


Figure 9. An instance of the denoising result on a synthetic strip. (a) Depicts the noise-free ground truth surface, (b) shows the noise corrupted surface, and (c) represents the denoised surface reconstructed using the proposed network. (Color online).

For the comparative analysis with traditional 1D filtering methods we divided the resulting metal sheet surface in virtual longitudinal strips, also called fibers [58,67]. For each fiber, we applied the following 1D denoising approaches:

A Butterworth IIR filter. This filter provides the optimum balance of attenuation and phase response. It has no rippling effect in the passband or stopband, and as a result, it is frequently referred to as a maximally flat filter. The Butterworth filter provides flatness at the cost of a somewhat broad transition area from passband to stopband, with typical transitory characteristics. It has the following characteristics: a smooth monotonic response (no ripple), it has the slowest roll-off for equivalent order filters, and a more linear passband phase response than other methods. A Butterworth IIR third-order digital filter with a cutoff frequency of 6 dB below the passband value of 0.01 specified in normalized frequency units is used.

A Savitzky-Golay FIR smoothing filter, which is a variation of the FIR average filter that can effectively retain the targeted signal's high-frequency content while still not eliminating as much noise as a FIR average. Savitzky-Golay filters maintain various moment orders better than other smoothing approaches, which generally retain peak widths and heights. It has the following characteristics: a computation time proportional to window width,

it preserves the area, position and width of peaks, and flattens peaks less than moving average with same window width. A third-order Savitzky-Golay FIR smoothing filter with a frame length of 99 samples is used in our experiments.

A Moving Average filter was also applied, which is a method used to smooth data by calculating a series of averages of different subsets of the entire dataset. It is a form of finite impulse response filter with the following characteristics: an optimal approach for reducing random noise while retaining a sharp step response, in general term is a good smoother filter, conceptually it is the simplest to implement, but on the contrary has a poor low-pass filter (frequency domain) and a slow roll-off and terrible stopband attenuation characteristics. A moving-average filter with a 33-sample-long sliding window is used for the comparison experiments.

A Chebyshev Type II filter has been applied. This filter is also known as an inverse filter, it does not roll off and has no ripple in the passband, but it has equiripple in the stopband. The main characteristics of this filter are: it is maximally flat in the passband and has a faster roll-off than Butterworth but slower roll-off than Chebyshev Type I. We used a third-order low-pass Chebyshev Type II filter with a stopband attenuation of 33 dB and a stopband edge frequency of 0.02 specified in normalised frequency units.

Finally, a piecewise cubic Hermite interpolation filter has been used. This filter uses both the height surface information and its derivative calculated from a dual laser sensor data series. It is continuous in shape and its derivative. In comparison to the Savitzky-Golay, Butterworth, Chebyshev, and Average Mean filters used for surface reconstruction in [10], this method achieved a 41 percent improvement.

Because we have the ground truth surface, we can compute the error of our denoising process. Table 2 shows the comparative results of the denoising approaches described above when applied to the synthetic surface. MAE improvements achieved by our method range from three times better when compared to the Hermite filtering approach to 6 times better when compared to the Chebyshev filter approach. Similar improvements are achieved in term of RMSE.

In addition, we conducted 2D wavelet-based denoising methods. The number of vanishing moments N and the denoising threshold are the metaparameters for this approach. According to the current research, disregarding the computational cost of the wavelet transform (WT), higher vanishing moments would yield better performance [68,69]. We selected the following wavelets: Daubechies (dbN), $N = 4$, Symlets ($symN$) $N = 8$, Meyer ($dmey$), Coiflets ($coifN$), $N = 4$, and Fejer-Korovkin (fkN), $N = 4$. We performed the WT of data samples up to 8 levels. For denoising, wavelet transform coefficients below an empirically selected WT threshold are set to zero. An inverse wavelet transform is used after that to transform the processed signal back to the original spatial domain. Because the wavelet coefficients are affected by values outside the extent of the signal under consideration, to avoid boundary effects, the first and last 4 samples were removed in the processed input data. Table 2 shows the comparative results. MAE improvements achieved by our method range from 2.5 times better when compared to the Fejer-Korovkin filtering approach to 1.3 times better when compared to the Symlets filter approach. Similar improvements are achieved in term of RMSE. For a graphical representation of these results, we provide the denoising results on five data samples in Figure 10.

Table 2. Comparative results of our approach with both traditional 1D and 2D denoising approaches and 2D denoising CNN methods. MAE = mean absolute error; MaxAE = maximum absolute error; STD = standard deviation of the absolute error; RMSE = root mean squared error. Best results presented in bold font.

Method	CNN-2D/1D/2D	Blind/Non Blind	MAE *	MaxAE *	STD *	RMSE *
CBRDNet-ReLu (ours)	CNN-2D	Blind	0.140	0.376	0.136	0.147
CBRDNet-LeakyReLu (ours)	CNN-2D	Blind	0.160	0.466	0.154	0.172
CBDNet	CNN-2D	Blind	0.172	0.520	0.162	0.185
NERNet	CNN-2D	Blind	0.184	0.499	0.175	0.195
BRDNet	CNN-2D	Blind	0.198	0.659	0.184	0.212
FFDNet	CNN-2D	Non Blind	0.224	0.501	0.201	0.252
CDnCNN_B	CNN-2D	Blind	0.312	0.840	0.308	0.342
Sym8	2D	NA	0.176	0.543	0.170	0.188
Coif4	2D	NA	0.180	0.591	0.179	0.190
Db8	2D	NA	0.181	0.622	0.179	0.201
Dmey	2D	NA	0.256	0.942	0.282	0.291
Fk8	2D	NA	0.390	1.998	0.588	0.390
Hermite	1D	NA	0.413	1.150	0.380	0.459
Butterworth	1D	NA	0.760	4.423	0.735	0.781
Savitzky-Golay	1D	NA	0.842	6.436	0.779	0.853
Moving Average	1D	NA	0.801	5.463	0.928	0.865
Chebyshev Type II	1D	NA	0.828	5.040	0.828	0.903

* Measurements are expressed in millimeters (mm).

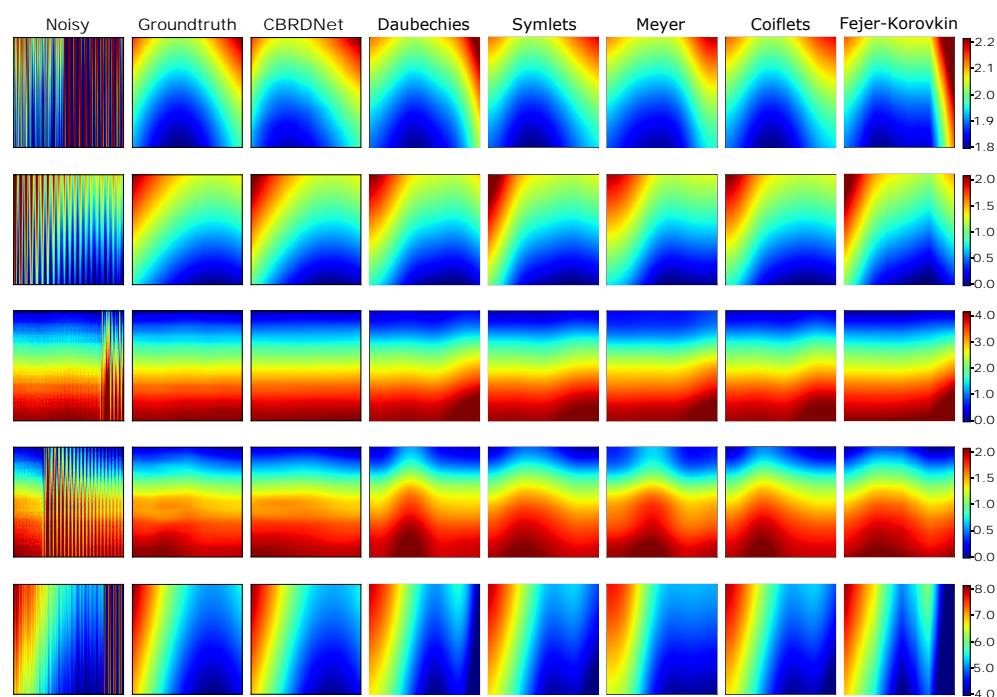


Figure 10. Comparison of our proposed CBRDNet with 2D wavelet-based denoising techniques. Noisy synthetic samples have very low SNR, hence the the groundtruth surface of the samples is almost lostt in some samples. To facilitate the comparison with the denoised samples, the color scale of the images corresponding to the first column, i.e., noisy sample, is clipped. Color scale values are expressed in millimeters (mm). (Color online).

Finally, we compared the architecture presented in this article to the five earlier stated CNN-based approaches. Comparing various deep learning algorithms is a challenging task because of the large number of hyperparameters that must be appropriately tuned during the network training process. Notwithstanding, the aforementioned architectures were trained and assessed 100 times on the same dataset to obtain the statistical results listed

in Table 2. Furthermore, for a clearer graphical representation of denoising performance, we provide the outcomes of these methods on five data samples, see Figure 11. When compared to the groundtruth the CBRDNet results are very close to the real ones, MAE improvements range from 2.5 times better when compared to CDnCNN_B and 1.2 times better when compared to CBDNet. Similar improvements are measured in terms of RMSE.

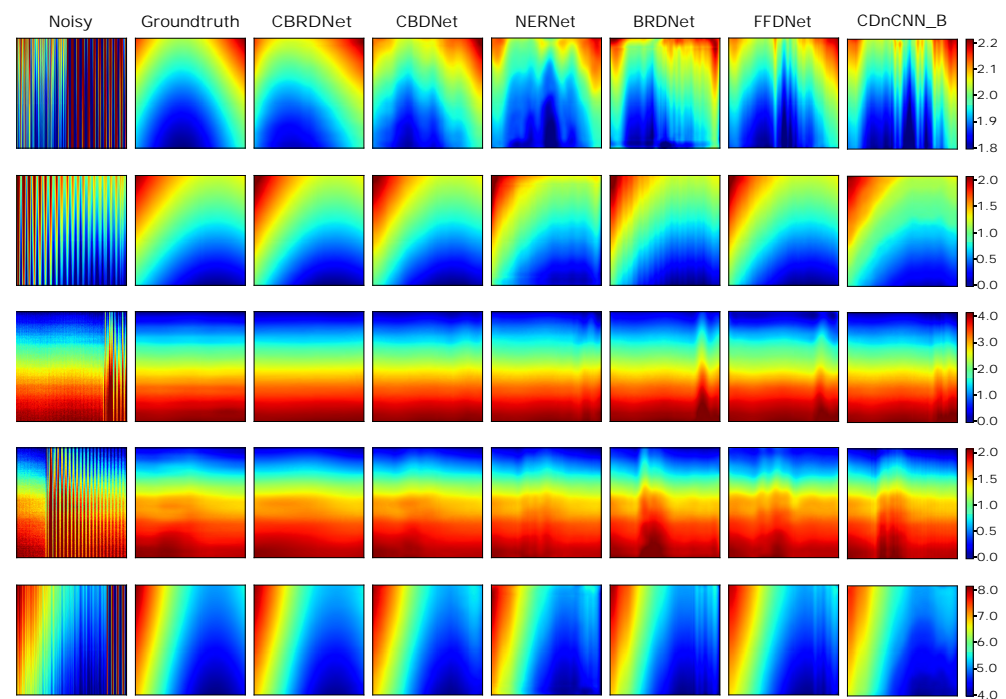


Figure 11. Comparison of our proposed CBRDNet with other methods on five different samples. Note that because of the low SNR, the geometrical surface of the samples is hidden by the induced perturbations. To facilitate the comparison with the denoised samples, the color scale of the images corresponding to the first column, i.e., noisy sample, is clipped. Color scale values are expressed in millimeters (mm). (Color online).

7.2. Real Data Results

Measuring results from a specimen tested out of the roll levelling system with a CMM cannot be fairly compared to those obtained by our method, as has been previously discussed in Section 6. Results obtained with the double laser line sensor and the Hermite filtering method proposed by Alonso et al. [10] have been used as groundtruth in order to evaluate the improvement of the proposed method in an industrial environment. Experimental results with real data are shown in Figures 12 and 13, where (a) is the denoised data using Hermite cubic interpolation, (b) is the raw data retrieved from the sensor and, finally, (c) is the denoised surface obtained using our method. The proposed CBRDNet architecture effectively recovers the smooth reconstructed surface after the noisy waves have been filtered, as seen in the figures.

The results shows graphically that the proposed method is capable of accurately reconstructing the surface of the metal sheet. When compared to state-of-the-art techniques, it achieves equivalent or better visually appealing results, as a real ground truth is always lacking in real experiments. Figure 14 depicts a longitudinal fibre, with unfiltered data collected directly from the sensor in blue, Hermite filtering in red, 2D Symlet wavelet-based filtering results in yellow, and the results from the CNN proposed in this work in green. It can be seen that the method is capable of reconstructing the sheet's surface preserving the sinusoidal characteristics of the metal sheet, specially in areas where the cutting effect occurs.

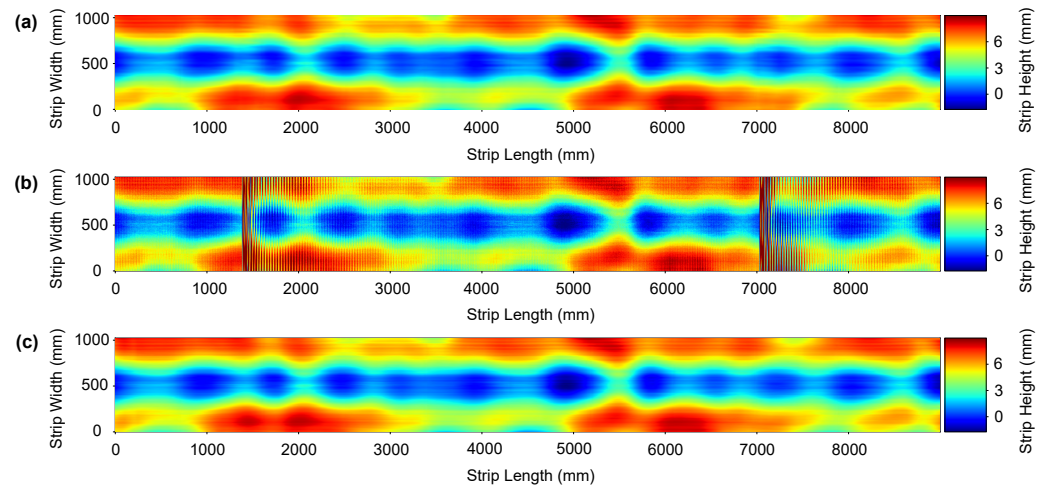


Figure 12. An instance of a real metal sheet surface denoising. Plate thickness: 3 mm; yield point Re: 215 MPa; Dimension of the mother plate—length: 9 m; width: 1050 mm. (a) Hermite filter denoised ground truth surface, (b) noise corrupted surface and (c) denoised reconstructed surface using the proposed network. (Color online).

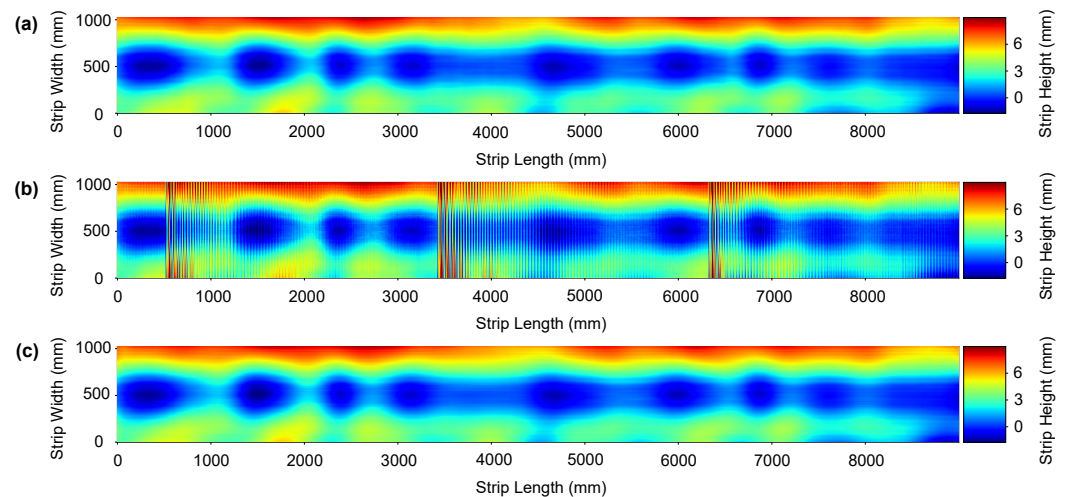


Figure 13. An instance of a real metal sheet surface denoising. Plate thickness: 6mm; yield point Re: 500 MPa; Dimension of the mother plate—length: 9 m; width: 1050 mm. (a) Hermite filter denoised ground truth surface, (b) noise corrupted surface and (c) denoised reconstructed surface using the proposed network. (Color online).

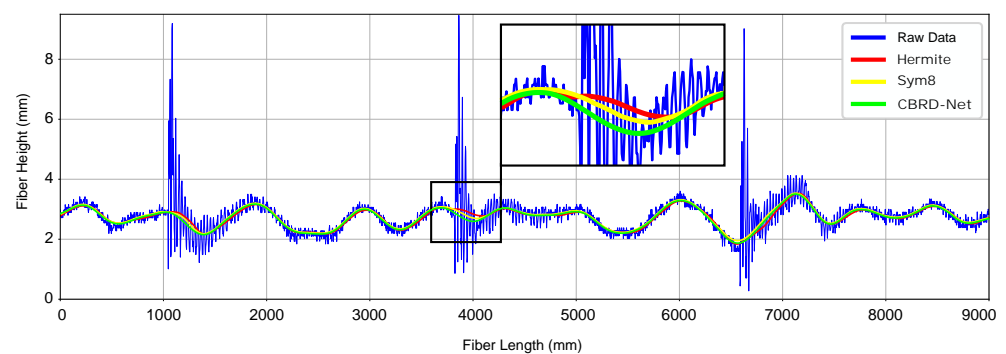


Figure 14. An instance of longitudinal fiber reconstruction, the blue line represents the raw 1D data from a fiber extracted from Figure 13, the red line shows the Hermite interpolation result, the yellow line shows Symlet results, and finally the green line depicts the CBRDNet denoised result. The inset provides a better detail of the results achieved by both Hermite and CBRDNet in the highlighted area.

7.3. Ablation Studies

Several ablation studies have been carried out in order to analyse the effects of both the noise estimation module (NE-SNet subnetwork) and training the network with synthetic, real, and mixed datasets.

7.3.1. Effect of the NE-SNet Subnetwork

An ablation study was conducted to better understand the contribution of the NE-SNet subnetwork component to the overall system. This research has revealed that the overall performance of the proposed system is highly dependant on the NE-SNet subnetwork, increasing the accuracy of the proposed network up to 10%. Quantitative results of this study are shown in Table 3. Besides that, noise prediction experiments reveal that the NE-SNet achieves an accuracy of nearly a 85% extracting the noise both in synthetic and real data. Figure 15 depicts some results obtain by the NE-SNet subnetwork over both synthetic and real metal strip patches. The mean absolute error (MAE), maximum absolute error (MaxAE), standard deviation of the absolute error (STD), and root mean squared error (RMSE) were evaluated over a 500 sample dataset, results are as follows, MAE = 0.420 mm, MaxAE = 1.105 mm, STD = 0.124, and RMSE = 0.480 mm.

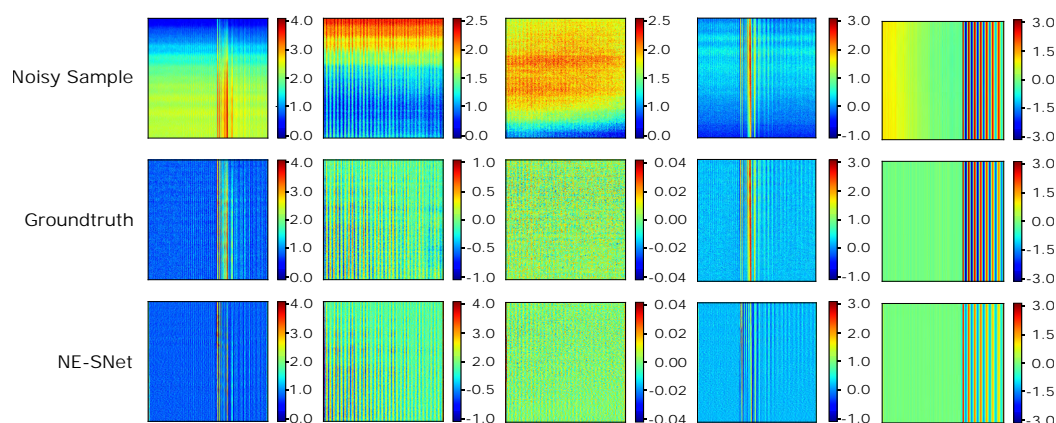


Figure 15. Results of the proposed NE-SNet subnetwork estimating the noise level map over a set of real and synthetic data samples. Noisy Sample stands for the corrupted noisy data, groundtruth is the known noise level map, finally NE-SNet is the estimated noise output. Color scale values are expressed in millimeters (mm). (Color online).

Table 3. Comparative results of our NE-SNet subnetwork ablation study with the full model and the best CNN and conventional denoising approaches. MAE = mean absolute error; MaxAE = maximum absolute error; STD = standard deviation of the absolute error; RMSE = root mean squared error. Best results presented in bold font.

Method	CNN-2D/1D/2D	MAE *	MaxAE *	STD *	RMSE *
CBRDNet (Full Model)	CNN-2D	0.140	0.376	0.136	0.147
CBRDNet (No NE-SNet)	CNN-2D	0.305	1.043	0.284	0.385
CBDNet	CNN-2D	0.172	0.520	0.162	0.185
Sym8	2D	0.176	0.543	0.170	0.188
Hermite	1D	0.413	1.150	0.380	0.459

* Measurements are expressed in millimeters (mm).

7.3.2. Effect of Synthetic and Real Data

We have developed the following approaches. First, we trained our proposed CBRDNet on synthetic data exclusively. Second we trained CBRDNet on real data only. On the one hand, the experiments carried out demonstrate that CBRDNet (Synth) achieve worse results than CBRDNet (Real) and CBRDNet removing the existing real noise. This fact occurs even when trained on large amount of synthetic data samples, mainly because real noise cannot be accurately described by the defined noise model at 3. On the other hand, CBRDNet (Real) produces not so accurate results in comparison to CBRDNet, as a result of the impact of insufficiently noise-free real data. At the same time, CBRDNet has proved to be more effective in dealing with real noise while maintaining an accurate surface information. Quantitative results of the three strategies are shown in Table 4 on 500 sample synthetic, real, and mixed datasets. CBRDNet obtains better results than CBRDNet(Synth) and CBRDNet(Real) except in the synthetic dataset, but we dismiss these results as they are not directly applicable to a real production environment where real noise is present.

Table 4. Comparative results of training data ablation studies. MAE = mean absolute error; MaxAE = maximum absolute error; STD = standard deviation of the absolute error; RMSE = root mean. (Synth) = trained on synthetic dataset; (Real) = trained on real dataset squared error. Best results presented in bold font.

Method	MAE *	MaxAE *	STD *	RMSE *
Mixed dataset results				
CBRDNet	0.140	0.376	0.136	0.147
CBRDNet (Synth)	0.260	0.496	0.248	0.265
CBRDNet (Real)	0.180	0.401	0.175	0.186
Synthetic dataset results				
CBRDNet	0.190	0.410	0.181	0.195
CBRDNet (Synth)	0.110	0.206	0.128	0.129
CBRDNet (Real)	0.280	0.526	0.254	0.292
Real dataset results				
CBRDNet	0.147	0.386	0.142	0.154
CBRDNet (Synth)	0.282	0.366	0.265	0.291
CBRDNet (Real)	0.159	0.396	0.155	0.161

* Measurements are expressed in millimeters (mm).

8. Conclusions and Future Work

In this paper, we present a novel denoising deep learning architecture for filtering range image sensor data that can be used for accurate flatness measurement in the context of metal sheet manufacturing, named CBRDNet.

This network is able to filter out the non-linear noise components in the range images that hinder accurate surface reconstruction and thus surface flatness measurements. It has been trained using both real and synthetic samples of steel coils from a roll leveling cut to length line. This combination improves the network's denoising capabilities. Furthermore, synthetic data not only provided a wide range of representative samples for training, but also a groundtruth for quantitative evaluation of the accuracy of the denoised flatness measurements. We carried out different experiments to validate the proposed filtering strategy.

In the first place, results obtained denoising synthetic data have proved that our method outperforms traditional 1D filtering techniques, namely Hermite, Savitzky-Golay, Chebyshev, and Butterworth filters. Compared to them, we achieved an improvement of up to 6 times in terms of accuracy, particularly in surface regions where high amplitude noises are induced by the mechanical processes carried out in the production line, e.g., cutting the metal strip to the desired length. In the second place, the proposed CBRDNet achieves slightly better results in comparison with 2D wavelet-based filtering techniques.

We achieved an error reduction up to 1.3 times when compared to the best performing wavelet in our study, i.e., Symlets (Sym8), although in some sample regions there was no clear improvement in terms of precision. Wavelet denoising results must be taken with a grain of salt, because an optimal wavelet class and order selection might improve them, while we report results of a necessarily limited empirical exploration. To this date we do not know of such a data driven optimal wavelet design process. In the third place, experiments with synthetic data show that the CBRDNet architecture is able to obtain better results than state-of-the-art deep learning denoising architectures for the specific kind of noise that we are dealing with. Compared to these methods we obtain improvements ranging from 1.2 up to 2.5 times in terms of surface reconstruction accuracy. This improvement is clearly visible in the areas of the metal sheet where the noise due to metal strip cutting occurs.

Finally, results with real data obtained from an industrial leveling cut to length line have shown that the proposed method is capable of accurately reconstructing metal sheet surfaces. The conducted experiments have shown a surface reconstruction error reduction than can be down to 15% relative to solutions based on conventional interpolation methods. Numerical results have shown that the proposed CBRDNet achieves a mean absolute error (MAE) of 0.140mm a maximum absolute error (MaxAE) of 0.376 mm, a standard deviation of the absolute error (STD) of 0.136 mm, and a root mean squared error (RMSE) of 0.147 mm.

Future research will explore deep denoising architectures in the frequency domain. Although in some cases it is difficult to differentiate a signal from noise in the spatial domain, this task might be easier in the frequency domain because noisy signals can be comprised of a set of sine wave signals represented in the frequency domain with different frequencies, phases, and amplitudes. We intend to implement and compare these possible enhancements to the network outlined in this paper in future works. Moreover, when larger data sets are needed but the access to real data is restricted in some way, for example, when data becomes sensitive to its distribution, or simply when access to real data is challenging, the development of tools capable of generating synthetic data would provide a solution to this data shortage. GANs are computational structures that employ two neural networks, competing with each other, to create new synthetic data samples that may be used as surrogates for real data. To further our research we plan to explore the potential of using GANs architectures instead of the current noise model to generate larger dataset with more likelihood to real data.

Author Contributions: Conceptualization, M.A., A.I., D.M., I.A. and M.G.; methodology, M.A., A.I., D.M., I.A. and M.G.; software, M.A., I.A. and D.M.; validation, M.A.; formal analysis, M.A., A.I., I.A. and M.G.; writing, original draft preparation, M.A., A.I., D.M. and M.G.; writing, review and editing, M.A., A.I., D.M., I.A. and M.G.; visualisation, M.A. and M.G.; project administration, M.A. and M.G.; funding acquisition, M.A. and M.G. All authors read and agreed to the published version of the manuscript.

Funding: This work was partially supported by by FEDER funds through MINECO project TIN2017-85827-P, and ELKARTEK funded projects ENSOL2 and CODISAVA2 (KK-202000077 and KK-202000044) supported by the Basque Government.

Institutional Review Board Statement: Not applicable.

Informed Consent Statement: Not applicable.

Conflicts of Interest: The authors declare no conflict of interest.

Abbreviations

The following abbreviations are used in this manuscript:

CNN	Convolutional Neural Network
DAE	Denoising Autoencoders
CDAE	Convolutional Denoising Autoencoders
GAN	Generative Adversarial Network
SGD	Stochastic Gradient Descent
CBRDNet	Convolutional Blind Residual Denoising Network
NE-SNet	Noise Estimation Subnetwork
NR-SNet	Noise Removal Subnetwork
ADAM	Adaptive Moment Estimation
ReLU	Rectified Linear Unit
BN	Batch Normalization
Conv2D	2D Convolution Layer
HSLA	High-Strength Low-Alloy
MSE	Mean Squared Error
MAE	Mean Absolute Error
MaxAE	Maximum Absolute Error
STD	Standard Deviation
RMSE	Root Mean Squared Error
CMM	Coordinate Measuring Machine
Db	Daubechies
Coif	Coiflets
Sym	Symlets
Fk	Fejer-Korovkin
Dmey	Meyer

References

- Jouet, J.; Francois, G.; Tourscher, G.; de Lamberterie, B. Automatic flatness control at Solmer hot strip mill using the Lasershape sensor. *Iron Steel Eng.* **1988**, *65*, 50–56.
- Chiarella, M.; Pietrzak, K.A. An Accurate Calibration Technique for 3D Laser Stripe Sensors. In *Optics, Illumination, and Image Sensing for Machine Vision IV*; Svetkoff, D.J., Ed.; International Society for Optics and Photonics, SPIE, Bellingham: Washington, CA, USA, 1990; Volume 1194, pp. 176–185. [\[CrossRef\]](#)
- Álvarez, H.; Alonso, M.; Sánchez, J.R.; Izaguirre, A. A Multi Camera and Multi Laser Calibration Method for 3D Reconstruction of Revolution Parts. *Sensors* **2021**, *21*, 765. [\[CrossRef\]](#)
- Siekański, P.; Magda, K.; Malowany, K.; Rutkiewicz, J.; Styk, A.; Krzesłowski, J.; Kowaluk, T.; Zagórski, A. On-line laser triangulation scanner for wood logs surface geometry measurement. *Sensors* **2019**, *19*, 1074. [\[CrossRef\]](#) [\[PubMed\]](#)
- Kierkegaard, P.; Classon, L.A. A new-generation optical flatness measurement system. *Iron Steel Technol.* **2015**, *12*, 76–81.
- Kierkegaard, P. Developments and Benefits from Optical Flatness Measurement in Strip Processing Lines. In Proceedings of the Congreso y Exposición Nacional de la Industria del Acero, CONAC, Monterrey, Mexico, 8–20 November 2016; pp. 1–15.
- Pernkopf, F. 3D surface acquisition and reconstruction for inspection of raw steel products. *Comput. Ind.* **2005**, *56*, 876–885. [\[CrossRef\]](#)
- Usamentiaga, R.; Molleda, J.; Garcia, D.F.; Bulnes, F.G. Removing vibrations in 3D reconstruction using multiple laser stripes. *Opt. Lasers Eng.* **2014**, *53*, 51–59. [\[CrossRef\]](#)
- Usamentiaga, R.; Garcia, D.F. Robust registration for removing vibrations in 3D reconstruction of web material. *Opt. Lasers Eng.* **2015**, *68*, 135–148. [\[CrossRef\]](#)
- Alonso, M.; Izaguirre, A.; Andonegui, I.; Graña, M. Optical Dual Laser Based Sensor Denoising for Online Metal Sheet Flatness Measurement Using Hermite Interpolation. *Sensors* **2020**, *20*, 5441. [\[CrossRef\]](#)
- Alonso, M.; Izaguirre, A.; Andonegui, I.; Graña, M. An Application of Laser Measurement to On-Line Metal Strip Flatness Measurement. In Proceedings of the 15th International Conference on Soft Computing Models in Industrial and Environmental Applications (SOCO 2020), Burgos, Spain, 16–18 September 2020; Springer International Publishing: Cham, Switzerland, 2021; pp. 835–842.
- Ronneberger, O.; Fischer, P.; Brox, T. U-Net: Convolutional Networks for Biomedical Image Segmentation. In Proceedings of the Medical Image Computing and Computer-Assisted Intervention—MICCAI 2015, Munich, Germany, 5–9 October 2015; Navab, N., Hornegger, J., Wells, W.M., Frangi, A.F., Eds.; Springer International Publishing: Cham, Switzerland, 2015; pp. 234–241.
- Borselli, A.; Colla, V.; Vannucci, M.; Veroli, M. A fuzzy inference system applied to defect detection in flat steel production. In Proceedings of the International Conference on Fuzzy Systems, Barcelona, Spain, 18–23 July 2010; pp. 1–6. [\[CrossRef\]](#)

14. Borselli, A.; Colla, V.; Vannucci, M. Surface Defects Classification in Steel Products: A Comparison between Different Artificial Intelligence-based Approaches. In Proceedings of the 11th IASTED International Conference on Artificial Intelligence and Applications, AIA 2011, Innsbruck, Austria, 14–16 February 2011. [\[CrossRef\]](#)
15. Xu, K.; Xu, Y.; Zhou, P.; Wang, L. Application of RNAMlet to surface defect identification of steels. *Opt. Lasers Eng.* **2018**, *105*, 110–117. [\[CrossRef\]](#)
16. Brandenburger, J.; Colla, V.; Nastasi, G.; Ferro, F.; Schirm, C.; Melcher, J. Big Data Solution for Quality Monitoring and Improvement on Flat Steel Production. *IFAC-PapersOnLine* **2016**, *49*, 55–60. [\[CrossRef\]](#)
17. Appio, M.; Ardesi, A.; Lugnan, A. Automatic Surface Inspection in Steel Products ensures Safe, Cost-Efficient and Timely Defect Detection in Production. In Proceedings of the AISTech-Iron and Steel Technology Conference, São Paulo, Brazil, 2–4 October 2018; pp. 89–101.
18. Graña, M.; Alonso, M.; Izaguirre, A. A Panoramic Survey on Grasping Research Trends and Topics. *Cybern. Syst.* **2019**, *50*, 40–57. [\[CrossRef\]](#)
19. Chong, E.; Han, C.; Park, F. Deep Learning Networks for Stock Market Analysis and Prediction: Methodology, Data Representations, and Case Studies. *Expert Syst. Appl.* **2017**, *83*, 187–205. [\[CrossRef\]](#)
20. Chen, X.W.; Lin, X. Big Data Deep Learning: Challenges and Perspectives. *IEEE Access* **2014**, *2*, 514–525. [\[CrossRef\]](#)
21. Najafabadi, M.M.; Villanustre, F.; Khoshgoftaar, T.M.; Seliya, N.; Wald, R.; Muharemagic, E. Deep learning applications and challenges in big data analytics. *J. Big Data* **2015**, *2*, 1. [\[CrossRef\]](#)
22. Affonso, C.; Rossi, A.L.D.; Vieira, F.H.A.; de Leon Ferreira de Carvalho, A.C.P. Deep learning for biological image classification. *Expert Syst. Appl.* **2017**, *85*, 114–122. [\[CrossRef\]](#)
23. Liu, Y.; Geng, J.; Su, Z.; Zhang, W.; Li, J. Real-Time Classification of Steel Strip Surface Defects Based on Deep CNNs. In *Proceedings of 2018 Chinese Intelligent Systems Conference, Vol II*; Springer: Singapore, 2019; pp. 257–266. [\[CrossRef\]](#)
24. Wang, Y.; Li, C.; Peng, L.; An, R.; Jin, X. Application of convolutional neural networks for prediction of strip flatness in tandem cold rolling process. *J. Manuf. Process.* **2021**, *68*, 512–522. [\[CrossRef\]](#)
25. Hinton, G.E.; Zemel, R.S. Autoencoders, minimum description length, and Helmholtz free energy. *Adv. Neural Inf. Process. Syst.* **1994**, *6*, 3–10.
26. Goodfellow, I.; Bengio, Y.; Courville, A. *Deep Learning*; MIT Press: Cambridge, MA, USA, 2016.
27. Schmidhuber, J. Deep learning in neural networks: An overview. *Neural Netw.* **2015**, *61*, 85–117. [\[CrossRef\]](#)
28. Bank, D.; Koenigstein, N.; Giryas, R. Autoencoders. *arXiv* **2021**, arXiv:2003.05991.
29. Vincent, P.; Larochelle, H.; Bengio, Y.; Manzagol, P.A. Extracting and Composing Robust Features with Denoising Autoencoders. In Proceedings of the 25th International Conference on Machine Learning, ICML'08, Helsinki, Finland, 5–9 July 2008; Association for Computing Machinery: New York, NY, USA, 2008; pp. 1096–1103. [\[CrossRef\]](#)
30. Ruder, S. An overview of gradient descent optimization algorithms. *arXiv* **2017**, arXiv:1609.04747.
31. Gondara, L. Medical Image Denoising Using Convolutional Denoising Autoencoders. In Proceedings of the 2016 IEEE 16th International Conference on Data Mining Workshops (ICDMW), Barcelona, Spain, 12–15 December 2016; IEEE Computer Society: Los Alamitos, CA, USA, 2016; pp. 241–246. [\[CrossRef\]](#)
32. Masci, J.; Meier, U.; Cireşan, D.; Schmidhuber, J. Stacked Convolutional Auto-Encoders for Hierarchical Feature Extraction. In Proceedings of the Artificial Neural Networks and Machine Learning—ICANN 2011, Espoo, Finland, 14–17 June 2011; Honkela, T., Duch, W., Girolami, M., Kaski, S., Eds.; Springer: Berlin/Heidelberg, Germany, 2011; pp. 52–59.
33. Li, H.; Xu, Z.; Taylor, G.; Goldstein, T. Visualizing the Loss Landscape of Neural Nets. *arXiv* **2017**, arXiv:1712.09913.
34. Roy, H.; Chaudhury, S.; Yamasaki, T.; DeLatte, D.; Ohtake, M.; Hashimoto, T. Lunar surface image restoration using U-net based deep neural networks. *arXiv* **2019**, arXiv:1904.06683.
35. Lee, S.; Negishi, M.; Urakubo, H.; Kasai, H.; Ishii, S. Mu-net: Multi-scale U-net for two-photon microscopy image denoising and restoration. *Neural Netw.* **2020**, *125*, 92–103. [\[CrossRef\]](#) [\[PubMed\]](#)
36. Komatsu, R.; Gonsalves, T. Comparing U-Net Based Models for Denoising Color Images. *AI* **2020**, *1*, 465–486. [\[CrossRef\]](#)
37. Isola, P.; Zhu, J.Y.; Zhou, T.; Efros, A. Image-to-Image Translation with Conditional Adversarial Networks. In Proceedings of the IEEE Conference on Computer Vision and Pattern Recognition, Honolulu, HI, USA, 21–26 July 2017; pp. 5967–5976. [\[CrossRef\]](#)
38. Jansson, A.; Humphrey, E.; Montecchio, N.; Bittner, R.; Kumar, A.; Weyde, T. Singing voice separation with deep U-Net convolutional networks. In Proceedings of the 18th International Society for Music Information Retrieval Conference, Suzhou, China, 23–27 October 2017.
39. Zhang, Z.; Liu, Q.; Wang, Y. Road Extraction by Deep Residual U-Net. *IEEE Geosci. Remote Sens. Lett.* **2018**, *15*, 749–753. [\[CrossRef\]](#)
40. Guo, S.; Yan, Z.; Zhang, K.; Zuo, W.; Zhang, L. Toward Convolutional Blind Denoising of Real Photographs. In Proceedings of the 2019 IEEE/CVF Conference on Computer Vision and Pattern Recognition (CVPR), Long Beach, CA, USA, 16–20 June 2019; pp. 1712–1722.
41. Guo, B.; Song, K.; Dong, H.; Yan, Y.; Tu, Z.; Zhu, L. NERNet: Noise estimation and removal network for image denoising. *J. Vis. Commun. Image Represent.* **2020**, *71*, 102851. [\[CrossRef\]](#)
42. Tian, C.; Xu, Y.; Zuo, W. Image denoising using deep CNN with batch renormalization. *Neural Netw.* **2020**, *121*, 461–473. [\[CrossRef\]](#)

43. Zhang, K.; Zuo, W.; Zhang, L. FFDNet: Toward a Fast and Flexible Solution for CNN-Based Image Denoising. *IEEE Trans. Image Process.* **2018**, *27*, 4608–4622. [[CrossRef](#)]
44. Zhang, K.; Zuo, W.; Chen, Y.; Meng, D.; Zhang, L. Beyond a Gaussian Denoiser: Residual Learning of Deep CNN for Image Denoising. *IEEE Trans. Image Process.* **2017**, *26*, 3142–3155. [[CrossRef](#)]
45. Buades, A.; Coll, B.; Morel, J.M. A Review of Image Denoising Algorithms, with a New One. *Multiscale Model. Simul.* **2005**, *4*, 490–530. [[CrossRef](#)]
46. Limshuebchuey, A.; Duangsoithong, R.; Saejia, M. Comparison of Image Denoising using Traditional Filter and Deep Learning Methods. In Proceedings of the 2020 17th International Conference on Electrical Engineering/Electronics, Computer, Telecommunications and Information Technology (ECTI-CON), Phuket, Thailand, 24–27 June 2020; pp. 193–196. [[CrossRef](#)]
47. Fan, L.; Zhang, F.; Fan, H.; Zhang, C. Brief review of image denoising techniques. *Vis. Comput. Ind. Biomed. Art* **2019**, *2*, 7. [[CrossRef](#)]
48. Testolin, A.; Stoianov, I.; De Filippo De Grazia, M.; Zorzi, M. Deep Unsupervised Learning on a Desktop PC: A Primer for Cognitive Scientists. *Front. Psychol.* **2013**, *4*, 251. [[CrossRef](#)] [[PubMed](#)]
49. Lee, H.; Grosse, R.; Ranganath, R.; Ng, A. Convolutional deep belief networks for scalable unsupervised learning of hierarchical representations. In Proceedings of the 26th Annual International Conference on Machine Learning, Montreal, QC, Canada, 14–18 June 2009; p. 77. [[CrossRef](#)]
50. Lan, R.; Zou, H.; Pang, C.; Zhong, Y.; Liu, Z.; Luo, X. Image denoising via deep residual convolutional neural networks. *Signal Image Video Process.* **2021**, *15*, 1–8. [[CrossRef](#)]
51. Seib, V.; Lange, B.; Wirtz, S. Mixing Real and Synthetic Data to Enhance Neural Network Training—A Review of Current Approaches. *arXiv* **2020**, arXiv:2007.08781.
52. He, K.; Zhang, X.; Ren, S.; Sun, J. Deep Residual Learning for Image Recognition. In Proceedings of the IEEE Conference on Computer Vision and Pattern Recognition, Las Vegas, NV, USA, 27–30 June 2016; pp. 770–778. [[CrossRef](#)]
53. Kingma, D.P.; Ba, J. Adam: A Method for Stochastic Optimization. *arXiv* **2017**, arXiv:1412.6980.
54. He, K.; Zhang, X.; Ren, S.; Sun, J. Delving Deep into Rectifiers: Surpassing Human-Level Performance on ImageNet Classification. In Proceedings of the IEEE International Conference on Computer Vision (ICCV 2015), Santiago, Chile, 7–13 December 2015; Volume 1502. [[CrossRef](#)]
55. Masters, D.; Luschi, C. Revisiting Small Batch Training for Deep Neural Networks. *arXiv* **2018**, arXiv:1804.07612.
56. Kandel, I.; Castelli, M. The effect of batch size on the generalizability of the convolutional neural networks on a histopathology dataset. *ICT Express* **2020**, *6*, 312–315. [[CrossRef](#)]
57. Maas, A.L.; Hannun, A.Y.; Ng, A.Y. Rectifier nonlinearities improve neural network acoustic models. In Proceedings of the 30th International Conference on Machine Learning, Atlanta, GA, USA, 16–21 June 2013.
58. ASTM A1030/A1030M-11, *Measuring Flatness Characteristics of Steel Sheet Products, Standard Practice for*; ASTM International: West Conshohocken, PA, USA, 2011.
59. Butterworth, S. On the theory of filter amplifiers. *Wirel. Eng.* **1930**, *7*, 536–541.
60. Oppenheim, A.; Schaffer, R.; Buck, J.; Lee, L. *Discrete-Time Signal Processing*; Prentice Hall international editions; Prentice Hall: Hoboken, NJ, USA, 1999.
61. Savitzky, A.; Golay, M.J.E. Smoothing and Differentiation of Data by Simplified Least Squares Procedures. *Anal. Chem.* **1964**, *36*, 1627–1639. [[CrossRef](#)]
62. Schaffer, R.W. What Is a Savitzky-Golay Filter? [Lecture Notes]. *IEEE Signal Process. Mag.* **2011**, *28*, 111–117. [[CrossRef](#)]
63. Weinberg, L.; Slepian, P. Takahasi's Results on Tchebycheff and Butterworth Ladder Networks. *IRE Trans. Circuit Theory* **1960**, *7*, 88–101. [[CrossRef](#)]
64. Daubechies, I. *Ten Lectures on Wavelets*; Society for Industrial and Applied Mathematics, 3600 University City Science Center: Philadelphia, PA, USA, 1992.
65. Meyer, Y. *Ondelettes et Opérateurs*; Number v. 1 in Actualités Mathématiques; Hermann, MS, USA, 1990.
66. Nielsen, M. On the Construction and Frequency Localization of Finite Orthogonal Quadrature Filters. *J. Approx. Theory* **2001**, *108*, 36–52. [[CrossRef](#)]
67. ASTM A568/A568M-17a, *Standard Specification for Steel, Sheet, Carbon, Structural, and High-Strength, Low-Alloy, Hot-Rolled and Cold-Rolled, General Requirements for*; ASTM International: West Conshohocken, PA, USA, 2017.
68. Peng, Z.; Wang, G. Study on Optimal Selection of Wavelet Vanishing Moments for ECG Denoising. *Sci. Rep.* **2017**, *7*, 4564. [[CrossRef](#)] [[PubMed](#)]
69. Galiano, G.; Velasco, J. On a nonlocal spectrogram for denoising one-dimensional signals. *Appl. Math. Comput.* **2014**, *244*, 859–869. [[CrossRef](#)]

